

Todo list

Get a picture of EGRET to include	10
Short description of the history of TeV astronomy	12
What is the LAT effective area?	12
Make note of “Air force had early warning of pulsars” paper	13
First gamma-ray detection	13
When was the PSR, PWN connection made	14
XX	
Get image of Synchrotron radiation (from R&L to include in discussion. . . .	18
Why no Bremsstrahlung radiation from PWN. Maybe a back-of-the-envelope estimate	21
Describe the characteristic π^0 cutoff energy	21
Include discussion of modeling, if time permitting	21
Describe Catalog	22
Dig up HESS reference of HESS J1514-59.	23
Where are sites of acceleratoin	30
Discuss pulsar evolution “The Evolution and Structure of Pulsar Wind Nebulae” – Bryan M. Gaensler and Patrick O. Slane	32
Describe Mattana’s work on pulsar wind nebulae (PWNe): “On the evolution of the Gamma- and X-ray luminosities of Pulsar Wind Nebulae”	32
Describe SNR Reverse Shock	34
Include discussion of cooling in Matanna et al 2009 (equation 12	35
Look up scaling relationships for IC and Sync radiation from Adam Van Etten’s thesis	35

what section discusses energy dependent psf?	37
What are the benefits of maximum likelihood	38
Describe Wilk's Therorem and it's application to parameter error estimation .	38
WHAT SECTION DESCRIBES EXTENDED SOURCE PDFs	40
FINISH DISCUSSION	40
Discuss how diffuse background is more complciated and requires a mapcube.	40
LINK TO arXiv:1206.1896 for MORE THOUROUGH DISCUSSION OF EF- FECTIVE AREA	41
DISCUSS HOW EFFECTIVE AREA IS A FUNCTION OF DIFFERENT THINGS	41
What is the range of the integrals	41
BETTER DISCUSSION OF PSF OF THE LAT, WHAT ITS SCALE IS... .	42
Why discard time dispersion	42
WRITE ENERGY DISPERSION AS A DELTA FUNCTION	42
FINISH	43
Figure out how the θ depedence of the IRFs factors into this calcualtion . . .	43
Write Section or Perform simple MC Simulation to demonstrate significance of detection	44
What would make good future work. Something about CTA population study, something about improved modeling liek HESS J1825, something about better PSF	107

OBSERVATIONS OF PWNE WITH THE FERMI GAMMA-RAY
SPACE TELESCOPE

A DISSERTATION
SUBMITTED TO THE DEPARTMENT OF PHYSICS
AND THE COMMITTEE ON GRADUATE STUDIES
OF STANFORD UNIVERSITY
IN PARTIAL FULFILLMENT OF THE REQUIREMENTS
FOR THE DEGREE OF
DOCTOR OF PHILOSOPHY

Joshua Jeremy Lande

March 2013

© Copyright by Joshua Jeremy Lande 2013
All Rights Reserved

I certify that I have read this dissertation and that, in my opinion, it is fully adequate in scope and quality as a dissertation for the degree of Doctor of Philosophy.

(Stefan Funk) Principal Adviser

I certify that I have read this dissertation and that, in my opinion, it is fully adequate in scope and quality as a dissertation for the degree of Doctor of Philosophy.

(Elliott Bloom)

I certify that I have read this dissertation and that, in my opinion, it is fully adequate in scope and quality as a dissertation for the degree of Doctor of Philosophy.

(Roger Romani)

Approved for the University Committee on Graduate Studies

Abstract

Two things fill the mind with ever-increasing wonder and awe, the more often and the more intensely the mind of thought is drawn to them: the starry heavens above me and the moral law within me.” – Immanuel Kant

The launch of the *Fermi* Gamma-ray space telescope in 2008 offered an unprecedented view into the γ -ray sky.

All the things we can learn with the the Large Area Telescope (LAT)

Development of a new analysis method for studying spatially-extended PWNs using `pointlike`.

A monte-carlo validation of the analysis method.

Search for new spatially-extended sources with the LAT.

Observations of PWNs in the off-peak region of LAT detected pulsars.

Search for PWNs counterparts to TeV sources.

Using the population of PWNs to understand the radiation mechanism of PWNs.

Acknowledgement

Acknowledge the educational institutes which taught me physics: My high school HB Woodlawn, my undergraduate institution Marlboro College, and my Stanford University.

First, I would like to acknowledge those mentors who inspired me to get a PhD.

- Mark Dodge, my high school physics teacher.
- Ron Turner, my internship adviser at Analytic Services (ANSER) during the GWU Science and Engineering Apprentice Program (SEAP)
- Anthony Tyson at UC Davis for my SULI Internship
- Apurva Mehta and Sam Webb sam Web at SLAC SULI Internship.

During my PhD I was helped by an almost overwhelminlgy large number of people in the LAT collaboration.

People at Stanford/SLAC: Stefan Funk, Elliott Bloom, Markus Ackermann, Tobias Jogler, Junichiro Katsuta, Yasunobu Uchiyama, Seth Digel, James Chiang

`pointlike` collaborators: Matthew Kerr, Toby Burnett, Eric Wallace, Marshall Roth

Pulsar Collaborators: David Smith, Matthew Kerr, Peter den Hartog, Tyrel Johnson, Damien Parent, Ozlem Celik

Careful review of text: Jean Ballet, Johann Cohen-Tanugi

I would like to thank the PWNs people Thank the people in Bordeaux: Marianne Lemoine-Goumard, Romain Rousseau, and Marie-Hélène Grondin

Fermi SLAC Grad Students: Keith Bechtol, Alex Drlica-Wagner, Alice Allafort, Herman Lee Yvonne Edmonds, Bijan Berenji, Ping Wang, Warit Mitthumsiri

Joanne Bogart, Heather Kelly, Richard Dubois, Renata Dart, Stuart Marshall, and Glenn Morris for putting up with my computer problems.

Martha Siegel, Chris Hall, Ziba Mahdavi, awesome SLAC administrators. Maria Frank, Elva Carbajal, and Violet Catindig , awesome Stanford administrators.

Additional Astro Stanford Graduate Students: Helen Craig, Michael Shaw, Adam Van Etten, Kyle Watters

Additonal Graduate Students at Stanford: Dan Riley, Joel Frederico, Ahmed Ismail, Joshua Cogan, Kunal Sahasrabuddhe,

Contents

Abstract	iv
Acknowledgement	v
1 Overview	3
2 Gamma-ray Astrophysics	4
2.1 Astronomy and the Atmosphere	4
2.2 The History of Gamma-ray Astrophysics	5
2.3 The <i>Fermi</i> Gamma-ray Space Telescope	12
2.3.1 The Tracker	12
2.3.2 The Calorimeter	12
2.3.3 Anti-Coincidence Detector	12
2.3.4 Gamma-ray Burst Monitor	12
2.4 Astrophysical Sources of Gamma-rays	12
2.4.1 Pulsars	12
2.4.2 Pulsar Wind Nebulae	14
2.5 Radiation Processes in Gamma-ray Astrophysics	17
2.5.1 Synchrotron	18
2.5.2 Inverse Compton	19
2.5.3 Bremsstrahlung	20
2.5.4 Pion Decay	21
2.6 The Galactic Diffuse and Isotropic Gamma-ray Background	21
2.7 Sources Detected by the Fermi the Large Area Telescope	22

2.7.1	The Second Fermi Catalog	22
2.7.2	The Second Fermi Pulsar Catalog	23
2.7.3	Pulsar Wind Nebulae Detected by The Large Area Telescope .	23
3	The Pulsar/Pulsar Wind Nebula System	25
3.1	Neutron Star Formation	25
3.2	Pulsar Evolution	26
3.3	Pulsar Magnetosphere	29
3.4	Pulsar Wind Nebulae Structure	31
3.5	Pulsar Wind Nebula Emission	35
4	Maximum-likelihood analysis of LAT data	36
4.1	Motivations for Maximum-Likelihood Analysis of Gamma-ray Data .	37
4.2	Description of Maximum-Likelihood Analysis	38
4.3	Defining a Model of the Sources in the Sky	38
4.4	The LAT Instrument Response Functions	41
4.5	Binned Maximum-Likelihood of LAT Data with the Science Tools . .	43
4.6	The Alternate Maximum-Likelihood Package <code>pointlike</code>	45
5	Analysis of Spatially Extended LAT Sources	46
5.1	Introduction	46
5.2	Analysis Method	49
5.2.1	Modeling Extended Sources in the <code>pointlike</code> Package	49
5.2.2	Extension Fitting	51
5.2.3	<code>gtlike</code> Analysis Validation	53
5.2.4	Comparing Source Sizes	53
5.3	Validation of the TS Distribution	54
5.3.1	Point-like Source Simulations Over a Uniform Background . .	54
5.3.2	Point-like Source Simulations Over a Structured Background .	56
5.3.3	Extended Source Simulations Over a Structured Background .	57
5.4	Extended Source Detection Threshold	59
5.5	Testing Against Source Confusion	60

5.6	Test of 2LAC Sources	64
6	Search for Pulsar Wind Nebulae associated with Gamma-loud Pulsars	103
6.1	Off-peak Phase Selection	103
6.2	Off-peak Analysis Method	103
6.3	Off-peak Results	103
6.4	Off-Peak Individual Source Discussion	103
7	Search for Pulsar Wind Nebulae associated with TeV Pulsars	104
7.1	List of Candidates	104
7.2	Analysis Method	104
7.3	Sources Detected	104
8	Search for Pulsar Wind Nebulae associated with High \dot{E} Pulsars	105
9	Population Study of The Large Area Telescope (LAT)-detected Pulsar wind nebula (PWN)	106
10	Future Work (or Outlook)??	107

List of Tables

5.1	Monte Carlo Spectral Parameters	69
5.2	Extension Detection Threshold	77
5.2	Extension Detection Threshold	78
5.3	Analysis of the twelve extended sources included in the 2FGL catalog	83
5.4	Extension fit for the nine additional extended sources	86
5.5	Dual localization, alternative PSF, and alternative approach to modeling the diffuse emission	87
5.6	Nearby Residual-induced Sources	88

List of Figures

2.1	Transparency of the atmosphere of the earth to photons of varying wavelenthts. This figure is from Carroll & Ostlie (2006)	4
2.2	The experimental design of Explorer XI. This figure is from Kraushaar et al. (1965).	6
2.3	The position of all 621 cosmic γ -rays detected by the Third Orbiting Solar Observatory (OSO-3). This figure is from Kraushaar et al. (1972).	8
2.4	A map of the sources observed by COS-B. The filled circles represent brighter sources. The unshaded region corresponds to the parts of the sky observed by COS-B. This figure is from Swanenburg et al. (1981).	10
2.5	The position of the Energetic Gamma Ray Experiment Telescope (EGRET) sources in the sky in galactic coordinates. The size of the source markers corresponds to the overall source intensity. This figure is from (Hartman et al. 1999).	11
2.6	The Orion plate from Bevis' book <i>Uranographia Britannica</i> . The Crab nebula can be found on the horn of Taurus the Bull on the top of the figure and the source is marked by a cloudy symbol. This figure was reproduced from Ashworth (1981).	15
3.1	The rotating dipole model of a puslar. This figure is taken from (Carroll & Ostlie 2006).	27
3.2	The magnetosphere for a rotating pulsar. The pulsar is on the bottom left of the plot. This figure is from Goldreich & Julian (1969).	30

3.3	The regions of emission in a pulsar/PWN system. This figure shows (top) the pulsar's magnetosphere, (middle), the unshocked pulsar wind and (bottom) the shocked pulsar wind which can be observed as the PWN. "R", "O", "X", and " γ " describe sites of radio, optical, X-ray, and γ -ray emission respectively. "CR", "Sy", and "IC" refer to regions of curvature, inverse Compton, and synchrotron emission. Figure is taken from Aharonian & Bogovalov (2003).	33
5.1	Counts maps and TS profiles for the SNR IC 443. (a) TS vs. extension of the source. (b) TS_{ext} for individual energy bands. (c) observed radial profile of counts in comparison to the expected profiles for a spatially extended source (solid and colored red in the online version) and for a point-like source (dashed and colored blue in the online version). (d) smoothed counts map after subtraction of the diffuse emission compared to the smoothed LAT PSF (inset). Both were smoothed by a 0.1° 2D Gaussian kernel. Plots (a), (c), and (d) use only photons with energies between 1 GeV and 100 GeV. Plots (c) and (d) include only photons which converted in the front part of the tracker and have an improved angular resolution (Atwood et al. 2009).	67
5.2	A comparison of a 2D Gaussian and uniform disk spatial model of extended sources before and after convolving with the PSF for two energy ranges. The solid black line is the PSF that would be observed for a power-law source of spectral index 2. The dashed line and the dash-dotted lines are the brightness profile of a Gaussian with $r_{68} = 0.5$ and the convolution of this profile with the LAT PSF respectively (colored red in the online version). The dash-dot-dotted and the dot-dotted lines are the brightness profile of a uniform disk with $r_{68} = 0.5$ and the convolution of this profile with the LAT PSF respectively (colored blue in the online version).	68

5.3	Cumulative distribution of the TS for the extension test when fitting simulated point-like sources in the 1 GeV to 100 GeV energy range. The four plots represent simulated sources of different spectral indices and the different lines (colored in the online version) represent point-like sources with different 100 MeV to 100 GeV integral fluxes. The dashed line (colored red) is the cumulative density function of Equation 5.11.	70
5.4	The same plot as Figure ?? but fitting in the 10 GeV to 100 GeV energy range.	71
5.5	Cumulative distribution of TS_{ext} for sources simulated on top of the Galactic diffuse and isotropic background.	72
5.6	The distribution of TS values when fitting 985 statistically independent simulations of W44. (a) is the distribution of TS values when fitting W44 as a point-like source and (b) is the distribution of TS_{ext} when fitting the source with a uniform disk or a radially-symmetric Gaussian spatial model. (c) is the distribution of the change in TS when fitting the source with an elliptical disk spatial model compared to fitting it with a radially-symmetric disk spatial model and (d) when fitting the source with an elliptical ring spatial model compared to an elliptical disk spatial model.	73
5.7	The distribution of fit parameters for the Monte Carlo simulations of W44. The plots show the distribution of best fit (a) flux (b) spectral index and (c) 68% containment radius. The dashed vertical lines represent the simulated values of the parameters.	74

5.8	The detection threshold to resolve an extended source with a uniform disk model for a two-year exposure. All sources have an assumed power-law spectrum and the different line styles (colors in the electronic version) correspond to different simulated spectral indices. The lines with no markers correspond to the detection threshold using photons with energies between 100 MeV and 100 GeV, while the lines with star-shaped markers correspond to the threshold using photons with energies between 1 GeV and 100 GeV.	75
5.9	The LAT detection threshold for four spectral indices and three backgrounds ($1\times$, $10\times$, and $100\times$ the Sreekumar-like isotropic background) for a two-year exposure. The left-hand plots are the detection threshold when using photons with energies between 1 GeV and 100 GeV and the right-hand plots are the detection threshold when using photons with energies between 10 GeV and 100 GeV. The flux is integrated only in the selected energy range. Overlaid on this plot are the LAT-detected extended sources placed by the magnitude of the nearby Galactic diffuse emission and the energy range they were analyzed with. The star-shaped markers (colored red in the electronic version) are sources with a spectral index closer to 1.5, the triangular markers (colored blue) an index closer to 2, and the circular markers (colored green) an index closer to 2.5. The triangular marker in plot (d) below the sensitivity line is MSH 15–52.	76

5.10	The projected detection threshold of the LAT to extension after 10 years for a power-law source of spectral index 2 against 10 times the isotropic background in the energy range from 1 GeV to 100 GeV (solid line colored red in the electronic version) and 10 GeV to 100 GeV (dashed line colored blue). The shaded gray regions represent the detection threshold assuming the sensitivity improves from 2 to 10 years by the square root of the exposure (top edge) and linearly with exposure (bottom edge). The lower plot shows the factor increase in sensitivity. For small extended sources, the detection threshold of the LAT to the extension of a source will improve by a factor larger than the square root of the exposure.	79
5.11	(a) and (b) are the distribution of TS_{ext} and of $TS_{2\text{pts}}$ when fitting simulated spatially extended sources of varying sizes as both an extended source and as two point-like sources. (c) and (d) are the distribution of $TS_{\text{ext}} - TS_{2\text{pts}}$ for the same simulated sources. (a) and (c) represent sources fit in the 1 GeV to 100 GeV energy range and (b) and (d) represent sources fit in the 10 GeV to 100 GeV energy range. In (c) and (d), the plus-shaped markers (colored red in the electronic version) are fits where $TS_{\text{ext}} \geq 16$	80
5.12	The distribution of $TS_{\text{ext}} - TS_{2\text{pts}}$ when fitting two simulated point-like sources of varying separations as both an extended source and as two point-like sources. (a), and (b) represent simulations of two point-like sources with the same spectral index and (c) and (d) represent simulations of two point-like sources with different spectral indices. (a) and (c) fit the simulated sources in the 1 GeV to 100 GeV energy range and (b) and (d) fit in the 10 GeV to 100 GeV energy range. The plus-shaped markers (colored red in the electronic version) are fits where $TS_{\text{ext}} \geq 16$	81

5.13	The cumulative density of TS_{ext} for the 733 clean AGN in 2LAC that were significant above 1 GeV calculated with <code>pointlike</code> (dashed line colored blue in the electronic version) and with <code>gtlike</code> (solid line colored black). AGN are too far and too small to be resolved by the LAT. Therefore, the cumulative density of TS_{ext} is expected to follow a $\chi^2_1/2$ distribution (Equation ??, the dash-dotted line colored red).	82
5.14	A TS map generated for the region around the SNR IC 443 using photons with energies between 1 GeV and 100 GeV. (a) TS map after subtracting IC 443 modeled as a point-like source. (b) same as (a), but IC 443 modeled as an extended source. The cross represents the best fit position of IC 443.	84
5.15	A diffuse-emission-subtracted 1 GeV to 100 GeV counts map of the region around 2FGL J1856.2+0450c smoothed by a 0.1° 2D Gaussian kernel. The plus-shaped marker and circle (colored red in the online version) represent the center and size of the source fit with a radially-symmetric uniform disk spatial model. The black crosses represent the positions of other 2FGL sources. The extension is statistically significant, but the extension encompasses many 2FGL sources and the emission does not look to be uniform. Although the fit is statistically significant, it likely corresponds to residual features of inaccurately modeled diffuse emission picked up by the fit.	85

- 5.16 A diffuse-emission-subtracted 1 GeV to 100 GeV counts map of 2FGL J0823.0–4246 smoothed by a 0.1° 2D Gaussian kernel. The triangular marker (colored red in the online version) represents the 2FGL position of this source. The plus-shaped marker and the circle (colored red) represent the best fit position and extension of this source assuming a radially-symmetric uniform disk model. The two star-shaped markers (colored green) represent 2FGL sources that were removed from the background model. From left to right, these sources are 2FGL J0823.4–4305 and 2FGL J0821.0–4254. The lower right inset is the model predicted emission from a point-like source with the same spectrum as 2FGL J0823.4–4305 smoothed by the same kernel. This source is spatially coincident with the Puppis A SNR. The light blue contours correspond to the X-ray image of Puppis A observed by *ROSAT* (Petre et al. 1996). 89
- 5.17 The spectral energy distribution of the extended sources Puppis A (2FGL J0823.0–4246) and γ -Cygni (2FGL J2021.5+4026). The lines (colored red in the online version) are the best fit power-law spectral models of these sources. Puppis A has a spectral index of 2.21 ± 0.09 and γ -Cygni has an index of 2.42 ± 0.19 . The spectral errors are statistical only. The upper limit is at the 95% confidence level. . . . 90

- 5.18 A diffuse-emission-subtracted 10 GeV to 100 GeV counts map of 2FGL J0851.7–4635 smoothed by a $0^{\circ}25$ 2D Gaussian kernel. The triangular marker (colored red in the electronic version) represents the 2FGL position of this source. The plus-shaped marker and the circle (colored red) are the best fit position and extension of this source assuming a radially-symmetric uniform disk model. The three black crosses represent background 2FGL sources. The three star-shaped markers (colored green) represent other 2FGL sources that were removed from the background model. They are (from left to right) 2FGL J0853.5–4711, 2FGL J0855.4–4625, and 2FGL J0848.5–4535. The circular and square-shaped marker (colored blue) represents the 2FGL and relocalized position of another 2FGL source. This extended source is spatially coincident with the Vela Jr. SNR. The contours (colored light blue) correspond to the TeV image of Vela Jr. (Aharonian et al. 2007a). 91
- 5.19 A diffuse-emission-subtracted 10 GeV to 100 GeV counts map of 2FGL J1615.0–5051 (upper left) and 2FGL J1615.2–5138 (lower right) smoothed by a $0^{\circ}1$ 2D Gaussian kernel. The triangular markers (colored red in the electronic version) represent the 2FGL positions of these sources. The cross-shaped markers and the circles (colored red) represent the best fit positions and extensions of these sources assuming a radially symmetric uniform disk model. The two black crosses represent background 2FGL sources and the star-shaped marker (colored green) represents 2FGL J1614.9-5212, another 2FGL source that was removed from the background model. The contours (colored light blue) correspond to the TeV image of HESS J1616–508 (left) and HESS J1614–518 (right) (Aharonian et al. 2006d). 92

5.20	The spectral energy distribution of four extended sources associated with unidentified extended TeV sources. The black points with circular markers are obtained by the LAT. The points with plus-shaped markers (colored red in the electronic version) are for the associated H.E.S.S. sources. (a) the LAT SED of 2FGL J1615.0–5051 together with the H.E.S.S. SED of HESS J1616–508. (b) 2FGL J1615.2–5138 and HESS J1614–518. (c) 2FGL J1632.4–4753c and HESS J1632–478. (d) 2FGL J1837.3–0700c and HESS J1837–069. The H.E.S.S. data points are from (Aharonian et al. 2006d). Both LAT and H.E.S.S. spectral errors are statistical only.	93
5.21	A diffuse-emission-subtracted 1 GeV to 100 GeV counts map of (a) the region around 2FGL J1627.0–2425 smoothed by a 0°.1 2D Gaussian kernel and (b) with the emission from 2FGL J1625.7–2526 subtracted. The triangular marker (colored red in the online version) represents the 2FGL position of this source. The plus-shaped marker and the circle (colored red) represent the best fit position and extension of this source assuming a radially-symmetric uniform disk model and the black cross represents a background 2FGL source. The contours in (a) correspond to the 100 μm image observed by IRAS (Young et al. 1986). The contours in (b) correspond to CO ($J = 1 \rightarrow 0$) emission integrated from -8 km s^{-1} to 20 km s^{-1} . They are from de Geus et al. (1990), were cleaned using the moment-masking technique (Dame 2011), and have been smoothed by a 0°.25 2D Gaussian kernel.	94

- 5.22 A diffuse-emission-subtracted 10 GeV to 100 GeV counts map of 2FGL J1632.4–4753c (a) smoothed by a $0^{\circ}.1$ 2D Gaussian kernel and (b) with the emission from the background sources subtracted. The triangular marker (colored red in the electronic version) represents the 2FGL position of this source. The plus-shaped marker and the circle (colored red) are the best fit position and extension of 2FGL J1632.4–4753c assuming a radially-symmetric uniform disk model. The four black crosses represent background 2FGL sources subtracted in (b). The circular and square-shaped markers (colored blue) represent the 2FGL and relocalized positions respectively of two additional background 2FGL sources subtracted in (b). The star-shaped marker (colored green) represents 2FGL J1634.4–4743c, another 2FGL source that was removed from the background model. The contours (colored light blue) correspond to the TeV image of HESS J1632–478 (Aharonian et al. 2006d). . . . 95
- 5.23 A diffuse-emission-subtracted 10 GeV to 100 GeV counts map of 2FGL J1712.4–3941 (a) smoothed by a $0^{\circ}.15$ 2D Gaussian kernel and (b) with the emission from the background sources subtracted. This source is spatially coincident with RX J1713.7–3946 and was recently studied in Abdo et al. (2011). The triangular marker (colored red in the online version) represents the 2FGL position of this source. The plus-shaped marker and the circle (colored red) are the best fit position and extension of this source assuming a radially symmetric uniform disk model. The two black crosses represent background 2FGL sources subtracted in (b). The contours (colored light blue) correspond to the TeV image (Aharonian et al. 2007b). 96

- 5.24 A diffuse-emission-subtracted 10 GeV to 100 GeV counts map of the region around 2FGL J1837.3–0700c (a) smoothed by a $0^\circ.15$ 2D Gaussian kernel and (b) with the emission from the background sources subtracted. The triangular marker (colored red in the online version) represents the 2FGL position of this source. The plus-shaped marker and the circle (colored red) represent the best fit position and extension of 2FGL J1837.3–0700c assuming a radially-symmetric uniform disk model. The circular and square-shaped markers (colored blue) represent the 2FGL and the relocalized positions respectively of two background 2FGL sources subtracted in (b). The star-shaped marker (colored green) represents 2FGL J1835.5–0649, another 2FGL source that was removed from the background model. The contours (colored light blue) correspond to the TeV image of HESS J1837–069 (Aharonian et al. 2006d). The diamond-shaped marker (colored orange) represents the position of PSR J1838–0655 and the hexagonal-shaped marker (colored purple) represents the position AX J1837.3–0652 (Gotthelf & Halpern 2008). 97
- 5.25 A diffuse-emission-subtracted 10 GeV to 100 GeV counts map of the region around 2FGL J2021.5+4026 smoothed by a $0^\circ.1$ 2D Gaussian kernel. The triangular marker (colored red in the online version) represents the 2FGL position of this source. The plus-shaped marker and the circle (colored red) represent the best fit position and extension of 2FGL J2021.5+4026 assuming a radially-symmetric uniform disk model. The star-shaped marker (colored green) represents 2FGL J2019.1+4040, a 2FGL source that was removed from the background model. 2FGL J2021.5+4026 is spatially coincident with the γ -Cygni SNR. The contours (colored light blue) correspond to the 408MHz image of γ -Cygni observed by the Canadian Galactic Plane Survey (Taylor et al. 2003). 98

5.26	The 21 spatially extended sources detected by the LAT at GeV energies with 2 years of data. The twelve extended sources included in 2FGL are represented by the circular markers (colored red in the on-line version). The nine new extended sources are represented by the triangular markers (colored orange). The source positions are overlaid on a 100 MeV to 100 GeV Aitoff projection sky map of the LAT data in Galactic coordinates.	99
5.27	A comparison of the sizes of extended sources detected at both GeV and TeV energies. The TeV sizes of W30, 2FGL J1837.3–0700c, 2FGL J1632.4–4753c, 2FGL J1615.0–5051, and 2FGL J1615.2–5138 are from Aharonian et al. (2006d). The TeV sizes of MSH 15–52, HESS J1825–137, Vela X, Vela Jr., RX J1713.7–3946 and W28 are from Aharonian et al. (2005, 2006b,c, 2007a,b, 2008). The TeV size of IC 443 is from Acciari et al. (2009) and W51C is from Krause et al. (2011). The TeV sizes of MSH 15–52, HESS J1614–518, HESS J1632–478, and HESS J1837–069 have only been reported with an elliptical 2D Gaussian fit and so the plotted sizes are the geometric mean of the semi-major and semi-minor axis. The LAT extension of Vela X is from Abdo et al. (2010). The TeV sources were fit assuming a 2D Gaussian surface brightness profile so the plotted GeV and TeV extensions were first converted to r_{68} (see Section ??). Because of their large sizes, the shape of RX J1713.7–3946 and Vela Jr. were not directly fit at TeV energies and so are not included in this comparison. On the other hand, dedicated publications by the LAT collaboration on these sources showed that their morphologies are consistent (Abdo et al. 2011; Tanaka et al. 2011). The LAT extension errors are the statistical and systematic errors added in quadrature.	100

5.28	The distributions of the sizes of 18 extended LAT sources at GeV energies (colored blue in the electronic version) and the sizes of the 40 extended H.E.S.S. sources at TeV energies (colored red). The H.E.S.S. sources were fit with a 2D Gaussian surface brightness profile so the LAT and H.E.S.S. sizes were first converted to r_{68} . The GeV size of Vela X is taken from Abdo et al. (2010). Because of their large sizes, the shape of RX J1713.7–3946 and Vela Jr. were not directly fit at TeV energies and are not included in this comparison. Centaurus A is not included because of its large size.	101
5.29	The distribution of spectral indices of the 1873 2FGL sources (colored red in the electronic version) and the 21 spatially extended sources (colored blue). The index of Centaurus A is taken from Nolan et al. (2012) and the index of Vela X is taken from Abdo et al. (2010). . .	102

List of Acronyms

2CG the second COS-B catalog. 8

2FGL the second *Fermi* catalog. 21, 36

2PC the second *Fermi* pulsar catalog. 22

3EG the Third EGRET Catalog. 9

ACD Anti-Coincidence Detector. 11

arcsec second of arc. 31

BPL broken-power law. 38

CGRO the Compton Gamma Ray Observatory. 8

CGS the Centimetre-Gram-Second System of Units. 38, 39

ECPL exponentially-cutoff power law. 38, 39

EGRET the Energetic Gamma Ray Experiment Telescope. 8–10

ESA the European Space Agency. 8

FWHM full width at half maximum. 6

GBM Gamma-ray Burst Monitor. 11

IC inverse Compton. 4, 18, 19, 30, 31, 34

LAT the Large Area Telescope. iv, v, 11, 21, 22, 105

MIT the Massachusetts Institute of Technology. 6, 12

MSP millisecond pulsar. 26

NASA the National Aeronautics and Space Administration. 7, 8

NRL the Naval Research Laboratory. 12

NS neutron star. 12, 24, 25, 28, 29

OSO-3 the Third Orbiting Solar Observatory. 6, 7, 20

PL power law. 38, 39

PWN pulsar wind nebula. iv, v, 5, 13, 24, 28, 30–34, 105

SA solid angle. 40, 41

SAS-2 the second Small Astronomy Satellite. 7, 8

SNR supernova remnant. 28, 30, 31, 39

Chapter 1

Overview

In Chapter 2, we discuss the history of γ -ray astrophysics, ...

Chapter 2

Gamma-ray Astrophysics

2.1 Astronomy and the Atmosphere

Humans surely have, since the very beginning, stared into space and contemplated its brilliance. Stone circles in the Nabta Playa in Egypt are likely the first observed astronomical observatory and are believed to have acted as a prehistoric calendar. Dating back to the 5th century BC, they are 1,000 years older than stonehenge (McK Mahille et al. 2007).

Astronomy has historically been almost entirely concerned with studying the photons that arrive from outer space. Because of their charge neutrality, photons are not deflected by intergalactic electric and magnetic fields and therefore point back to the objects emitting them.

Historically, the field of astronomy concerned the study of visible light. The reason for this is visible light is not significantly absorbed in the atmosphere. In addition to the visible spectrum, radio waves, some energies of infrared radiation, and long-wavelength ultraviolet radiation can be measured from the ground. Figure 2.1 shows the transparency of the atmosphere of the earth to photons of different wavelengths.

Slowly, over time, astronomers expanded their view across the electromagnetic spectrum. First, the astronomical observations were made from the ground. Infrared radiation from the sun was first observed by William Herschel in 1800. Herschel

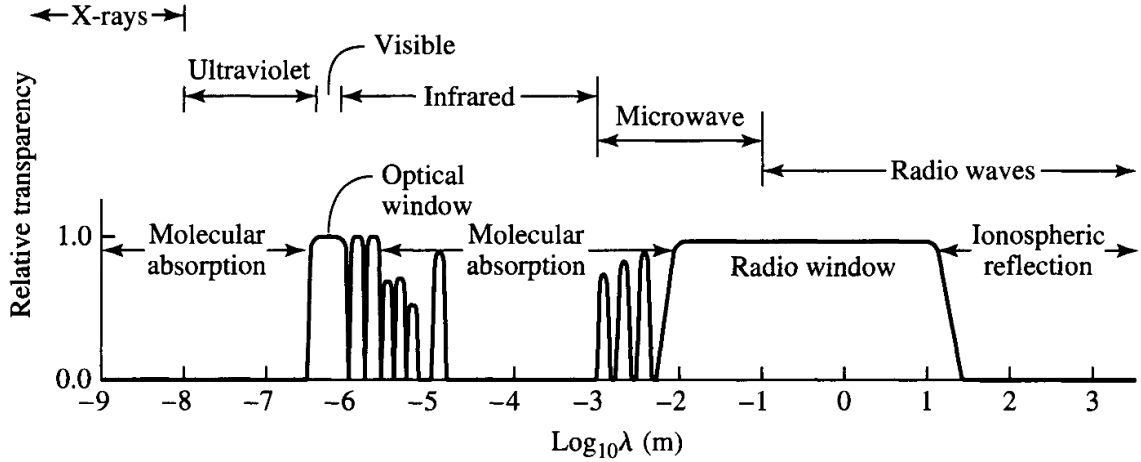


Figure 2.1 Transparency of the atmosphere of the earth to photons of varying wavelengths. This figure is from Carroll & Ostlie (2006)

measured this infrared radiation by measuring the temperature of sunlight through a prism and extending the measurement past the red part of the spectrum (Herschel 1800). The first extraterrestrial source of radio waves was detected by Jansky in 1933. Jansky, a radio engineer at Bell labs, was studying the origins of radio interference when he detected radio emission towards the center of our galaxy. (Jansky 1933).

The expansion of the astronomical frontiere to other wavelengths required the development of rockets and satellites in the 20th century. The first ultraviolet observation of the sun was performed in 1946 from a captured V-2 rocket (Baum et al. 1946). Observations of solar x-rays were also first carried out on a captured V-2 Rocket in 1949 (Burnight 1949).

2.2 The History of Gamma-ray Astrophysics

It was only natural to wonder about photons with even higher energies. These higher energy photons must come from more extreme processes in space.

As is common in the field of physics, the prediction of the detection of cosmic γ -rays far preceded their discovery. Feenberg & Primakoff (1948) theorized that

the interaction of starlight with cosmic rays could produce γ -rays through inverse Compton (IC) upscattering. Following the discovery of the neutral pion in 1949, Hayakawa (1952) predicted that γ -ray emission could be observed from the decay of neutral pions when cosmic rays interacted with interstellar matter. And in the same year, Hutchinson (1952) discussed the bremsstrahlung radiation of cosmic-ray electrons. Morrison (1958) first predicted the detection of several sources of γ -rays including solar flares, pulsar wind nebulae (PWNe), and active galaxies.

Attempts were made in the 1940s and 1950s to determine the composition of cosmic rays using balloon-based experiments. See, for example Critchfield et al. (1952) and Hulsizer & Rossi (1948). But the attempt to observe cosmic γ -rays was hampered by the strong background of atmospheric albedo γ -rays.

The first space-based γ -ray detector was Explorer XI Kraushaar et al. (1965). It was developed at the Massachusetts Institute of Technology (MITs) under the direction of William L. Kraushaar. Explorer XI incorporated five alternating slabs of cesium iodide and sodium iodide which would induce a gamma-ray to pair-convert into an electron positron pair. The electron and positron pair would then travel through a sandwich scintillation detector. A scintillator is a crystalline material that emits low-energy photons when a high-energy charged particle travels through it. A Cherenkov counter below the scintillation detector measured these low-energy photons, which allowed for the measurement of the energy of the γ -rays. This experiment was surrounded by a plastic anticoincidence scintillation counter which allowed for the rejection of background particles. Figure 2.2 shows the experimental design of Explorer XI.

Explorer XI operated in the energy range above 100 MeV. It had an area of $\sim 45\text{cm}^2$ but an effective area of only $\sim 7\text{cm}^2$, corresponding to a detector efficiency of $\sim 15\%$.

It was launched on board Explorer XI on April 27, 1961. The instrument was in operation for 7 months, but only 141 hours of data were of acceptable quality. Using these observations, Explorer XI observed 31 γ -rays and, because the distribution a distribution of these γ -rays was consistent with being isotropic, the experiment could not firmly identify the γ -rays as being cosmic in nature.

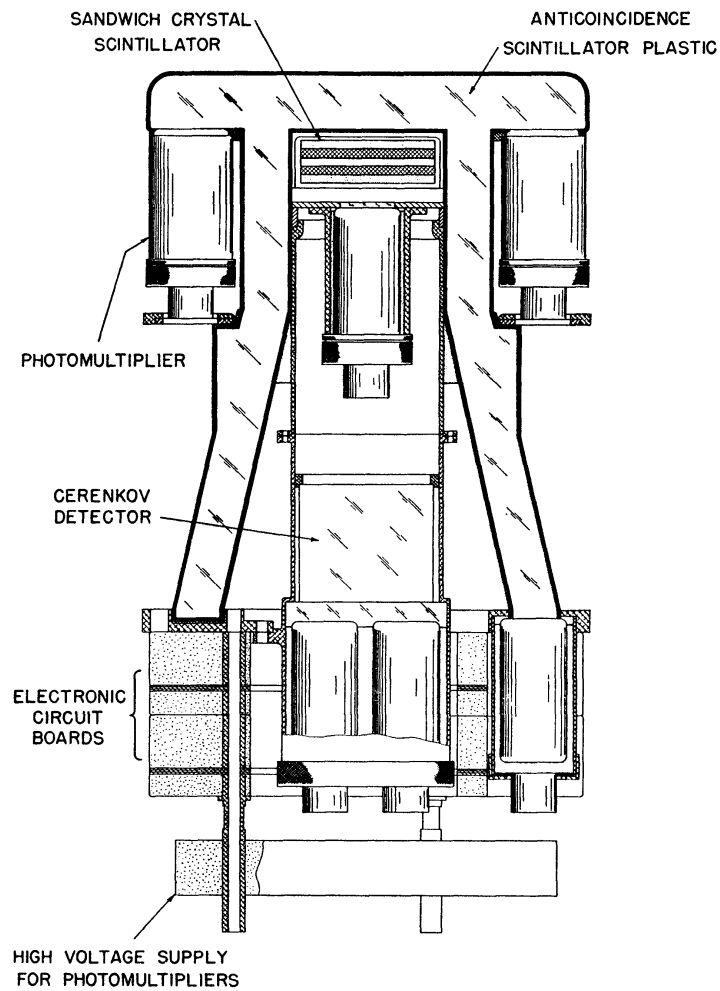


Figure 2.2 The experimental design of Explorer XI. This figure is from Kraushaar et al. (1965).

The first definitive detection of γ -ray came in 1962 by an experiment on the Ranger 3 moon probe (Arnold et al. 1962). It detected an isotropic flux of γ -rays in the 0.5 MeV to 2.1 MeV energy range.

The Third Orbiting Solar Observatory (OSO-3), also developed by Kraushaar, was the next major astrophysical γ -ray detector (Kraushaar et al. 1972). OSO-3 allowed the on board γ -ray detected to have an improved weight, power, telemetry, and exposure, creating a more sensitive experiment. The experiment operated in the energy range from 50 MeV to ~ 400 MeV, had an effective area $\sim 9 \text{ cm}^2$, and had a angular resolution of $\sim 24^\circ$ at its full width at half maximum (FWHM).

OSO-3 was launched on March 8, 1967 and operated for 16 months, measuring 621 cosmic γ -rays. The most important result of the experiment was to measure a strong anisotropy in the distribution of the γ -rays with a strong clustering of γ -rays towards the Galactic plane. Figure 2.2 shows a sky map of these γ -rays. This experiment confirmed both a Galactic component to the γ -ray sky as well as an additional isotropic component, hypothesised to be extragalactic in origin.

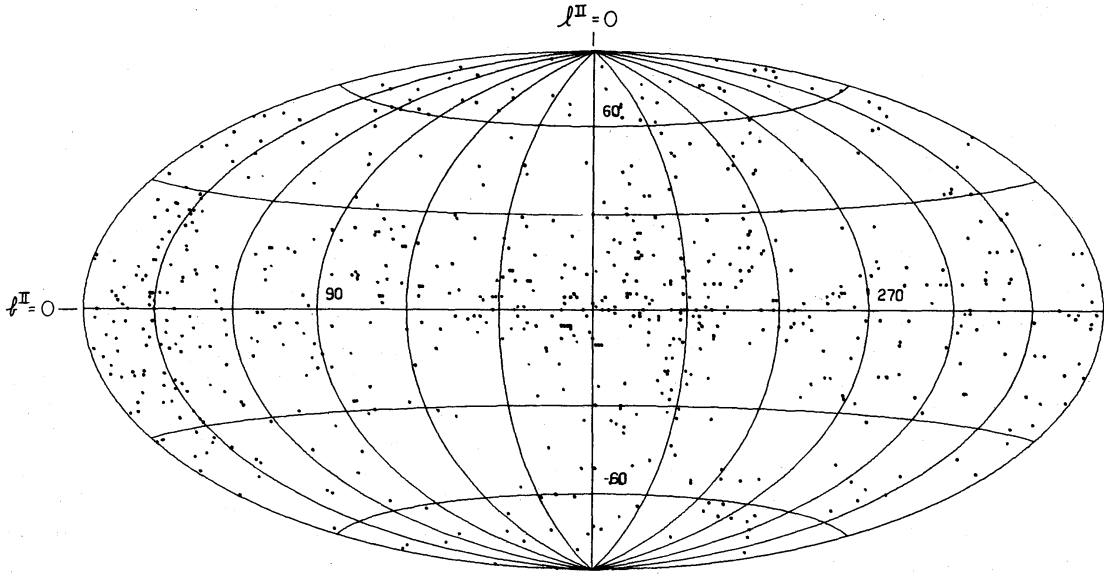


Figure 2.3 The position of all 621 cosmic γ -rays detected by OSO-3. This figure is from Kraushaar et al. (1972).

The major discovery by OSO-3 was confirmed by a balloon-based γ -ray detector in 1970 (Kniffen & Fichtel 1970). In the following year, the first γ -ray pulsar (the Crab) was detected by another balloon-based detector Browning et al. (1971).

The next major advancement in γ -ray astronomy came the second Small Astronomy Satellite (SAS-2) and COS-B.

SAS-2 was a dedicated γ -ray detector launched by the National Aeronautics and Space Administration (NASA) in November 15, 1972. SAS-2 was Fichtel et al. (1975). It improved upon OSO-3 by incorporating a spark chamber and having an overall larger size. The size of the active area of the detector was 640 cm^2 and the experiment had a much improved effective area of $\sim 115 \text{ cm}^2$. The spark chamber allowed for a separate measurement of the electron and positron tracks, which allowed for improved directional reconstruction of the incident γ -ray. SAS-2 had a PSF $\sim 5^\circ$ at 30 MeV and $\sim 1^\circ$ at 1 GeV.

SAS-2 collected data for over 6 months before a power supply failure ended data collection. SAS-2 Observed over 8,000 γ -ray photons covering $\sim 55\%$ of the sky including most of the Galactic plane. SAS-2 discovered strong emission along the Galactic plane and particularly towards the Galactic center. It also discovered pulsations from the Crab (Fichtel et al. 1975) and Vela pulsar (Thompson et al. 1977b). In addition, SAS-2 discovered Geminga, the first γ -ray source with no compelling multiwavelength counterpart (Thompson et al. 1977a). Geminga was eventually discovered to be a pulsar by the Energetic Gamma Ray Experiment Telescope (EGRET) (Bertsch et al. 1992) and retroactively by SAS-2 (Mattox et al. 1992).

on August 9, 1975, the European Space Agency (ESA) launched COS-B, a γ -ray detector similar to SAS-2. COS-B included a spark chamber but improved upon the design of SAS-2 by including a calorimeter below the spark chamber which improved the energy resolution to $< 100\%$ for energies $\sim 3 \text{ GeV}$ (Bignami et al. 1975). COS-B has a comparable effective area to SAS-2: $\sim 50 \text{ cm}^2$ at $\sim 400 \text{ MeV}$ (Bignami et al. 1975).

COS-B operated successfully for over 6 years and produced the first detailed catalog of the γ -ray sky. In total, COS-B observed $\sim 80,000$ photons Mayer-Hasselwander et al. (1982). The second COS-B catalog (2CG) detailed the detection 25 γ -ray sources

for $E > 100$ MeV (Swanenburg et al. 1981). Figure 2.2 shows a map of these sources. Of these sources, the vast majority lay along the galactic plane and could not be positively identified with sources observed at other wavelengths. In addition, COS-B observed the first ever extragalactic γ -ray source, (3C273, Swanenburg et al. 1978).

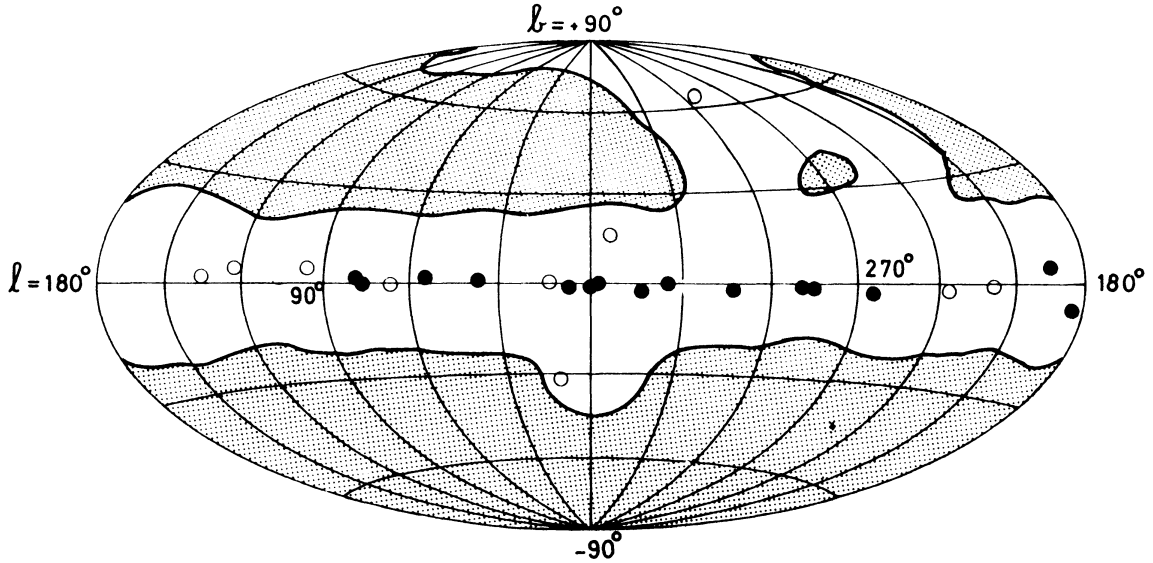


Figure 2.4 A map of the sources observed by COS-B. The filled circles represent brighter sources. The unshaded region corresponds to the parts of the sky observed by COS-B. This figure is from Swanenburg et al. (1981).

The next major γ -ray experiment was EGRET. It was launched on board the Compton Gamma Ray Observatory (CGRO) in April, 1991. CGRO was second of the Great Observatories satellites launched by NASAs. EGRET had a design similar to SAS-2, but had an expanded energy range, operating from 20 MeV to 30 GeV, an improved effective area of $\sim 1500 \text{ cm}^2$ from ~ 500 MeV to ~ 1 GeV, and an improved angular resolution, decreasing to $\sim 0.5^\circ$ at its highest energies Thompson et al. (1993).

At the time, CGRO was the heaviest astrophysical experiment launched into orbit, weighting $\sim 17,000$ kg. EGRET contributed $\sim 6,000$ kg to the mass of CGRO.

EGRET vastly expanded the field of γ -ray astronomy. EGRET detected six pulsars (Nolan et al. 1996) and also the Crab Nebula Nolan et al. (1993). EGRET also detected the LMC, the first normal galaxy outside of our galaxy to be detected at

γ -rays (Sreekumar et al. 1992). EGRET also detected Centarus A, the first radio galaxy detected at γ -rays Sreekumar et al. (1999). In total, EGRET detected 271 γ -ray sources using 4 years. The results were presented in the Third EGRET Catalog (3EG) (Hartman et al. 1999). This catalog included 66 high confidence blazar identifications and 27 low-confidence AGN identifications. Figure 2.2 plots the position of the sources observed by EGRET.

In total, EGRET detected over 1,500,000 celestial gamma rays Thompson (2008).

EGRET was designed with a 2 year mission lifetime, but operated for 9 years. Over time, the performance of EGRET degraded due to hardware failure and due to having to replenish gas in the spark chamber Esposito et al. (1999).

Get a picture of EGRET to include

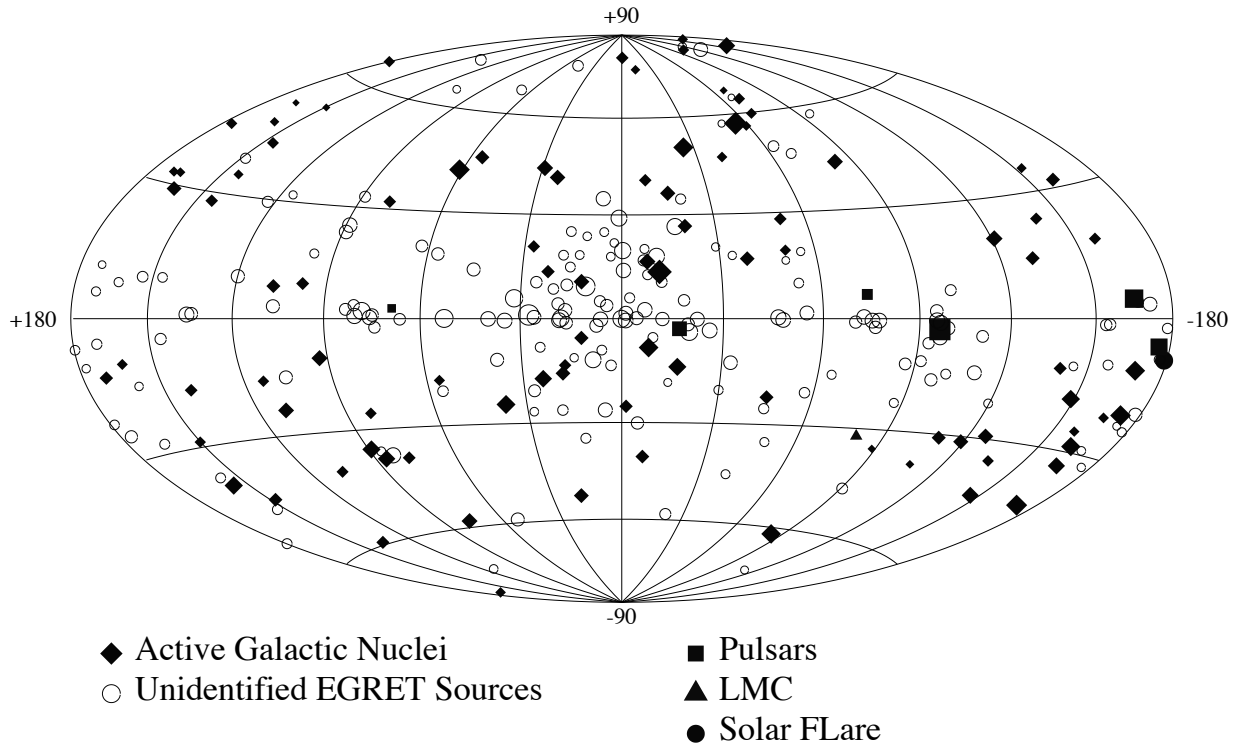


Figure 2.5 The position of EGRET sources in the sky in galactic coordinates. The size of the source markers corresponds to the overall source intensity. This figure is from (Hartman et al. 1999).

- AGILE
 - *Fermi*
 - Short description of the history of TeV astronomy
 - A detailed description of *Fermi* detector will be presented in Section 2.3.4.
 - The major source classes detected by *Fermi* will be presented in Section 2.7
- The principles of the detector will be described in Section 2.3.4.

What is the LAT effective area?

2.3 The *Fermi* Gamma-ray Space Telescope

The Large Area Telescope (LAT) is a pair-production telescope

2.3.1 The Tracker

2.3.2 The Calorimeter

2.3.3 Anti-Coincidence Detector

The Anti-Coincidence Detector (ACD) is ...

2.3.4 Gamma-ray Burst Monitor

2.4 Astrophysical Sources of Gamma-rays

2.4.1 Pulsars

“The gravitational collapse of the core of a massive star into a neutron star (e.g., Baade & Zwicky 1934) releases enough energy to power a supernova explosion (e.g., Zwicky 1938).” – gelfand_2009_dynamical-model

“First widely accepted prediction of an ultra-dense star was given by Zwicky and Baade (1934). Proposed the idea that a supernova represents the transition of an ordinary star into a neutron star, consisting mainly of neutrons.” – <http://www.atnf.csiro.au/research/pulsar/orange10/pdf/RaiYuenOrange2010.pdf>

Pulsars were first discovered in 1967 by Jocelyn Bell Burnell and Antony Hewish (Hewish et al. 1968). They had constructed a radio telescope that used interplanetary scintillation with the intention of observing quasars. In the process, they detected a source with a periodicity of 1.3 s.

Make note of “Air force had early warning of pulsars” paper

Even before the discovery, Pacini (1967) had predicted the existence of neutron stars (NSs). Shortly following the 1967 discovery, Gold (1968) and Pacini (1968) argued that the observed pulsar was a rotating NS.

The discovery of many more pulsars came quickly. In 1968, the Vela pulsar (Large et al. 1968) and the Crab pulsar (Staelin & Reifenstein 1968) were discovered.

The first pulsar observed at optical frequencies was the Crab, discovered in 1969 shortly after its radio discovery (Cocke et al. 1969). In the same year, the first X-ray pulsations were discovered from the same source. At the time, there were no space-based X-ray observatories, so observations had to be performed from rockets. The discovery was carried out almost concurrently by a group at the Naval Research Laboratory (NRL) (Fritz et al. 1969) and at MIT (Bradt et al. 1969). Using proportional counters, these experiments showed that the pulsed emission from the Crab extended to X-ray energies and that, for this source, the X-rays emission was a factor > 100 more energetic than the observed visible emission.

- I read somewhere, but don’t have the reference (it was one of those verbose history books on pulsars), that originally the neutron star hypothesis wasn’t well accepted. But then one pulsar was found with a very short period (I think the Crab) which, for causality reasons, had to be small enough that it seemed to confirm the Neutron star hypothesis.
- For Crab describe spin down?: “and these pulsations were then shown to be slowing down at a rate of 36 ns per day (Richards & Comella 1969).” – Gaensler

& Slane (2006)

As was discussed in Section 2.2, γ -ray emission from the Crab was detected only 2 years later (Browning et al. 1971).

ATNF catalog?

- “There are currently more than 1,800 pulsars in the ATNF on-line catalog [Manchester et al., 2005], with rotation periods in the range 0.0016-12 seconds (Figure 3.1) and derived spin down luminosities in the range XXX - XXX erg/s.”
– dalton_2011_identification-gamma-ray

EGRET pulsars?

The state of the art in γ -ray detection of pulsars will be included in an upcoming publication. 2PC: Section 2.7.2

When was the PSR, PWN connection made

First
gamma-
ray
detec-
tion

2.4.2 Pulsar Wind Nebulae

A PWN is a diffuse nebula of shocked relativistic particles. A PWNs surrounds and is powered by an accompanying pulsar. PWNs have been observed long before the discovery of pulsars, but the pulsar/PWN connection could not be made until after the detection of pulsars.

The most famous PWNs is the Crab nebula, associated with the Crab pulsar.

- Chinese SN observations of Crab Nebulae: (p128 of “The Crab Nebula: An Astrophysical Chimera”) “It was probably also recorded by Anasazi Indian artists (in present-day Arizona and New Mexico), as findings in Navaho Canyon and White Mesa (both Arizona) as well as in the Chaco Canyon National Park (New Mexico) indicate; there’s a review of the research on the Chaco Canyon Anasazi art online. In addition, Ralph R. Robbins of the University of Texas has found Mimbres Indian art from New Mexico, possibly depicting the supernova.”
– <http://messier.seds.org/m/m001.html>

It was discovered in 1731 by physician and amateur astronomer John Bevis. This source was going to be published in his sky atlas *Uranographia Britannica*, but the work was never published because his published filed for bankruptcy in 1750. Figure 2.4.2 shows Beavis' plate containing the Crab nebula. A detailed history of John Bevis' work can be found in Ashworth (1981).

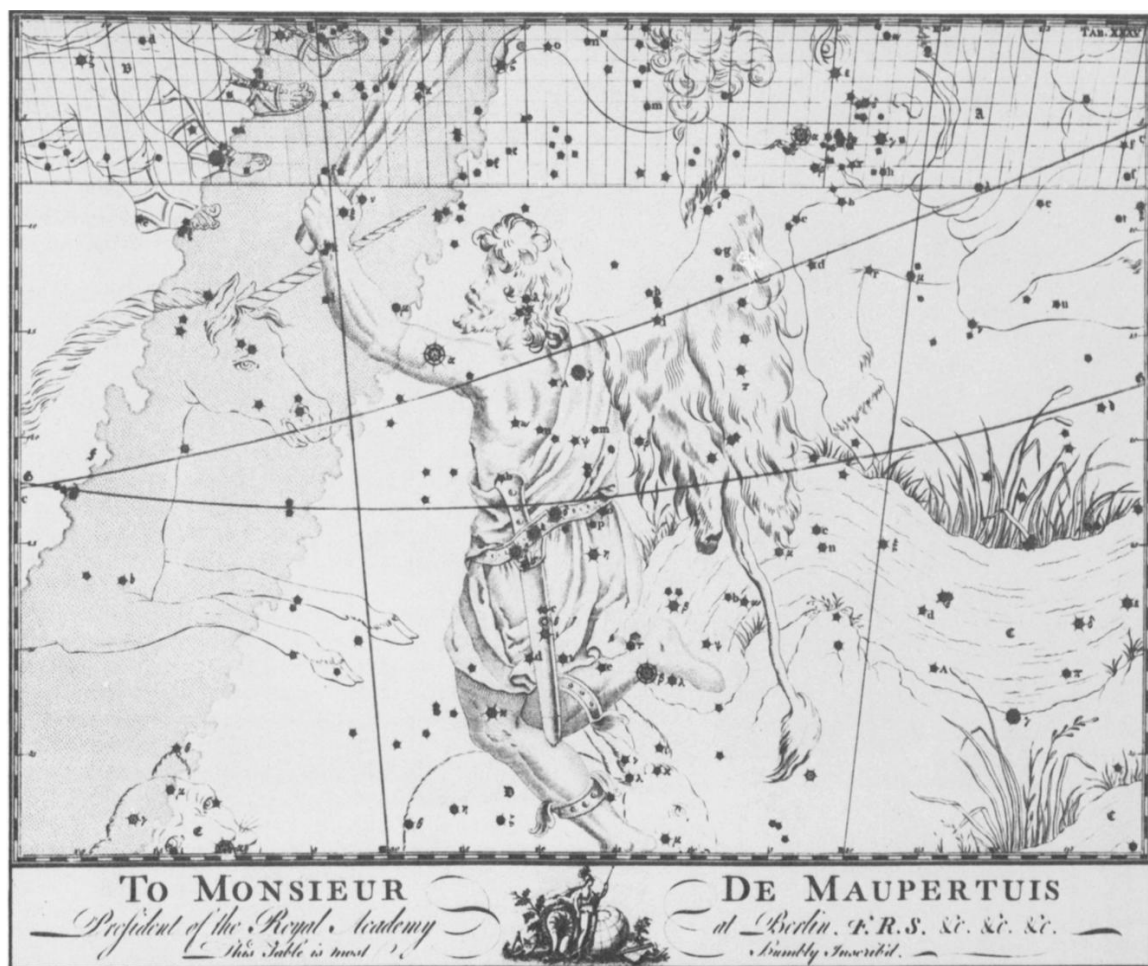


Figure 2.6 The Orion plate from Bevis' book *Uranographia Britannica*. The Crab nebula can be found on the horn of Taurus the Bull on the top of the figure and the source is marked by a cloudy symbol. This figure was reproduced from Ashworth (1981).

- Crab Nebulae is M1 in Charles Messier's catalog 1758 (p128 of "The Crab

Nebula: An Astrophysical Chimera”)

- Connection to 1054: “Lundmark (1921) suggested a connection between the Crab Nebula and the event of 1054 AD” (p128 of “The Crab Nebula: An Astrophysical Chimera”) “The Crab Nebula (Fig. 1) is almost certainly associated with a supernova (SN) explosion observed in 1054 CE (Stephenson & Green 2002, and references therein).” – “The Evolution and Structure of Pulsar Wind Nebulae” Bryan M. Gaensler and Patrick O. Slane
- “The same year, J.C. Duncan of Mt. Wilson Observatory compared photographic plates taken 11.5 years apart, and found that the Crab Nebula was expanding at an average of about 0.2” per year; backtracing of this motion showed that this expansion must have begun about 900 years ago (Duncan 1921). Also the same year, Knut Lundmark noted the proximity of the nebula to the 1054 supernova (Lundmark 1921).” – <http://messier.seds.org/m/m001.html> “In 1942, based on investigations with the 100-inch Hooker telescope on Mt. Wilson, Walter Baade computed a more accurate figure of 760 years age from the expansion, which yields a starting date around 1180 (Baade 1942); later investigations improved this value to about 1140. The actual 1054 occurrence of the supernova shows that the expansion must have been accelerated.” – <http://messier.seds.org/m/m001.html>
- “but it was not until 1942 that Duyvendak (1942) and Mayall & Oort (1942) presented complete studies of modern observations of the expanding nebula and of the early Chinese records. It was this work that established unambiguously that the Crab is the remnant of SN1054.” (p128 of “The Crab Nebula: An Astrophysical Chimera”)
- “1949, the Crab nebula was identified as a strong source of radio radiation (Bolton et.al. 1949), discovered 1948 named and listed as Taurus A (Bolton 1948), and later as 3C 144.” - <http://messier.seds.org/m/m001.html>
- Synchrotron emission hypothesis: “while the inner, blueish nebula emits continuous light consisting of highly polarised so-called synchrotron radiation, which is

- The non-thermal radiation processes typical in astrophysics are most comonly

2.5.1 Synchrotron

Get image of Synchrotron radiation (from R&L to include in discussion.

The synchrotron radiation processes is commonly observed in astrophysics. It is caused when charged particles, typically electrons, spiral around magnetic field lines.

This emission is discussed thoroughly in Blumenthal & Gould (1970) and Rybicki & Lightman (1979). In what follows, we adopt the notation from Houck & Allen (2006).

A charged particle of mass m and charge q in a magnetic field of strength \mathbf{B} will experince an electromagnetic force:

$$\frac{d}{dt}(\gamma m \mathbf{v}) = \frac{q}{c} \mathbf{v} \times \mathbf{B} \quad (2.1)$$

This force will cause a particle to accelerate around the magnetic field lines, causing it to radiate by maxwell's equations.

The power emitted at a frequency ν by particle spiraling will be

$$P_{\text{emitted}}(\nu) = \frac{\sqrt{3} q^3 B \sin \alpha}{mc^2} F(\nu/\nu_c) \quad (2.2)$$

where α is the angle between the particle's velocity vector and magnetic field vector. Here,

$$F(x) \equiv x \int_x^\infty K_{\frac{5}{3}}(\xi) d\xi, \quad (2.3)$$

and

$$\nu_c = \frac{3qB\gamma^2}{4\pi mc} \sin \alpha \equiv \nu_0 \gamma^2 \sin \alpha \quad (2.4)$$

Because power is inversely-proportional to mass, synchotron radiation is almost always assumed to come from electrons.

Now, we assume a population of particles and compute the total emission. We say that $N(p, \alpha)$ is the number of particles per unit momentum and solid angle with a momentum p and pitch angle α .

We find the total power emitted by integrating over particle momentum and distribution

$$\frac{dW}{dt} = \int dp \int d\vec{\Omega} P_{\text{emitted}}(\nu) N(p, \alpha) \quad (2.5)$$

If we assume the pitch angles of the particles to be isotropically distributed and include Equation 2.2, we find that the photon emission per unit energy and time is

$$\frac{dN}{d\omega dt} = \frac{\sqrt{3}q^3 B}{hm_e c^2 \omega} \int dp N(p) R\left(\frac{\omega}{\omega_0 \gamma^2}\right) \quad (2.6)$$

where

$$R(x) \equiv \frac{1}{2} \int_0^\pi d\alpha \sin^2 \alpha F\left(\frac{x}{\sin \alpha}\right) \quad (2.7)$$

It is typical in astrophysics to assume a power-law distribution of electrons written as

$$N(p) dp = \kappa p^{-\gamma} dp. \quad (2.8)$$

For a powerlaw distribution of photons integrated over pitch angle, we find

$$P_{\text{tot}}(\omega) \propto \kappa B^{(p+1)/2} \omega^{-(p-1)/2}. \quad (2.9)$$

See, Rybicki & Lightman (1979) or Longair (2011) for a full derivation. This shows that, assuming a power-law electron distribution, the electron spectral index can be related to the photon spectral index.

2.5.2 Inverse Compton

Normal compoton scattering involves a photon colliding with a free electron and transferring energy to it. In IC scattering, a high-energy electron interacts with a low-energy photon imparting energy to it. This process occurs when highly-energetic electrons interact with a dense photon field.

The derivation of IC emission requires a quantum electrodynamical treatment. It was first computed in Klein & Nishina (1929), and the derivation is described in Blumenthal & Gould (1970). In what follows, we follow the notational convention of

Houck & Allen (2006).

We assume a population of relativistic ($\gamma \gg 1$) electrons written as $N(p)$ which is contained inside isotropic photon distribution with number density $n(\omega_i)$.

The distribution of photons emitted by IC scatter is written as

$$\frac{dN}{d\omega dt} = c \int d\omega_i n(\omega_i) \int_{p_{\min}}^{\infty} dp N(p) \sigma_{\text{KN}}(\gamma, \omega_i, \omega) \quad (2.10)$$

where ω is the outgoing photon energy written in units of the electron rest mass energy, $\omega \equiv h\nu/(m_e c^2)$, and σ_{KN} is the Klein-Nishina cross section.

The Klein-Nishina cross section is

$$\sigma_{\text{KN}}(\gamma, \omega_i, \omega) = \frac{2\pi r_0^2}{\omega_i \gamma^2} \left[1 + q - 2q^2 + 2q \ln q + \frac{\tau^2 q^2 (1 - q)}{2(1 + \tau q)} \right] \quad (2.11)$$

Here,

$$q \equiv \frac{\omega}{4\omega_i \gamma (\gamma - \omega)}, \quad (2.12)$$

$\tau \equiv 4\omega_i \gamma$, and $r_0 = e^2/(m_e c^2)$ is the classical electron radius. The threshold electron lorentz factor is

$$\gamma_{\min} = \frac{1}{2} \left(\omega + \sqrt{\omega^2 + \frac{\omega}{\omega_i}} \right) \quad (2.13)$$

Typically, IC emission is assumed to originate when a power-law distribution of electrons (see Equation 2.8) interacts with a thermal photon distribution

$$n(\omega_i) = \frac{1}{\pi^2 \lambda^3} \frac{\omega_i^2}{e^{\omega_i/\Theta} - 1} \quad (2.14)$$

where $\lambda = \hbar/(m_e c)$ and $\Theta = kT/(m_e c^2)$. Typically, IC emission happens off CMB photons with $T = 2.725$ K. We conclude by noting that the free-parameters of IC emission are the the assumed particle spectrum and photon field.

2.5.3 Bremsstrahlung

Bremsstrahlung radiation is composed of electron-electron and electron-ion interactions. In either case, we assume a differential spectrum of accelerated electrons $N_e(E)$

that interacts with a target density of electrons (n_e) or ions (n_Z).

$$\frac{dN}{dEdt} = n_e \int dE N_e(E) v_e \frac{d\sigma_{ee}}{dE} + n_Z \int dE N_e(E) v_e \frac{d\sigma_{eZ}}{dE} \quad (2.15)$$

Here, v_e is the velocity of a the electron, and σ_{ee} and σ_{eZ} are the electron-electron and electron-ion cross sections.

The actual evaluation of these cross sections is quite involved. The electron-electron cross section was worked out in Haug (1975). The electron-ion cross section XXXXX.

We refer to Houck & Allen (2006) for a detailed description of the calculation of this cross section.

Why no Bremsstrahlung radiation from PWN. Maybe a back-of-the-envelope estimate

2.5.4 Pion Decay

Neutral pion decay occurs when highly-energetic protons interact with thermal protons. This emission happens when protons decay into neutral pions through $pp \rightarrow \pi^0 + X$ and subsequently decay through $\pi^0 \rightarrow 2\gamma$.

The gamma-ray emission from neutral pion decay can be computed as

$$\frac{dN}{dEdt} = n_H \int dE v_p N_p(E) \frac{d\sigma_{pp}}{dE} \quad (2.16)$$

Here, $N_p(E)$ is the differential proton distribution, σ_{pp} is gamma-ray cross section through proton-proton interactions, and n_H is the target hydrogen density.

Describe the characteristic pi0 cutoff energy

2.6 The Galactic Diffuse and Isotropic Gamma-ray Background

Include discussion of modeling, if time permitting

- Discuss the historical Observations of galactic diffuse emission
Mention how OSO-3 first detected the *gamma*-rays from the galaxy: Section 2.2.
- GALPROP model of diffuse emission. Reference: <http://arxiv.org/abs/1202.4039>
- Empirical Ring model of galactic diffuse emission.
- The isotropic background: <http://arxiv.org/abs/1002.3603>
- Galactic diffuse emission is primarily composed of ...
- Something about how great galprop is.
- Something about

2.7 Sources Detected by the Fermi the Large Area Telescope

- A variety of sources detected by the The Large Area Telescope:

2.7.1 The Second Fermi Catalog

The second *Fermi* catalog (2FGL) was a catalog by the LAT collaboration containing XXX Sources.

Describe Catalog

- Citation is Nolan et al. (2012)
- Source classification method
- Number of sources detected by the LAT
- Forward reference Chapter 4, which does a more thorough description of likelihood analysis method.
- Source classes/associations

2.7.2 The Second Fermi Pulsar Catalog

The second *Fermi* pulsar catalog (2PC) is a ...

- Process of detecting Pulsars with the LAT
- Number of pulsars detected by the LAT

2.7.3 Pulsar Wind Nebulae Detected by The Large Area Telescope

Crab

Vela X

MSH 15-52

Dig up HESS reference of HESS J1514-59.

HESS J1825–137

HESS J1825–137 is a cool source

HESS Detection: HESS Energy dependent morphology: Aharonian et al. (2006b)

LAT Detection: Grondin et al. (2011)

HESS J1640–465

HESS J1640–465 is also cool.

HESS detection: Aharonian et al. (2006d) Fermi detection: Slane et al. (2010)

2FGL J1857+026

2FGL J1857+026 is another good source.

LAT detection: Rousseau et al. (2012)

1. <http://arxiv.org/pdf/1206.3324v1.pdf>

J1023

...

Chapter 3

The Pulsar/Pulsar Wind Nebula System

3.1 Neutron Star Formation

As was discussed in Section 2.4, pulsars, PWNs, and supernova remnants are all the end products of supernovas. When a star undergoes a supernova, the ejecta forms a supernova remnant. If the remaining stellar core has a mass above the Chandrasekhar limit, then the core's electron degeneracy pressure cannot counteract the core's gravitational force and the core will collapse into a NS. The Chandrasekhar mass limit can be approximated as (Chandrasekhar 1931)

$$M_{\text{Ch}} \approx \frac{3\sqrt{2\pi}}{8} \left(\frac{\hbar c}{G} \right)^{3/2} \left[\left(\frac{Z}{A} \right) \frac{1}{m_{\text{H}}^2} \right] \quad (3.1)$$

where \hbar is the reduced Planck constant, c is the speed of light, G is the gravitational constant, m_{H} is the mass of hydrogen, Z is the number of protons, A is the number of nucleons, and M_{\odot} is the mass of the sun. This formula can be found in (Carroll & Ostlie 2006). When this formula is computed more exactly, one finds $M_{\text{Ch}} = 1.44M_{\odot}$.

Because NSs are supported by a neutron degeneracy pressure, the radius of a

neutron star can be approximated as

$$R_{\text{ns}} \approx \frac{(18\pi)^{2/3}}{10} \frac{\hbar^2}{GM_{\text{ns}}^{1/3}} \left(\frac{1}{m_{\text{H}}} \right)^{8/3} \quad (3.2)$$

This formula can be found in (Carroll & Ostlie 2006). The canonical radius for NSs is ~ 10 km.

In these very dense environments, the protons and electrons in the NS form into neutrons through inverse β decay:

$$p^+ + e^- \rightarrow n + \nu_e. \quad (3.3)$$

But if a NS had a sufficiently large mass, the gravitational force would overpower the neutron degeneracy pressure and the object would collapse into a black hole. The maximum mass of a NS is unknown because it depends on the equation of state inside the star, but is commonly predicted to be $\sim 2.5M_{\odot}$. Recently, a pulsar with a mass of $\sim 2M_{\odot}$ was discovered (Demorest et al. 2010), constraining theories of the equation of state.

In addition to rotationally-powered pulsars, the primary class of observed pulsars, there are two additional source classes of pulsars with a different mechanism powering the source. The first class is accretion-powered pulsars, also called X-ray pulsars, are a bright and populous source class at X-ray energies. In these sources, the emission energy comes from the accretion of matter from a donor star. See Caballero & Wilms (2012) for a review. The second class is magnetars which have a very strong magnetic field and a relatively slow rotational period. In magnetars, the strong magnetic field powers the emission. See Rea & Esposito (2011) for a review.

3.2 Pulsar Evolution

The simplest model of a pulsar is that it is a rotating dipole magnet with the rotation axis and the magnetic axis offset by an angle θ . A diagram of this model is shown in Figure 3.1. The energy output from the pulsar is then assumed to come from

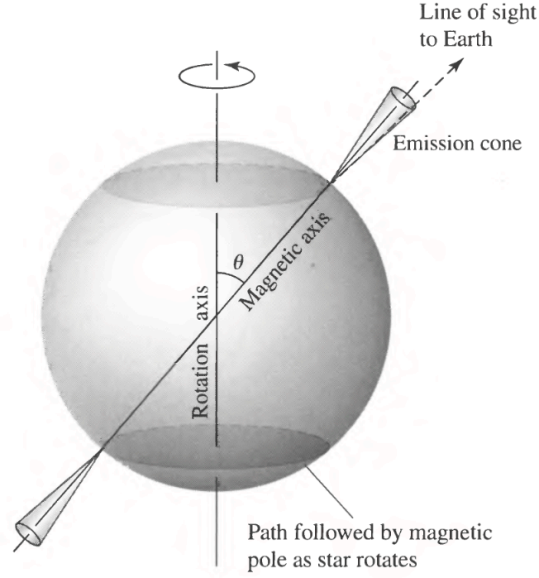


Figure 3.1 The rotating dipole model of a pulsar. This figure is taken from (Carroll & Ostlie 2006).

rotational kinetic energy stored in the neutron star which is released as the pulsar spins down.

Both the period P and the period derivative $\dot{P} = dP/dt$ can be directly observed for a pulsar. Except in a few millisecond pulsars (MSPs) which are being sped up through accretion (see for example Falanga et al. (2005)), pulsars are slowing down ($\dot{P} < 0$).

We write the rotational kinetic energy as

$$E_{\text{rot}} = \frac{1}{2} I \Omega^2 \quad (3.4)$$

where $\Omega = 2\pi/P$ is the angular frequency of the pulsar and I is the moment of inertia.

For a uniform sphere,

$$I = \frac{2}{5} M R^2 \quad (3.5)$$

Assuming a canonical pulsar as was described in Chapter 3, we find a canonical moment of inertia of $I = 10^{45} \text{ g cm}^2$.

We make the connection between the pulsar's spin-down energy and the rotational

kinetic energy as $\dot{E} = -dE_{\text{rot}}/dt$. Using this, Equation 3.4 can be rewritten as

$$\dot{E} = I\Omega\dot{\omega} \quad (3.6)$$

It is believed that as the pulsar spins down, the this rotational energy is released as pulsed electromagnetic radiation and also as a wind of electrons and positrons accelerated in the magnetic field of the pulsar.

If the pulsar were a pure dipole magnet, its radiation would be described as (Gunn & Ostriker 1969)

$$\dot{E} = \frac{2B^2 R_{\text{NS}}^6 \Omega^4 \sin^2 \theta}{3c^3}. \quad (3.7)$$

Combining equations Equation 3.6 and Equation 3.7, we find that for a pure dipole magnet,

$$\dot{\omega} \propto \Omega^3. \quad (3.8)$$

In the few situations in which this relationship has been definitively measured, this relationship does has not hold. We generalize Equation 3.8 as:

$$\dot{\omega} \propto \Omega^n \quad (3.9)$$

where n is what we call the pulsar breaking index. And we note that Equation 3.9 we can can solve for n by taking the derivative of the equation

$$n = \frac{\Omega\ddot{\omega}}{\dot{\omega}^2} \quad (3.10)$$

The breaking index is hard to measure due to timing noise and glitches in the pulsar's phase. To this date, it has been meausred in eight pulsars (See Espinoza et al. 2011, and references therein), and in all situations $n < 3$. This suggests that there are additional processes besides magnetic dipole radiation that contribute to the energy release (Blandford & Romani 1988).

Equation 3.9 is a Bernoulli differential equation which can be integrated to solve

for time:

$$T = \frac{P}{(n-1)|\dot{P}|} \left(1 - \left(\frac{P_0}{P} \right)^{(n-1)} \right) \quad (3.11)$$

For a canonical $n = 3$ pulsars which is relatively old $P_0 \ll P$, we obtain what is called the characteristic age of the pulsar:

$$\tau_c = P/2\dot{P}. \quad (3.12)$$

Using Equation 3.6 and Equation 3.8, we can solve for the spin-down evolution of the pulsar as a function of time (Pacini & Salvati 1973)

$$\dot{E}(t) = \dot{E}_0 \left(1 + \frac{t}{\tau_0} \right)^{-\frac{(n+1)}{(n-1)}} \quad (3.13)$$

where

$$\tau_0 \equiv \frac{P_0}{(n-1)|\dot{P}_0|}. \quad (3.14)$$

Equation 3.9, Equation 3.11, and Equation 3.13 show us that given the current P , \dot{P} , \dot{E} , P_0 , and breaking index n , we can calculate the pulsar's age and energy-emission history.

In a few situations, the pulsar's age is well known and the breaking index can be measured, so P_0 can be inferred. See Kaspi & Helfand (2002) for a review of the topic. For other sources, attempts have been made to infer the initial spin-down age based on the dynamics of an associated supernova remnant (SNR)/PWN (van der Swaluw & Wu 2001).

Finally, if we assume dipole radiation is the only source of energy release, we can combine Equation 3.6 and Equation 3.7 to solve for the magnetic field:

$$B = \sqrt{\frac{3Ic^3}{8\pi^2 R_{\text{NS}}^6 \sin^2 \theta}} P \dot{P} = 3.2 \times 10^{19} \sqrt{P \dot{P}} \text{ G} \quad (3.15)$$

where in the last step we assumed the canonical values of $I = 10^{45} \text{ g cm}^{-2}$, $R_{\text{NS}} = 10 \text{ km}$, $\theta = 90^\circ$, and we assume that P is measured in units of seconds. For example,

for the Crab nebula, $P \approx 33$ ms (Staelin & Reifenstein 1968) and $\dot{P} \approx 36$ ns per day (Richards & Comella 1969) so $B \approx 10^{12}$ G.

3.3 Pulsar Magnetosphere

The basic picture of a pulsar magnetosphere was first presented in Goldreich & Julian (1969). The magnetic dipole of the rotating NS creates a quadrupole electric field.

The potential generated by this field is given as (Goldreich & Julian 1969):

$$\Delta\Phi = \frac{B\Omega^2 R_{\text{NS}}^2}{2c^2} \approx 6 \times 10^{12} \left(\frac{B}{10^{12} \text{ G}} \right) \left(\frac{R_{\text{NS}}}{10 \text{ km}} \right)^3 \left(\frac{P}{1 \text{ s}} \right). \quad (3.16)$$

For NSs, this potential produces magnetic field is much larger than the gravitaional force. Threfore, NS magnetospheres can act as a powerful particle accelerators.

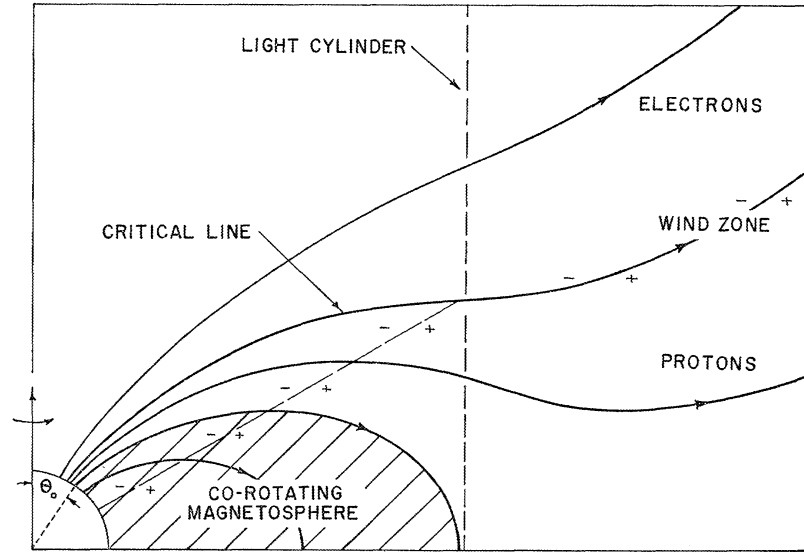


Figure 3.2 The magnetosphere for a rotating pulsar. The pulsar is on the bottom left of the plot. This figure is from Goldreich & Julian (1969).

Figure 3.2 shows a schematic diagram of this magnetosphere.

- Where are sites of acceleratoin

- Charge density in magnetosphere?
- Radio emission
- gamma-ray emission. Slot-gap, outer gap models "A long standing question in pulsar astronomy has been the location of the radio emission. Three places have been suggested; near the light cylinder (Smith 1969), perhaps located in regions of closed magnetic field lines (Gold 1968), and the open field line regions (Radhakrishnan & Cooke 1969). Nowadays, it is widely accepted (see e.g. Lyne & Smith 1990) that the radio emission originates from the open field line region well inside the light cylinder, whereas the very high energy emission (optical and above) probably arises in a quite different mechanism, much nearer to the light cylinder." – kramer_1997a_origin-pulsar

Pulsars typically release only a small percent of their overall energy budget as pulsed emission. The efficiency of converting spin-down energy into pulsed γ -rays is typically $\sim 0.1\%$ to 10% (Abdo et al. (2010d)). For example, the Crab nebulae is estimated to release 0.1% of its spin-down energy as pulsed γ -rays Abdo et al. (2010e). Typically, the energy released as radio and optical photons is much less. The optical flux of the Crab is a factor of ~ 100 smaller Cocke et al. (1969) and the radio flux is a factor of $\sim 10^4$ smaller. Therefore, the vast majority of the energy output of the pulsar is carried away as a pulsar wind, which will be described in the next section.

3.4 Pulsar Wind Nebulae Structure

The basic picture of the physics of PWNs comes from Rees & Gunn (1974) and Kennel & Coroniti (1984). More and more sophisticated models have emerged over the years. See, for example, Gelfand et al. (2009) and references therein.

The wind ejected from the pulsar's magnetosphere is initially cold which means that it flows radially out from the pulsar. This unshocked pulsar wind only emits radiation through IC Bogovalov & Aharonian (2000). This pulsar wind forms a bubble

as it presses into the SNR and forms a shock where the particle wind is further accelerated.

As the wind leaves the magnetosphere, it is believed to be dominated by the energy carried off in electromagnetic fields (the pointing flux $F_{E \times B}$). The rest of the energy is released as a particle flux (F_{particle}). We define the magnetization of the pulsar wind as

$$\sigma = \frac{F_{E \times B}}{F_{\text{particle}}} \quad (3.17)$$

”Between the pulsar light cylinder and the position of the wind termination shock the nature of the wind must thus change dramatically, although the mechanism for this transition is as yet unclear (see Arons 2002, Melatos 1998).”

The radius of the bubble (r_{ts}) is the radius where the ram pressure from the wind equals the pressure of the gas in the SNR. The ram pressure is computed as the energy in the bubble $\dot{E}r_{\text{ts}}/c$ (assuming the particles travel with a velocity $\approx c$) divided by the volume $4\pi r_{\text{ts}}^3/3$:

$$r_{\text{ts}} = \sqrt{\frac{\dot{E}}{\frac{4}{3}\pi P_{\text{ISM}}c}}. \quad (3.18)$$

Here, P_{ISM} is the pressure in the SNR. Typical values for the termination shock are 0.1 pc which is an angular size \sim second of arc (arcsec) for distances \sim kpc (Gaensler & Slane 2006).

At the termination shock, the particles are thermalized (given a random pitch angle), and accelerated to energies of 10^{15} eV (Arons 1996).

Downstream of the shock, the particles emit synchrotron and IC radiation as the thermalized electron population interacts with the magnetic field and seed photons (Gaensler & Slane 2006).

Figure 3.3 shows a diagram describing magnetosphere, unshocked wind, and synchrotron nebula which make up the Pulsar/PWN system.

- “Following this discovery, a theoretical understanding was soon developed in which the central pulsar generates a magnetized particle wind, whose ultrarelativistic electrons and positrons radiate synchrotron emission across the electromagnetic spectrum (Pacini & Salvati 1973, Rees & Gunn 1974). The pulsar has

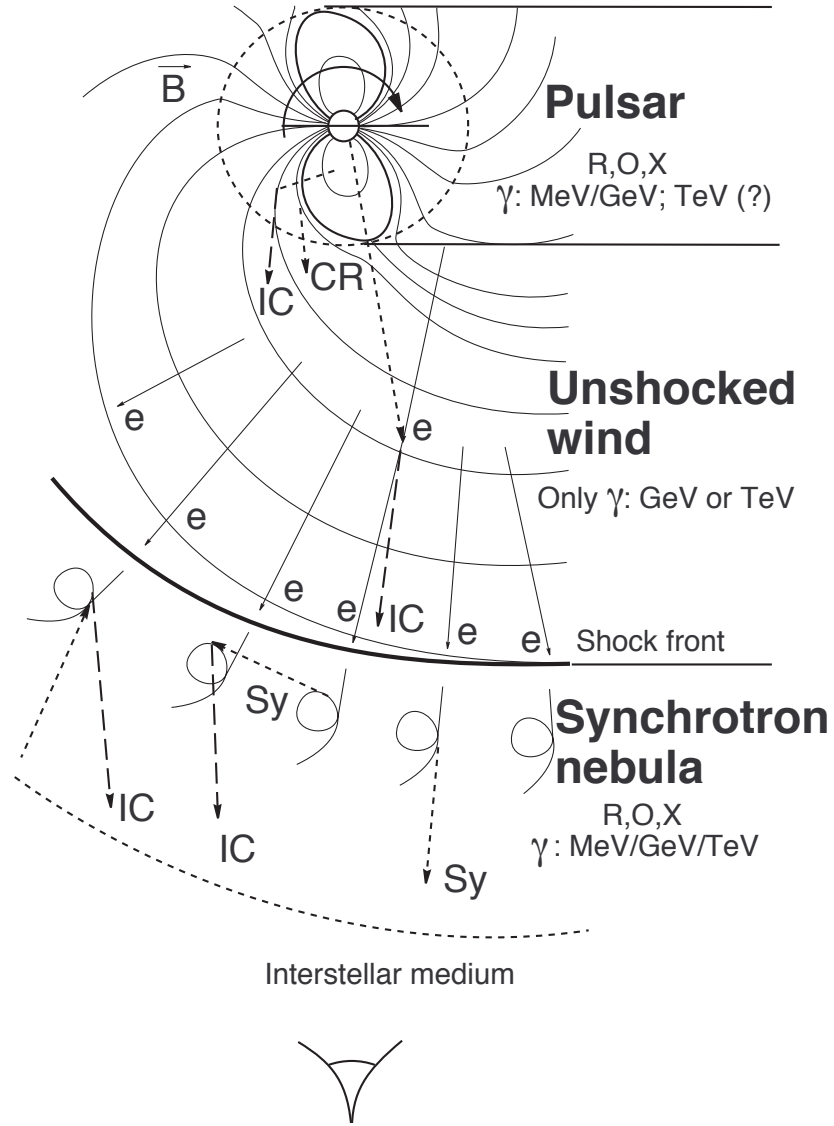


Figure 3.3 The regions of emission in a pulsar/PWN system. This figure shows (top) the pulsar’s magnetosphere, (middle), the unshocked pulsar wind and (bottom) the shocked pulsar wind which can be observed as the PWN. “R”, “O”, “X”, and “ γ ” describe sites of radio, optical, X-ray, and γ -ray emission respectively. “CR”, “Sy”, and “IC” refer to regions of curvature, inverse Compton, and synchrotron emission. Figure is taken from Aharonian & Bogovalov (2003).

steadily released about a third of its total reservoir of 10^{51} ergs of rotational energy into its surrounding nebula over the last 950 years. This is in sharp contrast to shell-like SNRs, in which the dominant energy source is the 10^{51} ergs of kinetic energy released at the moment of the original SN explosion.” – Gaensler & Slane (2006)

- How is pulsar outflow accelerated at shock?
- Discuss magnetization stuff :

1. see page 76 in "Relativistic Astrophysics and Cosmology" by Shapiro

Discuss pulsar evolution "The Evolution and Structure of Pulsar Wind Nebulae" – Bryan M. Gaensler and Patrick O. Slane

Describe Mattana's work on PWNs: "On the evolution of the Gamma- and X-ray luminosities of Pulsar Wind Nebulae"

"As has been discussed, pulsar wind nebulae are prominent sources of very high energy γ -rays. At these wavelengths, emission is caused by inverse Compton acceleration of seed photons by the relativistic electrons present in the nebula (see Section 1.3.5). As the electron energies needed to boost photons to these energies are not as large as that required for synchrotron emission to occur, inverse Compton emission is seen at the extremes of the nebula where synchrotron emission can no longer be observed and as such older pulsar wind nebulae are observed to be much larger in VHE γ -rays than their X-ray counterparts. In addition to this, inverse Compton emission is seen in the unshocked wind area of the PWN as the electrons present are energetic enough to produce inverse Compton radiation even if they are unable to produce synchrotron radiation" – keogh.2010.search-pulsar

"The morphology of a young PWN is often elongated along the pulsar spin axis due to the higher equatorial pressure associated with the toroidal magnetic field (Begelman & Li 1992, van der Swaluw 2003). This effect is seen clearly in many PWNe (e.g., Figs. 1 & 5) and allows one to infer the likely projected orientation of the pulsar. As the nebula expands (see 3.1), Rayleigh-Taylor instabilities form as the fast-moving relativistic fluid encounters and accelerates slower-moving unshocked

supernova ejecta. These form dense, finger-like filamentary structures that suffer photoionization from the surrounding synchrotron emission and radiate recombination lines in the optical and ultraviolet (UV) bands (Fig. 1(b); Hester et al. 1996). The increased density compresses the magnetic field around the filaments, causing enhanced synchrotron emission. One thus observes radio structures that correspond to the optical/UV filaments.” – <http://arxiv.org/pdf/astro-ph/0601081v1.pdf>

Describe SNR Reverse Shock

”In later stages the PWN interacts with the reverse shock formed in the SNR in which the NS was born. This interaction causes the disruption of the PWN, often leading to composite SNRs with complicated PWN structures in their interiors.” – slane_2005_young-neutron

”The structure of a PWN can be altered significantly through interaction with the reverse shock from the SNR in which it resides. In its early evolution the PWN is basically freely-expanding, encountering only small amounts of slow-moving ejecta in the SNR interior. As the SNR blast wave sweeps up sufficient amounts of circumstellar/interstellar material, a reverse shock is driven back through the ejecta. As this reverse shock propagates, heating the ejecta, it will eventually reach the PWN.” – slane_2005_young-neutron

3.5 Pulsar Wind Nebula Emission

In the Pulsar/PWN model, a population of electrons is emitted from the magnetosphere, released as an unshocked wind, and then accelerated at the termination shock. In the surrounding nebula, the electrons emit synchrotron and inverse Compton

- What is the characteristic synchrotron energy
- What is the characteristic IC energy
- look at: etten_2012a_particle-populations

Energetics of PWNe:

“The efficiency of conversion of spin-down luminosity into synchrotron emission is defined by efficiency factors η_{sync} and η_{IC} . Typical values are $\eta_{\text{sync}} \approx 0.1$ and $\eta_{\text{IC}} \approx 0.01$ (Becker & Trumper 1997, Frail & Scharringhausen 1997), although wide excursions from this are observed. Note that if the synchrotron lifetime of emitting particles is a significant fraction of the PWN age (as is almost always the case at radio wavelengths, and sometimes also in X-rays), then the PWN emission represents an integrated history of the pulsar spin down, and R and X are not true instantaneous efficiency factors”
—gaensler_2006_evolution-structure

X-ray energetics tabulated from: <http://arxiv.org/pdf/astro-ph/0006030v1.pdf>

Include discussion of cooling in Matanna et al 2009 (equation 12)

Look up scaling relationships for IC and Sync radiation from Adam Van Etten's thesis

Chapter 4

Maximum-likelihood analysis of LAT data

In this chapter, we discuss maximum-likelihood analysis, the principle analysis method used to perform spectral and spatial analysis of LAT data. In Section 4.1, we discuss the reasons necessary for employing this analysis procedure compared to other simpler analysis methods. In Section 4.2, we describe the benefits of a maximum-likelihood analysis. In Section 4.3, we discuss the steps involved in defining a complete model of the sky, a necessary part of any likelihood analysis.

In Section 4.5, we discuss the standard implementation of binned maximum likelihood in the LAT Science Tools and in particular the tool `gtlike`. In Section 4.6, we then discuss the `pointlike` package, an alternate package for maximum-likelihood analysis of LAT data. We discuss the similarities and differences between `pointlike` and `gtlike`.

In the next chapter (Chapter 5), we will discuss the addition of capability into `pointlike` for studying spatially-extended sources and the analysis method which will be used in this paper to study spatially-extended sources.

We note that much of the notation and formulation of likelihood analysis in this chapter follows Kerr (2010).

4.1 Motivations for Maximum-Likelihood Analysis of Gamma-ray Data

Traditionally, spectral and spatial analysis of astrophysical data relies on a process known as aperture photometry. In this process, a source in the data is analyzed by directly measuring the number of photons coming from the object. This process is done by measuring the counts within a given radius of the source and subtracting from it a background level estimated from a nearby region. Often, the source's flux is calibrated by measurements of nearby objects with known fluxes. Otherwise, the flux can be obtained from by dividing the number of counts from the source by the telescope's size, the observation time, and the telescope's conversion efficiency.

Similarly, for faint sources the statistical significance of the detection can be obtained from the Poisson nature of the data. For TeV experiments such as H.E.S.S., this analysis method is described in Li & Ma (1983).

Unfortunately, this simpler analysis method is inadequate for dealing with the complexities introduced in analyzing LAT data.

Most importantly, aperture photometry assumed that the background is isotropic so that the background level below the source can be estimated from nearby regions. As was discussed in Section 2.6, the Galactic diffuse emission is highly anisotropic, rendering this assumption invalid.

In addition, this method is not optimal due to the high density of sources detected in the Gamma-ray sky. 2FGL reported on the detection of 1873 sources, which corresponds to an average source spacing of $\sim 5^\circ$. But within the inner 45° of the galactic plane in longitude and 0.5° of the galactic plane in latitude, there are 73 sources, corresponding to a source density of ~ 1 source per square degree. The aperture photometry method is unable to effectively fit multiple sources when the tails of the PSF overlap and furthermore make background estimation problematic.

Finally, this method is suboptimal due to the large energy range of LAT observations. A typical spectral analysis studies a source from an energy of 100 MeV to energies above 100 GeV. Similarly, as was shown in , the PSF of the LAT is rather broad ($\gtrsim 1^\circ$) at low energy and much narrower ($\sim 0.1^\circ$) at higher energies. Therefore,

what
section
dis-
cusses
en-
ergy

there is a much higher sensitivity to the higher energy photons coming from a source. But simple aperture photometry method would ignore this improvement by weighting each photon equally.

4.2 Description of Maximum-Likelihood Analysis

The field of γ -ray astrophysics has generally found maximum-likelihood to be a dependable method to avoid the issues discussed above. The term likelihood was first introduced by Fisher (1925). Maximum-likelihood was applied to photon-counting experiments in the context of astrophysics by Cash (1979). Mattox et al. (1996) described the maximum-likelihood analysis framework developed to analyze EGRET data.

In the formulation, one relies upon primarily upon the likelihood function. The likelihood, denoted \mathcal{L} , is quite simply the probability of obtaining the observed data given an assumed model:

$$\mathcal{L} = P(\text{data}|\text{model}) \quad (4.1)$$

Section 4.3 will provide describe the components that go into a model of the data.

Generally, a model of the sky depends upon a list of parameters that we denote as $\boldsymbol{\lambda}$. Therefore, the likelihood function itself becomes a function of the parameters of the model:

$$\mathcal{L} = \mathcal{L}(\boldsymbol{\lambda}) \quad (4.2)$$

The term maximum-likelihood refers to the fact that the best-fit parameters of a model can be estimated by maximizing the likelihood function.

What are the benefits of maximum likelihood

Describe Wilk's Theorem and its application to parameter error estimation

4.3 Defining a Model of the Sources in the Sky

In order to perform a maximum-likelihood analysis, one requires a parameterized model of the sky. A model of the sky is composed of a set of γ -ray sources, each

characterized by its photon flux density $\mathcal{F}(E, t, \vec{\Omega}|\boldsymbol{\lambda})$. This represents the number of photons emitted per unit energy, per unit time, per units solid angle at a given energy, time, and position in the sky. In the Centimetre-Gram-Second System of Units (CGS), it has units of $\text{ph cm}^{-2}\text{s}^{-1}\text{erg}^{-1}\text{sr}^{-1}$.

Often, the spatial and spectral part of the source model are separable and independent of time. When that is the case, we like to write the source model as

$$\mathcal{F}(E, t, \vec{\Omega}|\boldsymbol{\lambda}) = \frac{dN}{dE} \times \text{PDF}(\vec{\Omega}). \quad (4.3)$$

Here, $\frac{dN}{dE}$ is only a function of energy and $\text{PDF}(\vec{\Omega})$ is only a function of position ($\vec{\Omega}$). In this formulation, some of the model parameters $\boldsymbol{\lambda}$ are taken by the $\frac{dN}{dE}$ function and some by the $\text{PDF}(\vec{\Omega})$ function. In CGS, $\frac{dN}{dE}$ is in units of $\text{ph cm}^{-2}\text{s}^{-1}\text{erg}^{-1}$.

The spectrum $\frac{dN}{dE}$ is typically modeled by simple geometric functions. The most popular spectral model is a power law (PL):

$$\frac{dN}{dE} = N_0 \left(\frac{E}{E_0} \right)^{-\gamma} \quad (4.4)$$

Here, $\frac{dN}{dE}$ is a function of energy and also for the two model parameters (the prefactor N_0 and the spectral index γ). The parameter E_0 is often called the energy scale or the pivot energy and is not considered a model parameter.

Another common spectral model is the broken-power law (BPL) spectral model

$$\frac{dN}{dE} = N_0 \times \begin{cases} (E/E_b)^{-\gamma_1} & \text{if } E < E_b \\ (E/E_b)^{-\gamma_2} & \text{if } E \geq E_b \end{cases} \quad (4.5)$$

This model represents a powerlaw with an index of γ_1 which has a break at energy E_b to having an index of γ_2 .

Finally, the exponentially-cutoff power law (ECPL) spectral model is often used to model the γ -ray emission from pulsars:

$$\frac{dN}{dE} = N_0 \left(\frac{E}{E_0} \right)^{-\gamma} \exp \left(-\frac{E}{E_c} \right). \quad (4.6)$$

For energies much below E_c , the ECPL is a PL with spectral index γ . For energies much larger than E_c , the ECPL exponentially decreases.

PDF represents the spatial distribution of the emission. It is traditionally normalized as though it was a probability:

$$\int d\Omega \text{PDF}(\vec{\Omega}). \quad (4.7)$$

Therefore, in CGS PDF has units of sr^{-1} . For a point-like source at a position $\vec{\Omega}'$, the spatial model is:

$$\text{PDF}(\vec{\Omega}) = \delta(\vec{\Omega} - \vec{\Omega}') \quad (4.8)$$

and is a function of the position of the source. Example spatial models for spatially-extended sources will be presented in section XXXXX.

This formulation assumed that the source models are not time dependent. This is traditionally because it is difficult to find simple parameterized models to fit the time behavior of a variable source. Instead, the typical strategy to fit variable sources is to divide a large range of time into multiple smaller time intervals and to perform multiple likelihood fits in each time range.

In some situations, the spatial and spectral part of a source do not nicely decouple. An example of this could be SNRs which could show a spectral variation across the source. Katsuta et al. (2012) and Hewitt et al. (2012) have simplified this problem by a simple method which has been adopted to study this kind of source.

FINISH DISCUSSION

In situations where spatial and spectral components couple, typical to make multiple spatial templates, each with an independent spectra (e.g. the Puppis A paper's fitting multiple hemispheres).

Discuss how diffuse background is more complicated and requires a mapcube.

WHAT
SEC-
TION
DE-
SCRIBES
EX-
TENDED
SOURCE
PDFs

4.4 The LAT Instrument Response Functions

The performance of the LAT is composed of two effects. The efficiency of the LAT refers to its ability to reconstruct a photon which comes into the detector. The dispersion of the LAT refers to the probability of misreconstructing an event.

The efficiency is typically called the effective area. We write it as $\epsilon(E, t, \vec{\Omega})$. It is a function of energy, time, and solid angle (SA). It is measured in units of area (cm^2).

LINK TO [arXiv:1206.1896](https://arxiv.org/abs/1206.1896) for MORE THOROUGH DISCUSSION OF EFFECTIVE AREA

DISCUSS HOW EFFECTIVE AREA IS A FUNCTION OF DIFFERENT THINGS

The dispersion is the probability of a photon with true energy E and incoming direction $\vec{\Omega}$ at time t being reconstructed to have an energy E' , an incoming direction $\vec{\Omega}'$ at a time t' . The dispersion is written as $P(E', t', \vec{\Omega}' | E, t, \vec{\Omega})$. It represents a probability and is therefore normalized such that

$$\int \int \int dE d\Omega dt P(E', t', \vec{\Omega}' | E, t, \vec{\Omega}) = 1 \quad (4.9)$$

What is the range of the integrals

Therefore, $P(E', t', \vec{\Omega}' | E, t, \vec{\Omega})$ has units of $1/\text{energy}/\text{SA}/\text{time}$

We assume these two factors to decouple and write the LAT's instrument response as

$$R(E', \vec{\Omega}', t' | E, \vec{\Omega}, t) = \epsilon(E, t, \vec{\Omega}) P(E', t', \vec{\Omega}' | E, t, \vec{\Omega}) \quad (4.10)$$

Therefore, the instrument response has units of $\text{area}/\text{energy}/\text{SA}/\text{time}$

The convolution of the flux of a model with the instrument response produces the expected counts per unit energy/time/SA begin reconstructed to have an energy E' at a position $\vec{\Omega}'$ and at a time t' :

$$\tau(E', \vec{\Omega}', t' | \lambda) = \int \int \int dE d\Omega dt \mathcal{F}(E, t, \vec{\Omega} | \lambda) R(E', \vec{\Omega}', t' | E, \vec{\Omega}, t) \quad (4.11)$$

Here, this integral is performed over all true energies, SAs, and times for which the source model has support.

For LAT analysis, we conventionally make the simplifying assumption that the energy, spatial, and time dispersion decouple:

$$P(E', t', \vec{\Omega}' | E, t, \vec{\Omega}) = \text{PSF}(\vec{\Omega}' | E, \vec{\Omega}) \times E_{\text{disp}}(E' | E) \times T_{\text{disp}}(t' | t) \quad (4.12)$$

Here, PSF is the point-spread function and represents ...

BETTER DISCUSSION OF PSF OF THE LAT, WHAT ITS SCALE IS...

E_{disp} represents the energy dispersion of the LAT. The energy dispersion of the LAT is a function of both the incident energy and incident angle of the photon. It varies from $\sim 5\%$ to 20% , degrading at lower energies due to energy losses in the tracker and at higher energy due to electromagnetic shower losses outside the calorimeter. Similarly, it improves for photons with higher incident angles that are allowed a longer path through the calorimeter (Ackermann et al. 2012).

For sources with smoothly-varying spectra, the effects of ignoring the inherent energy dispersion of the LAT are typically small. Ackermann et al. (2012) performed a monte carlo simulation to show that for power-law point-like sources, the bias introduced by ignoring energy dispersion was on the level of a few percent. Therefore, energy dispersion is typically ignored for standard likelihood analysis:

$$E_{\text{disp}} = \delta(E - E') \quad (4.13)$$

We caution that for analysis of sources extended to energies below 100 MeV and for sources expected to have spectra that do not smoothly vary, the effects of energy dispersion could be more severe.

- T_{disp} is the time dispersion.
- _____
- The timing dispersion is $< 10 \mu\text{s}$ Atwood et al. (2009)
- WRITE ENERGY DISPERSION AS A DELTA FUNCTION

Why
dis-
card
time
dis-
per-
sion

Therefore, the instrument response is typically approximated as

FINISH

$$R(E', \vec{\Omega}', t' | E, \vec{\Omega},) = \epsilon(E, t', \vec{\Omega}) \text{PSF}(\vec{\Omega}' | E, \vec{\Omega}) \quad (4.14)$$

The expected count rate is then typically integrated over time to compute the total counts. Assuming that the source model is time independent, we get:

$$\tau(E', \vec{\Omega}' | \boldsymbol{\lambda}) = \int d\Omega \mathcal{F}(E, \vec{\Omega} | \boldsymbol{\lambda}) \left(\int dt \epsilon(E, t, \vec{\Omega}) \right) \text{PSF}(\vec{\Omega}' | E, \vec{\Omega}) \quad (4.15)$$

This equation essentially says that the counts expected by the LAT for the particular model is the product of the source's flux with the effective area and then convolved with the point-spread function.

Figure out how the θ dependence of the IRFs factors into this calculation

4.5 Binned Maximum-Likelihood of LAT Data with the Science Tools

- For a standard LAT analysis, we perform a binned maximum-likelihood analysis:
- In the standard science tools, the data is binned in position and energy. and integrated in energy.
- For time-series analysis, typically a time-summed analysis is performed successivly in multiple time bins.
- The likelihood comes from a sum over each bin
- The likelihood is defined as

$$\mathcal{L} = \prod_j \frac{\theta_j^{n_j} e^{-\theta_j}}{n_j!} \quad (4.16)$$

– Here, j is a sum over position/energy bins.

- θ_j is the counts predicted by the model, which is defined following the discussion in Section 4.3.
- n_j are the observed counts in the spatial/energy bin j
- The model counts are computed by integrating the differential counts defined in Equation 4.11 over the energy bin:

$$\theta_{ij} = \int_j dE d\Omega dt \tau(E, \vec{\Omega}, t | \boldsymbol{\lambda}_i) \quad (4.17)$$

Here, j represents the integral over the j th position/energy bin, i represents the i th source, and $\boldsymbol{\lambda}_i$ refers to the parameters defining the i th source. The total model counts is computed by summing over all sources:

$$\theta_j = \sum_i \theta_{ij} \quad (4.18)$$

- In the standard *Fermi* science tools, the binning of photons over position in the sky and energy to compute n_j is done with `gtbin`.
- In the standard *Fermi* science tools, the model counts θ_j are computed in several steps . . .
- The instrument response is computed with a combination of `gtltcube`, `gtexpcube`.
- Convert a model of the sky into model predicted counts
- poisson likelihood
- Particular implementation of maximum likelihood analysis
- Describe `gtbin`, `gtselect`, `gtlike`

Write Section or Perform simple MC Simulation to demonstrate significance of detection

4.6 The Alternate Maximum-Likelihood Package `pointlike`

- Developed for Speed
- Sparse Matrices,
- Methods for computing integral model counts.

Chapter 5

Analysis of Spatially Extended LAT Sources

This chapter is based the first part of the the paper “Search for Spatially Extended Fermi-LAT Sources Using Two Years of Data” by Lande et al. 2012 ApJ, 756, 5

Spatial extension is an important characteristic for correctly associating γ -ray-emitting sources with their counterparts at other wavelengths and for obtaining an unbiased model of their spectra. We present a new method for quantifying the spatial extension of sources detected by the Large Area Telescope (LAT), the primary science instrument on the *Fermi Gamma-ray Space Telescope (Fermi)*. We perform a series of Monte Carlo simulations to validate this tool and calculate the LAT threshold for detecting the spatial extension of sources.

5.1 Introduction

A number of astrophysical source classes including supernova remnants (SNRs), pulsar wind nebulae (PWNe), molecular clouds, normal galaxies, and galaxy clusters are expected to be spatially resolvable by the Large Area Telescope (LAT), the primary instrument on the *Fermi Gamma-ray Space Telescope (Fermi)*. Additionally, dark

matter satellites are also hypothesized to be spatially extended. See Atwood et al. (2009) for pre-launch predictions. The LAT has detected seven SNRs which are significantly extended at GeV energies: W51C, W30, IC 443, W28, W44, RX J1713.7–3946, and the Cygnus Loop (Abdo et al. 2009a; Ajello et al. 2012; Abdo et al. 2010b,f,a, 2011; Katagiri et al. 2011). In addition, three extended PWN have been detected by the LAT: MSH 15–52, Vela X, and HESS J1825–137 (Abdo et al. 2010a; Abdo et al. 2010; Grondin et al. 2011). Two nearby galaxies, the Large and Small Magellanic Clouds, and the lobes of one radio galaxy, Centaurus A, were spatially resolved at GeV energies (Abdo et al. 2010c,b,c). A number of additional sources detected at GeV energies are positionally coincident with sources that exhibit large enough extension at other wavelengths to be spatially resolvable by the LAT at GeV energies. In particular, there are 59 GeV sources in the second Fermi Source Catalog (2FGL) that might be associated with extended SNRs (2FGL, Nolan et al. 2012). Previous analyses of extended LAT sources were performed as dedicated studies of individual sources so we expect that a systematic scan of all LAT-detected sources could uncover additional spatially extended sources.

The current generation of air Cherenkov detectors have made it apparent that many sources can be spatially resolved at even higher energies. Most prominent was a survey of the Galactic plane using the High Energy Stereoscopic System (H.E.S.S.) which reported 14 spatially extended sources with extensions varying from $\sim 0^\circ.1$ to $\sim 0^\circ.25$ (Aharonian et al. 2006d). Within our Galaxy very few sources detected at TeV energies, most notably the γ -ray binaries LS 5039 (Aharonian et al. 2006a), LS I+61–303 (Albert et al. 2006; Acciari et al. 2011), HESS J0632+057 (Aharonian et al. 2007c), and the Crab nebula (Weekes et al. 1989), have no detectable extension. High-energy γ -rays from TeV sources are produced by the decay of π^0 s produced by hadronic interactions with interstellar matter and by relativistic electrons due to Inverse Compton (IC) scattering and bremsstrahlung radiation. It is plausible that the GeV and TeV emission from these sources originates from the same population of high-energy particles and so at least some of these sources should be detectable at GeV energies. Studying these TeV sources at GeV energies would help to determine the emission mechanisms producing these high energy photons.

The LAT is a pair conversion telescope that has been surveying the γ -ray sky since 2008 August. The LAT has broad energy coverage (20 MeV to > 300 GeV), wide field of view (~ 2.4 sr), and large effective area (~ 8000 cm² at > 1 GeV). Additional information about the performance of the LAT can be found in Atwood et al. (2009).

Using 2 years of all-sky survey data, the LAT Collaboration published 2FGL (2FGL, Nolan et al. 2012). The possible counterparts of many of these sources can be spatially resolved when observed at other frequencies. But detecting the spatial extension of these sources at GeV energies is difficult because the size of the point-spread function (PSF) of the LAT is comparable to the typical size of many of these sources.

The capability to spatially resolve GeV γ -ray sources is important for several reasons. Finding a coherent source extension across different energy bands can help to associate a LAT source to an otherwise confused counterpart. Furthermore, γ -ray emission from dark matter annihilation has been predicted to be detectable by the LAT. Some of the dark matter substructure in our Galaxy could be spatially resolvable by the LAT (Baltz et al. 2008). Characterization of spatial extension could help to identify this substructure. Also, due to the strong energy dependence of the LAT PSF, the spatial and spectral characterization of a source cannot be decoupled. An inaccurate spatial model will bias the spectral model of the source and vice versa. Specifically, modeling a spatially extended source as point-like will systematically soften measured spectra. Furthermore, correctly modeling source extension is important for understanding an entire region of the sky. For example, an imperfect model of the spatially extended LMC introduced significant residuals in the surrounding region (Abdo et al. 2010d; Nolan et al. 2012). Such residuals can bias the significance and measured spectra of neighboring sources in the densely populated Galactic plane.

For these reasons, in Section 5.2 we present a new systematic method for analyzing spatially extended LAT sources. In Section 5.3, we demonstrate that this method can be used to test the statistical significance of the extension of a LAT source and we assess the expected level of bias introduced by assuming an incorrect spatial model. In Section ??, we calculate the LAT detection threshold to resolve the extension of a source. In Section 5.5, we study the ability of the LAT to distinguish between a single

extended source and unresolved closely-spaced point-like sources. In Section 5.6, we further demonstrate that our detection method does not misidentify point-like sources as being extended by testing the extension of active Galactic nuclei (AGN) believed to be unresolvable. In Section ??, we systematically reanalyze the twelve extended sources included in the 2FGL catalog and in Section ?? we describe a way to estimate systematic errors on the measured extension of a source. In Section ??, we describe a search for new spatially extended LAT sources. Finally, in Section ?? we present the detection of the extension of nine spatially extended sources that were reported in the 2FGL catalog but treated as point-like in the analysis. Two of these sources have been previously analyzed in dedicated publications.

5.2 Analysis Method

Morphological studies of sources using the LAT are challenging because of the strongly energy-dependent PSF that is comparable in size to the extension of many sources expected to be detected at GeV energies. Additional complications arise for sources along the Galactic plane due to systematic uncertainties in the model for Galactic diffuse emission.

For energies below ~ 300 MeV, the angular resolution is limited by multiple scattering in the silicon strip tracking section of the detector and is several degrees at 100 MeV. The PSF improves with energy approaching a 68% containment radius of $\sim 0.2^\circ$ at the highest energies (when averaged over the acceptance of the LAT) and is limited by the ratio of the strip pitch to the height of the tracker (Atwood et al. 2009; Abdo et al. 2009b; Ackermann et al. 2012).¹ However, since most high energy astrophysical sources have spectra that decrease rapidly with increasing energy, there are typically fewer higher energy photons with improved angular resolution. Therefore sophisticated analysis techniques are required to maximize the sensitivity of the LAT to extended sources.

¹More information about the performance of the LAT can be found at the *Fermi* Science Support Center (FSSC, <http://fermi.gsfc.nasa.gov>).

5.2.1 Modeling Extended Sources in the `pointlike` Package

A new maximum-likelihood analysis tool has been developed to address the unique requirements for studying spatially extended sources with the LAT. It works by maximizing the Poisson likelihood to detect the observed distributions of γ -rays (referred to as counts) given a parametrized spatial and spectral model of the sky. The data are binned spatially, using a HEALPix pixellization, and spectrally (Górski et al. 2005) and the likelihood is maximized over all bins in a region. The extension of a source can be modeled by a geometric shape (e.g. a disk or a two-dimensional Gaussian) and the position, extension, and spectrum of the source can be simultaneously fit.

This type of analysis is unwieldy using the standard LAT likelihood analysis tool `gtlike`² because it can only fit the spectral parameters of the model unless a more sophisticated iterative procedure is used. We note that `gtlike` has been used in the past in several studies of source extension in the LAT Collaboration (Abdo et al. 2010c,b,f, 2009a). In these studies, a set of `gtlike` maximum likelihood fits at fixed extensions was used to build a profile of the likelihood as a function of extension. The `gtlike` likelihood profile approach has been shown to correctly reproduce the extension of simulated extended sources assuming that the true position is known (Giordano & Fermi LAT Collaboration 2011). But it is not optimal because the position, extension, and spectrum of the source must be simultaneously fit to find the best fit parameters and to maximize the statistical significance of the detection. Furthermore, because the `gtlike` approach is computationally intensive, no large-scale Monte Carlo simulations have been run to calculate its false detection rate.

The approach presented here is based on a second maximum likelihood fitting package developed in the LAT Collaboration called `pointlike` (Abdo et al. 2010d; Kerr 2010). The choice to base the spatial extension fitting on `pointlike` rather than `gtlike` was made due to considerations of computing time. The `pointlike` algorithm was optimized for speed to handle larger numbers of sources efficiently, which is important for our catalog scan and for being able to perform large-scale Monte Carlo simulations to validate the analysis. Details on the `pointlike` package

²`gtlike` is distributed publicly by the FSSC.

can be found in Kerr (2010). We extended the code to allow a simultaneous fit of the source extension together with the position and the spectral parameters.

5.2.2 Extension Fitting

In `pointlike`, one can fit the position and extension of a source under the assumption that the source model can be factorized: $M(x, y, E) = S(x, y) \times X(E)$, where $S(x, y)$ is the spatial distribution and $X(E)$ is the spectral distribution. To fit an extended source, `pointlike` convolves the extended source shape with the PSF (as a function of energy) and uses the `minuit` library (James & Roos 1975) to maximize the likelihood by simultaneously varying the position, extension, and spectrum of the source. As will be described in Section ??, simultaneously fitting the position, extension, and spectrum is important to maximize the statistical significance of the detection of the extension of a source. To avoid projection effects, the longitude and latitude of the source are not directly fit but instead the displacement of the source in a reference frame centered on the source.

The significance of the extension of a source can be calculated from the likelihood-ratio test. The likelihood ratio defines the test statistic (TS) by comparing the likelihood of a simpler hypothesis to a more complicated one:

$$\text{TS} = 2 \log(\mathcal{L}(H_1)/\mathcal{L}(H_0)), \quad (5.1)$$

where H_1 is the more complicated hypothesis and H_0 the simpler one. For the case of the extension test, we compare the likelihood when assuming the source has either a point-like or spatially extended spatial model:

$$\text{TS}_{\text{ext}} = 2 \log(\mathcal{L}_{\text{ext}}/\mathcal{L}_{\text{ps}}). \quad (5.2)$$

`pointlike` calculates TS_{ext} by fitting a source first with a spatially extended model and then as a point-like source. The interpretation of TS_{ext} in terms of a statistical significance is discussed in Section ??.

For extended sources with an assumed radially-symmetric shape, we optimized

the calculation by performing one of the integrals analytically. The expected photon distribution can be written as

$$\text{PDF}(\vec{r}) = \int \text{PSF}(|\vec{r} - \vec{r}'|) I_{\text{src}}(\vec{r}') r' dr' d\phi' \quad (5.3)$$

where \vec{r} represents the position in the sky and $I_{\text{src}}(\vec{r})$ is the spatial distribution of the source. The PSF of the LAT is currently parameterized in the Pass 7-V6 (P7-V6) Source Instrument Response Function (IRFs, Ackermann et al. 2012) by a King function (King 1962):

$$\text{PSF}(r) = \frac{1}{2\pi\sigma^2} \left(1 - \frac{1}{\gamma}\right) \left(1 + \frac{u}{\gamma}\right)^{-\gamma}, \quad (5.4)$$

where $u = (r/\sigma)^2/2$ and σ and γ are free parameters (Kerr 2010). For radially-symmetric extended sources, the angular part of the integral can be evaluated analytically

$$\begin{aligned} \text{PDF}(u) &= \int_0^\infty r' dr' I_{\text{src}}(v) \int_0^{2\pi} d\phi' \text{PSF}(\sqrt{2\sigma^2(u + v - 2\sqrt{uv} \cos(\phi - \phi'))}) \\ &= \int_0^\infty dv I_{\text{src}}(v) \left(\frac{\gamma-1}{\gamma}\right) \left(\frac{\gamma}{\gamma + u + v}\right)^\gamma \times {}_2F_1\left(\gamma/2, \frac{1+\gamma}{2}, 1, \frac{4uv}{(\gamma + u + v)^2}\right), \end{aligned} \quad (5.5)$$

$$(5.6)$$

where $v = (r'/\sigma)^2/2$ and ${}_2F_1$ is the Gaussian hypergeometric function. This convolution formula reduces the expected photon distribution to a single numerical integral.

There will always be a small numerical discrepancy between the expected photon distribution derived from a true point-like source and a very small extended source due to numerical error in the convolution. In most situations, this error is insignificant. But in particular for very bright sources, this numerical error has the potential to bias the TS for the extension test. Therefore, when calculating TS_{ext} , we compare the likelihood fitting the source with an extended spatial model to the likelihood when the extension is fixed to a very small value (10^{-10} degrees in radius for a uniform disk model).

We estimate the error on the extension of a source by fixing the position of the source and varying the extension until the log of the likelihood has decreased by 1/2,

corresponding to a 1σ error (Eadie et al. 1971). Figure 5.1 demonstrates this method by showing the change in the log of the likelihood when varying the modeled extension of the SNR IC 443. The localization error is calculated by fixing the extension and spectrum of the source to their best fit values and then fitting the log of the likelihood to a 2D Gaussian as a function of position. This localization error algorithm is further described in Nolan et al. (2012).

5.2.3 gtlike Analysis Validation

`pointlike` is important for analyses of LAT data that require many iterations such as source localization and extension fitting. On the other hand, because `gtlike` makes fewer approximations in calculating the likelihood we expect the spectral parameters found with `gtlike` to be slightly more accurate. Furthermore, because `gtlike` is the standard likelihood analysis package for LAT data, it has been more extensively validated for spectral analysis. For those reasons, in the following analysis we used `pointlike` to determine the position and extension of a source and subsequently derived the spectrum using `gtlike`. Both `gtlike` and `pointlike` can be used to estimate the statistical significance of the extension of a source and we required that both methods agree for a source to be considered extended. There was good agreement between the two methods. Unless explicitly mentioned, all TS, TS_{ext} , and spectral parameters were calculated using `gtlike` with the best-fit positions and extension found by `pointlike`.

5.2.4 Comparing Source Sizes

We considered two models for the surface brightness profile for extended sources: a 2D Gaussian model

$$I_{\text{Gaussian}}(x, y) = \frac{1}{2\pi\sigma^2} \exp(-(x^2 + y^2)/2\sigma^2) \quad (5.7)$$

or a uniform disk model

$$I_{\text{disk}}(x, y) = \begin{cases} \frac{1}{\pi\sigma^2} & x^2 + y^2 \leq \sigma^2 \\ 0 & x^2 + y^2 > \sigma^2. \end{cases} \quad (5.8)$$

Although these shapes are significantly different, Figure 5.2 shows that, after convolution with the LAT PSF, their PDFs are similar for a source that has a 0.5° radius typical of LAT-detected extended sources. To allow a valid comparison between the Gaussian and the uniform disk models, we define the source size as the radius containing 68% of the intensity (r_{68}). By direct integration, we find

$$r_{68,\text{Gaussian}} = 1.51\sigma, \quad (5.9)$$

$$r_{68,\text{disk}} = 0.82\sigma, \quad (5.10)$$

where σ is defined in Equation 5.7 and Equation 5.8 respectively. For the example above, $r_{68} = 0.5^\circ$ so $\sigma_{\text{disk}} = 0.61^\circ$ and $\sigma_{\text{Gaussian}} = 0.33^\circ$.

For sources that are comparable in size to the PSF, the differences in the PDF for different spatial models are lost in the noise and the LAT is not sensitive to the detailed spatial structure of these sources. In Section ??, we perform a dedicated Monte Carlo simulation that shows there is little bias due to incorrectly modeling the spatial structure of an extended source. Therefore, in our search for extended sources we use only a radially-symmetric uniform disk spatial model. Unless otherwise noted, we quote the radius to the edge (σ) as the size of the source.

5.3 Validation of the TS Distribution

5.3.1 Point-like Source Simulations Over a Uniform Background

We tested the theoretical distribution for TS_{ext} to evaluate the false detection probability for measuring source extension. To do so, we tested simulated point-like sources

for extension. Mattox et al. (1996) discuss that the TS distribution for a likelihood-ratio test on the existence of a source at a given position is

$$P(\text{TS}) = \frac{1}{2}(\chi_1^2(\text{TS}) + \delta(\text{TS})), \quad (5.11)$$

where $P(\text{TS})$ is the probability density to get a particular value of TS, χ_1^2 is the chi-squared distribution with one degree of freedom, and δ is the Dirac delta function. The particular form of Equation 5.11 is due to the null hypothesis (source flux $\Phi = 0$) residing on the edge of parameter space and the model hypothesis adding a single degree of freedom (the source flux). It leads to the often quoted result $\sqrt{TS} = \sigma$, where σ here refers to the significance of the detection. It is plausible to expect a similar distribution for the TS in the test for source extension since the same conditions apply (with the source flux Φ replaced by the source radius r and $r < 0$ being unphysical). To verify Equation 5.11, we evaluated the empirical distribution function of TS_{ext} computed from simulated sources.

We simulated point-like sources with various spectral forms using the LAT on-orbit simulation tool `gtobssim`³ and fit the sources with `pointlike` using both point-like and extended source hypotheses. These point-like sources were simulated with a power-law spectral model with integrated fluxes above 100 MeV ranging from 3×10^{-9} to 1×10^{-5} ph cm⁻²s⁻¹ and spectral indices ranging from 1.5 to 3. These values were picked to represent typical parameters of LAT-detected sources. The point-like sources were simulated on top of an isotropic background with a power-law spectral model with integrated flux above 100 MeV of 1.5×10^{-5} ph cm⁻²s⁻¹ sr⁻¹ and spectral index 2.1. This was taken to be the same as the isotropic spectrum measured by EGRET (Sreekumar et al. 1998). This spectrum is comparable to the high-latitude background intensity seen by the LAT. The Monte Carlo simulation was performed over a one-year observation period using a representative spacecraft orbit and livetime. The reconstruction was performed using the P7_V6 Source class event selection and IRFs (Ackermann et al. 2012). For each significantly detected point-like source ($\text{TS} \geq 25$), we used `pointlike` to fit the source as an extended source and calculate TS_{ext} .

³`gtobssim` is distributed publicly by the FSSC.

This entire procedure was performed twice, once fitting in the 1 GeV to 100 GeV energy range and once fitting in the 10 GeV to 100 GeV energy range.

For each set of spectral parameters, $\sim 20,000$ statistically independent simulations were performed. For lower-flux spectral models, many of the simulations left the source insignificant ($TS < 25$) and were discarded. Table 5.1 shows the different spectral models used in our study as well as the number of simulations and the average point-like source significance. The cumulative density of TS_{ext} is plotted in Figures ?? and ?? and compared to the $\chi^2_1/2$ distribution of Equation ??.

Our study shows broad agreement between simulations and Equation ?. To the extent that there is a discrepancy, the simulations tended to produce smaller than expected values of TS_{ext} which would make the formal significance conservative. Considering the distribution in Figures ?? and ??, the choice of a threshold TS_{ext} set to 16 (corresponding to a formal 4σ significance) is reasonable.

5.3.2 Point-like Source Simulations Over a Structured Background

We performed a second set of simulations to show that the theoretical distribution for TS_{ext} is still preserved when the point-like sources are present over a highly-structured diffuse background. Our simulation setup was the same as above except that the sources were simulated on top of and analyzed assuming the presence of the standard Galactic diffuse and isotropic background models used in 2FGL. In our simulations, we selected our sources to have random positions on the sky such that they were within 5° of the Galactic plane. This probes the brightest and most strongly contrasting areas of the Galactic background.

To limit the number of tests, we selected only one flux level for each of the four spectral indices and we performed this test only in the 1 GeV to 100 GeV energy range. As described below, the fluxes were selected so that $TS \sim 50$. We do not expect to be able to spatially resolve sources at lower fluxes than these, and the results for much brighter sources are less likely to be affected by the structured background.

Because the Galactic diffuse emission is highly structured with strong gradients,

the point-source sensitivity can vary significantly across the Galactic plane. To account for this, we scaled the flux (for a given spectral index) so that the source always has approximately the same signal-to-noise ratio:

$$F(\vec{x}) = F(\text{GC}) \times \left(\frac{B(\vec{x})}{B(\text{GC})} \right)^{1/2}. \quad (5.12)$$

Here, \vec{x} is the position of the simulated source, F is the integral flux of the source from 100 MeV to 100 GeV, $F(\text{GC})$ is the same quantity if the source was at the Galactic center, B is the integral of the Galactic diffuse and isotropic emission from 1 GeV to 100 GeV at the position of the source, and $B(\text{GC})$ is the same quantity if the source was at the Galactic center. For the four spectral models, Table ?? lists $F(\text{GC})$ and the average value of TS.

For each spectrum, we performed $\sim 90,000$ simulations. Figure ?? shows the cumulative density of TS_{ext} for each spectrum. For small values of TS_{ext} , there is good agreement between the simulations and theory. For the highest values of TS_{ext} , there is possibly a small discrepancy, but the discrepancy is not statistically significant. Therefore, we are confident we can use TS_{ext} as a robust measure of statistical significance when testing LAT-detected sources for extension.

5.3.3 Extended Source Simulations Over a Structured Background

We also performed a Monte Carlo study to show that incorrectly modeling the spatial extension of an extended source does not substantially bias the spectral fit of the source, although it does alter the value of the TS. To assess this, we simulated the spatially extended ring-type SNR W44. We selected W44 because it is the most significant extended source detected by the LAT that has a non-radially symmetric photon distribution (Abdo et al. 2010a).

W44 was simulated with a power-law spectral model with an integral flux of 7.12×10^{-8} ph cm $^{-2}$ s $^{-1}$ in the energy range from 1 GeV to 100 GeV and a spectral index of 2.66 (see Section ??).

W44 was simulated with the elliptical ring spatial model described in Abdo et al. (2010a). For reference, the ellipse has a semi-major axis of $0^\circ.3$, a semi-minor axis of $0^\circ.19$, a position angle of 147° measured East of celestial North, and the ring's inner radius is 75% of the outer radius.

We used a simulation setup similar to that described in Section ??, but the simulations were over the 2-year interval of the 2FGL catalog. In the simulations, we did not include the finite energy resolution of the LAT to isolate any effects due to changing the assumed spatial model. The fitting code we use also ignores this energy dispersion and the potential bias introduced by this will be discussed in an upcoming paper by the LAT collaboration (Ackermann et al. 2012). In total, we performed 985 independent simulations.

The simulated sources were fit using a point-like spatial model, a radially-symmetric Gaussian spatial model, a uniform disk spatial model, an elliptical disk spatial model, and finally with an elliptical ring spatial model. We obtained the best fit spatial parameters using `pointlike` and, with these parameters, obtained the best fit spectral parameters using `gtlike`.

Figure 5.6a shows that the significance of W44 in the simulations is very large ($TS \sim 3500$) for a model with a point-like source hypothesis. Figure 5.6b shows that the significance of the spatial extension is also large ($TS_{\text{ext}} \sim 250$). On average TS_{ext} is somewhat larger when fitting the sources with more accurate spatial models. This shows that assuming an incorrect spatial model will cause the source's significance to be underestimated. Figure 5.6c shows that the sources were fit better when assuming an elliptical disk spatial model compared to a uniform disk spatial model ($TS_{\text{elliptical disk}} - TS_{\text{disk}} \sim 30$). Finally, Figure 5.6d shows that the sources were fit somewhat better assuming an elliptical ring spatial model compared to an elliptical disk spatial model ($TS_{\text{elliptical ring}} - TS_{\text{elliptical disk}} \sim 9$). This shows that the LAT has some additional power to resolve substructure in bright extended sources.

Figure 5.7a and Figure 5.7b clearly show that no significant bias is introduced by modeling the source as extended but with an inaccurate spatial model, while a point-like source modeling results in a $\sim 10\%$ and ~ 0.125 bias in the fit flux and index, respectively. Furthermore, Figure 5.7c shows that the r_{68} estimate of the extension size

is very mildly biased ($\sim 10\%$) toward higher values when inaccurate spatial models are used, and thus represents a reasonable measurement of the true 68% containment radius for the source. For the elliptical spatial models, r_{68} is computed by numeric integration.

5.4 Extended Source Detection Threshold

We calculated the LAT flux threshold to detect spatial extent. We define the detection threshold as the flux at which the value of TS_{ext} averaged over many statistical realizations is $\langle TS_{\text{ext}} \rangle = 16$ (corresponding to a formal 4σ significance) for a source of a given extension.

We used a simulation setup similar to that described in Section ??, but instead of point-like sources we simulated extended sources with radially-symmetric uniform disk spatial models. Additionally, we simulated our sources over the two-year time range included in the 2FGL catalog. For each extension and spectral index, we selected a flux range which bracketed $TS_{\text{ext}} = 16$ and performed an extension test for > 100 independent realizations of ten fluxes in the range. We calculated $\langle TS_{\text{ext}} \rangle = 16$ by fitting a line to the flux and TS_{ext} values in the narrow range.

Figure 5.8 shows the threshold for sources of four spectral indices from 1.5 to 3 and extensions varying from $\sigma = 0^\circ.1$ to $2^\circ.0$. The threshold is high for small extensions when the source is small compared to the size of the PSF. It drops quickly with increasing source size and reaches a minimum around $0^\circ.5$. The threshold increases for large extended sources because the source becomes increasingly diluted by the background. Figure 5.8 shows the threshold using photons with energies between 100 MeV and 100 GeV and also using only photons with energies between 1 GeV and 100 GeV. Except for very large or very soft sources, the threshold is not substantially improved by including photons with energies between 100 MeV and 1 GeV. This is also demonstrated in Figure 5.1 which shows TS_{ext} for the SNR IC 443 computed independently in twelve energy bins between 100 MeV and 100 GeV. For IC 443, which has a spectral index ~ 2.4 and an extension $\sim 0^\circ.35$, almost the entire increase in likelihood from optimizing the source extent in the model comes from energies

above 1 GeV. Furthermore, other systematic errors become increasingly large at low energy. For our extension search (Section ??), we therefore used only photons with energies above 1 GeV.

Figure 5.9 shows the flux threshold as a function of source extension for different background levels ($1\times$, $10\times$, and $100\times$ the nominal background), different spectral indices, and two different energy ranges (1 GeV to 100 GeV and 10 GeV to 100 GeV). The detection threshold is higher for sources in regions of higher background. When studying sources only at energies above 1 GeV, the LAT detection threshold (defined as the 1 GeV to 100 GeV flux at which $\langle TS_{\text{ext}} \rangle = 16$) depends less strongly on the spectral index of the source. The index dependence of the detection threshold is even weaker when considering only photons with energies above 10 GeV because the PSF changes little from 10 GeV to 100 GeV. Overlaid on Figure 5.9 are the LAT-detected extended sources that will be discussed in Section ?? and sec??. The extension thresholds are tabulated in Table 5.2.

Finally, Figure 5.10 shows the projected detection threshold of the LAT to extension with a 10 year exposure against 10 times the isotropic background measured by EGRET. This background is representative of the background near the Galactic plane. For small extended sources, the threshold improves by a factor larger than the square root of the relative exposures because the LAT is signal-limited at high energies where the present analysis is most sensitive. For large extended sources, the relevant background is over a larger spatial range and so the improvement is closer to a factor corresponding to the square root of the relative exposures that is caused by Poisson fluctuations in the background.

5.5 Testing Against Source Confusion

It is impossible to discriminate using only LAT data between a spatially extended source and multiple point-like sources separated by angular distances comparable to or smaller than the size of the LAT PSF. To assess the plausibility of source confusion for sources with $TS_{\text{ext}} \geq 16$, we developed an algorithm to test if a region contains two point-like sources. The algorithm works by simultaneously fitting in `pointlike`

the positions and spectra of the two point-like sources. To help with convergence, it begins by dividing the source into two spatially coincident point-like sources and then fitting the sum and difference of the positions of the two sources without any limitations on the fit parameters.

After simultaneously fitting the two positions and two spectra, we define $\text{TS}_{2\text{pts}}$ as twice the increase in the log of the likelihood fitting the region with two point-like sources compared to fitting the region with one point-like source:

$$\text{TS}_{2\text{pts}} = 2 \log(\mathcal{L}_{2\text{pts}}/\mathcal{L}_{\text{ps}}). \quad (5.13)$$

For the following analysis of LAT data, $\text{TS}_{2\text{pts}}$ was computed by fitting the spectra of the two point-like sources in `gtlike` using the best fit positions of the sources found by `pointlike`.

$\text{TS}_{2\text{pts}}$ cannot be quantitatively compared to TS_{ext} using a simple likelihood-ratio test to evaluate which model is significantly better because the models are not nested (Protassov et al. 2002). Even though the comparison of TS_{ext} with $\text{TS}_{2\text{pts}}$ is not a calibrated test, $\text{TS}_{\text{ext}} > \text{TS}_{2\text{pts}}$ indicates that the likelihood for the extended source hypothesis is higher than for two point-like sources and we only consider a source to be extended if $\text{TS}_{\text{ext}} > \text{TS}_{2\text{pts}}$.

We considered using the Bayesian information criterion (BIC, Schwarz 1978) as an alternative Bayesian formulation for this test, but it is difficult to apply to LAT data because it contains a term including the number of data points. For studying γ -ray sources in LAT data, we analyze relatively large regions of the sky to better define the contributions from diffuse backgrounds and nearby point sources. This is important for accurately evaluating source locations and fluxes but the fraction of data directly relevant to the evaluation of the parameters for the source of interest is relatively small.

As an alternative, we considered the Akaike information criterion test (AIC, Akaike 1974). The AIC is defined as $\text{AIC} = 2k - 2 \log \mathcal{L}$, where k is the number of parameters in the model. In this formulation, the best hypothesis is considered to be the one that minimizes the AIC. The first term penalizes models with additional

parameters.

The two point-like sources hypothesis has three more parameters than the single extended source hypothesis (two more spatial parameters and two more spectral parameters compared to one extension parameter), so the comparison $\text{AIC}_{\text{ext}} < \text{AIC}_{2\text{pts}}$ is formally equivalent to $\text{TS}_{\text{ext}} + 6 > \text{TS}_{2\text{pts}}$. Our criterion for accepting extension ($\text{TS}_{\text{ext}} > \text{TS}_{2\text{pts}}$) is thus equivalent to requesting that the AIC-based empirical support for the two point-like sources model be “considerably less” than for the extended source model, following the classification by Burnham & Anderson (2002).

We assessed the power of the $\text{TS}_{\text{ext}} > \text{TS}_{2\text{pts}}$ test with a Monte Carlo study. We simulated one spatially extended source and fit it as both an extended source and as two point-like sources using `pointlike`. We then simulated two point-like sources and fit them with the same two hypotheses. By comparing the distribution of $\text{TS}_{2\text{pts}}$ and TS_{ext} computed by `pointlike` for the two cases, we evaluated how effective the $\text{TS}_{\text{ext}} > \text{TS}_{2\text{pts}}$ test is at rejecting cases of source confusion as well as how likely it is to incorrectly reject that an extended source is spatially extended. All sources were simulated using the same time range as in Section ?? against a background 10 times the isotropic background measured by EGRET, representative of the background near the Galactic plane.

We did this study first in the energy range from 1 GeV to 100 GeV by simulating extended sources of flux $4 \times 10^{-9} \text{ ph cm}^{-2}\text{s}^{-1}$ integrated from 1 GeV to 100 GeV and a power-law spectral model with spectral index 2. This spectrum was picked to be representative of the new extended sources that were discovered in the following analysis when looking in the 1 GeV to 100 GeV energy range (see Section ??). We simulated these sources using uniform disk spatial models with extensions varying up to 1° . Figure 5.11a shows the distribution of TS_{ext} and $\text{TS}_{2\text{pts}}$ and Figure 5.11c shows the distribution of $\text{TS}_{\text{ext}} - \text{TS}_{2\text{pts}}$ as a function of the simulated extension of the source for 200 statistically independent simulations.

Figure 5.12a shows the same plot but when fitting two simulated point-like sources each with half of the flux of the spatially extended source and with the same spectral index as the extended source. Finally, Figure 5.12c shows the same plot with each point-like source having the same flux but different spectral indices. One point-like

source had a spectral index of 1.5 and the other an index of 2.5. These indices are representative of the range of indices of LAT-detected sources.

The same four plots are shown in Figure ??b, ??d, ??b, and ??d but this time when analyzing a source of flux 10^{-9} ph cm $^{-2}$ s $^{-1}$ (integrated from 10 GeV to 100 GeV) only in the 10 GeV to 100 GeV energy range. This flux is typical of the new extended sources discovered using only photons with energies between 10 GeV and 100 GeV (see Section ??).

Several interesting conclusions can be made from this study. As one would expect, $TS_{\text{ext}} - TS_{2\text{pts}}$ is mostly positive when fitting the simulated extended sources. In the 1 GeV to 100 GeV analysis, only 11 of the 200 simulated extended sources had $TS_{\text{ext}} > 16$ but were incorrectly rejected due to $TS_{2\text{pts}}$ being greater than TS_{ext} . In the 10 GeV to 100 GeV analysis, only 7 of the 200 sources were incorrectly rejected. From this, we conclude that this test is unlikely to incorrectly reject truly spatially extended sources.

On the other hand, it is often the case that $TS_{\text{ext}} > 16$ when testing the two simulated point-like sources for extension. This is especially the case when the two sources had the same spectral index. Forty out of 200 sources in the 1 GeV to 100 GeV energy range and 43 out of 200 sources in the 10 GeV to 100 GeV energy range had $TS_{\text{ext}} > 16$. But in these cases, we always found the single extended source fit to be worse than the two point-like source fit. From this, we conclude that the $TS_{\text{ext}} > TS_{2\text{pts}}$ test is powerful at discarding cases in which the true emission comes from two point-like sources.

The other interesting feature in Figure ??a and ??b is that for simulated extended sources with typical sizes ($\sigma \sim 0.5^\circ$), one can often obtain almost as large an increase in likelihood fitting the source as two point-like sources ($TS_{2\text{pts}} \sim TS_{\text{ext}}$). This is because although the two point-like sources represent an incorrect spatial model, the second source has four additional degrees of freedom (two spatial and two spectral parameters) and can therefore easily model much of the extended source and statistical fluctuations in the data. This effect is most pronounced when using photons with energies between 1 GeV and 100 GeV where the PSF is broader.

From this Monte Carlo study, we can see the limits of an analysis with LAT data

of spatially extended sources. Section ?? showed that we have a statistical test that finds when a LAT source is not well described by the PSF. But this test does not uniquely prove that the emission originates from spatially extended emission instead of from multiple unresolved sources. Demanding that $TS_{\text{ext}} > TS_{2\text{pts}}$ is a powerful second test to avoid cases of simple confusion of two point-like sources. But it could always be the case that an extended source is actually the superposition of multiple point-like or extended sources that could be resolved with deeper observations of the region. There is nothing about this conclusion unique to analyzing LAT data, but the broad PSF of the LAT and the density of sources expected to be GeV emitters in the Galactic plane makes this issue more significant for analyses of LAT data. When possible, multiwavelength information should be used to help select the best model of the sky.

5.6 Test of 2LAC Sources

For all following analyses of LAT data, we used the same two-year dataset that was used in the 2FGL catalog spanning from 2008 August 4 to 2010 August 1. We applied the same acceptance cuts and we used the same P7_V6 Source class event selection and IRFs (Ackermann et al. 2012). When analyzing sources in `pointlike`, we used a circular 10° region of interest (ROI) centered on our source and eight energy bins per logarithmic decade in energy. When refitting the region in `gtlike` using the best fit spatial and spectral models from `pointlike`, we used the ‘binned likelihood’ mode of `gtlike` on a $14^\circ \times 14^\circ$ ROI with a pixel size of $0^\circ03$.

Unless explicitly mentioned, we used the same background model as 2FGL to represent the Galactic diffuse, isotropic, and Earth limb emission. To compensate for possible residuals in the diffuse emission model, the Galactic emission was scaled by a power-law and the normalization of the isotropic component was left free. Unless explicitly mentioned, we used all 2FGL sources within 15° of our source as our list of background sources and we refit the spectral parameters of all sources within 2° of the source.

To validate our method, we tested LAT sources associated with AGN for extension. GeV emission from AGN is believed to originate from collimated jets. Therefore AGN are not expected to be spatially resolvable by the LAT and provide a good calibration source to demonstrate that our extension detection method does not misidentify point-like sources as being extended. We note that megaparsec-scale γ -ray halos around AGNs have been hypothesized to be resolvable by the LAT (Aharonian et al. 1994). However, no such halo has been discovered in the LAT data so far (Neronov et al. 2011).

Following 2FGL, the LAT Collaboration published the Second LAT AGN Catalog (2LAC), a list of high latitude ($|b| > 10^\circ$) sources that had a high probability association with AGN (Ackermann et al. 2011). 2LAC associated 1016 2FGL sources with AGN. To avoid systematic problems with AGN classification, we selected only the 885 AGN which made it into the clean AGN sub-sample defined in the 2LAC paper. An AGN association is considered clean only if it has a high probability of association $P \geq 80\%$, if it is the only AGN associated with the 2FGL source, and if no analysis flags have been set for the source in the 2FGL catalog. These last two conditions are important for our analysis. Source confusion may look like a spatially extended source and flagged 2FGL sources may correlate with unmodeled structure in the diffuse emission.

Of the 885 clean AGN, we selected the 733 of these 2FGL sources which were significantly detected above 1 GeV and fit each of them for extension. The cumulative density of TS_{ext} for these AGN is compared to the $\chi^2_1/2$ distribution of Equation ?? in Figure ?. The TS_{ext} distribution for the AGN shows reasonable agreement with the theoretical distribution and no AGN was found to be significantly extended ($\text{TS}_{\text{ext}} > 16$). The observed discrepancy from the theoretical distribution is likely due to small systematics in our model of the LAT PSF and the Galactic diffuse emission (see Section ??). The discrepancy could also in a few cases be due to confusion with a nearby undetected source. We note that the Monte Carlo study of section ?? effectively used perfect IRFs and a perfect model of the sky. The overall agreement with the expected distribution demonstrates that we can use TS_{ext} as a measure of the statistical significance of the detection of the extension of a source.

We note that the LAT PSF used in this study was determined empirically by fitting the distributions of gamma rays around bright AGN (see Section ??). Finding that the AGN we test are not extended is not surprising. This validation analysis is not suitable to reject any hypotheses about the existence of megaparsec-scale halos around AGN.

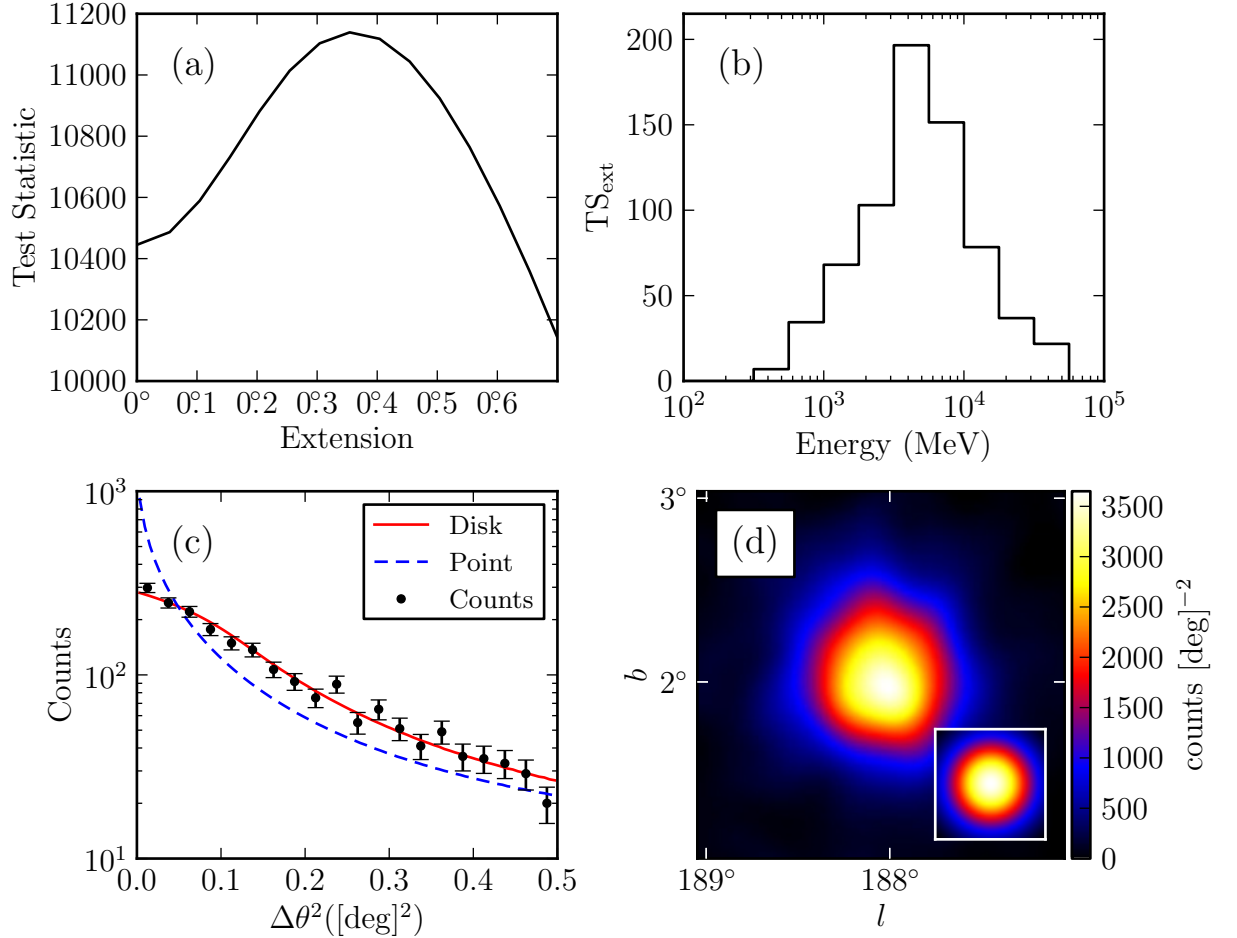


Figure 5.1 Counts maps and TS profiles for the SNR IC 443. (a) TS vs. extension of the source. (b) TS_{ext} for individual energy bands. (c) observed radial profile of counts in comparison to the expected profiles for a spatially extended source (solid and colored red in the online version) and for a point-like source (dashed and colored blue in the online version). (d) smoothed counts map after subtraction of the diffuse emission compared to the smoothed LAT PSF (inset). Both were smoothed by a 0.1×0.1 2D Gaussian kernel. Plots (a), (c), and (d) use only photons with energies between 1 GeV and 100 GeV. Plots (c) and (d) include only photons which converted in the front part of the tracker and have an improved angular resolution (Atwood et al. 2009).

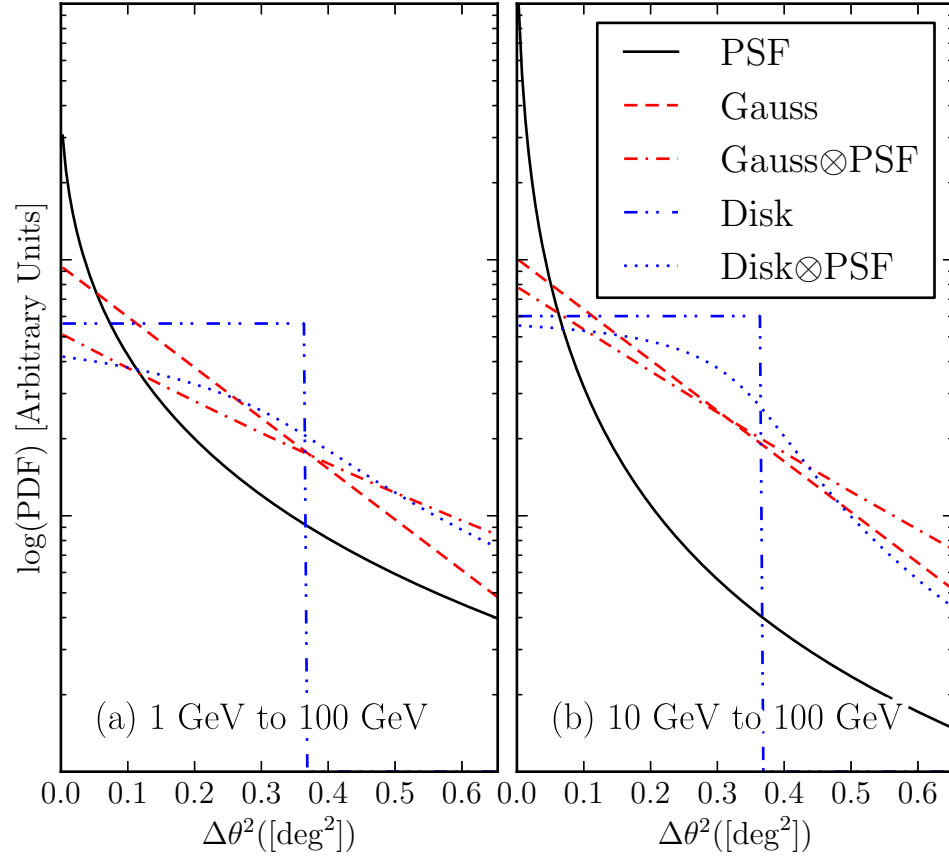


Figure 5.2 A comparison of a 2D Gaussian and uniform disk spatial model of extended sources before and after convolving with the PSF for two energy ranges. The solid black line is the PSF that would be observed for a power-law source of spectral index 2. The dashed line and the dash-dotted lines are the brightness profile of a Gaussian with $r_{68} = 0.5$ and the convolution of this profile with the LAT PSF respectively (colored red in the online version). The dash-dot-dotted and the dot-dotted lines are the brightness profile of a uniform disk with $r_{68} = 0.5$ and the convolution of this profile with the LAT PSF respectively (colored blue in the online version).

Table 5.1. Monte Carlo Spectral Parameters

Spectral Index	Flux ^(a) (ph cm ⁻² s ⁻¹)	$N_{1-100\text{GeV}}$	$\langle\text{TS}\rangle_{1-100\text{GeV}}$	$N_{10-100\text{GeV}}$	$\langle\text{TS}\rangle_{10-100\text{GeV}}$
Isotropic Background					
1.5	3×10^{-7}	18938	22233	18938	8084
	10^{-7}	19079	5827	19079	2258
	3×10^{-8}	19303	1276	19303	541
	10^{-8}	19385	303	19381	142
	3×10^{-9}	18694	62	12442	43
2	10^{-6}	18760	22101	18760	3033
	3×10^{-7}	18775	4913	18775	730
	10^{-7}	18804	1170	18803	192
	3×10^{-8}	18836	224	15256	50
	10^{-8}	17060	50
2.5	3×10^{-6}	18597	19036	18597	786
	10^{-6}	18609	4738	18608	208
	3×10^{-7}	18613	954	15958	53
	10^{-7}	18658	203
	3×10^{-8}	14072	41
3	10^{-5}	18354	19466	18354	215
	3×10^{-6}	18381	4205	15973	54
	10^{-6}	18449	966
	3×10^{-7}	18517	174
	10^{-7}	13714	41
Galactic Diffuse and Isotropic Background ^(b)					
1.5	2.3×10^{-8}	90741	63
2	1.2×10^{-7}	92161	60
2.5	4.5×10^{-7}	86226	47
3	2.0×10^{-6}	94412	61

^(a)Integral 100 MeV to 100 GeV flux.

^(b) For the Galactic simulations, the quoted fluxes are the fluxes for sources placed in the Galactic center. The actual fluxes are scaled by Equation 5.12.

Note. — A list of the spectral models of the simulated point-like sources which were tested for extension. For each model, the number of statistically independent simulations and the average value of TS is also tabulated. The top rows are the simulations on top of an isotropic background and the bottom rows are the simulations on top of the Galactic diffuse and isotropic background.

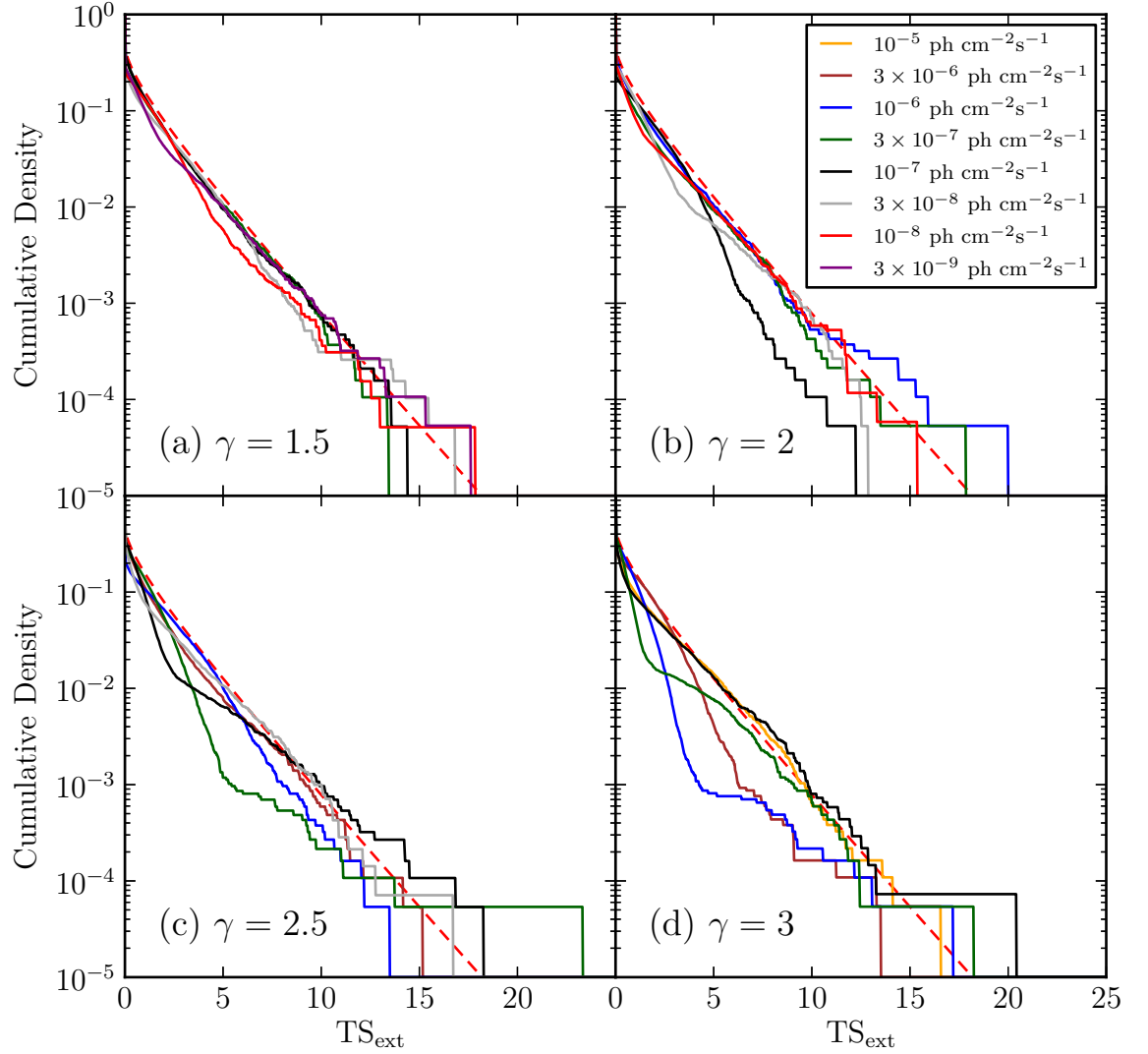


Figure 5.3 Cumulative distribution of the TS for the extension test when fitting simulated point-like sources in the 1 GeV to 100 GeV energy range. The four plots represent simulated sources of different spectral indices and the different lines (colored in the online version) represent point-like sources with different 100 MeV to 100 GeV integral fluxes. The dashed line (colored red) is the cumulative density function of Equation 5.11.

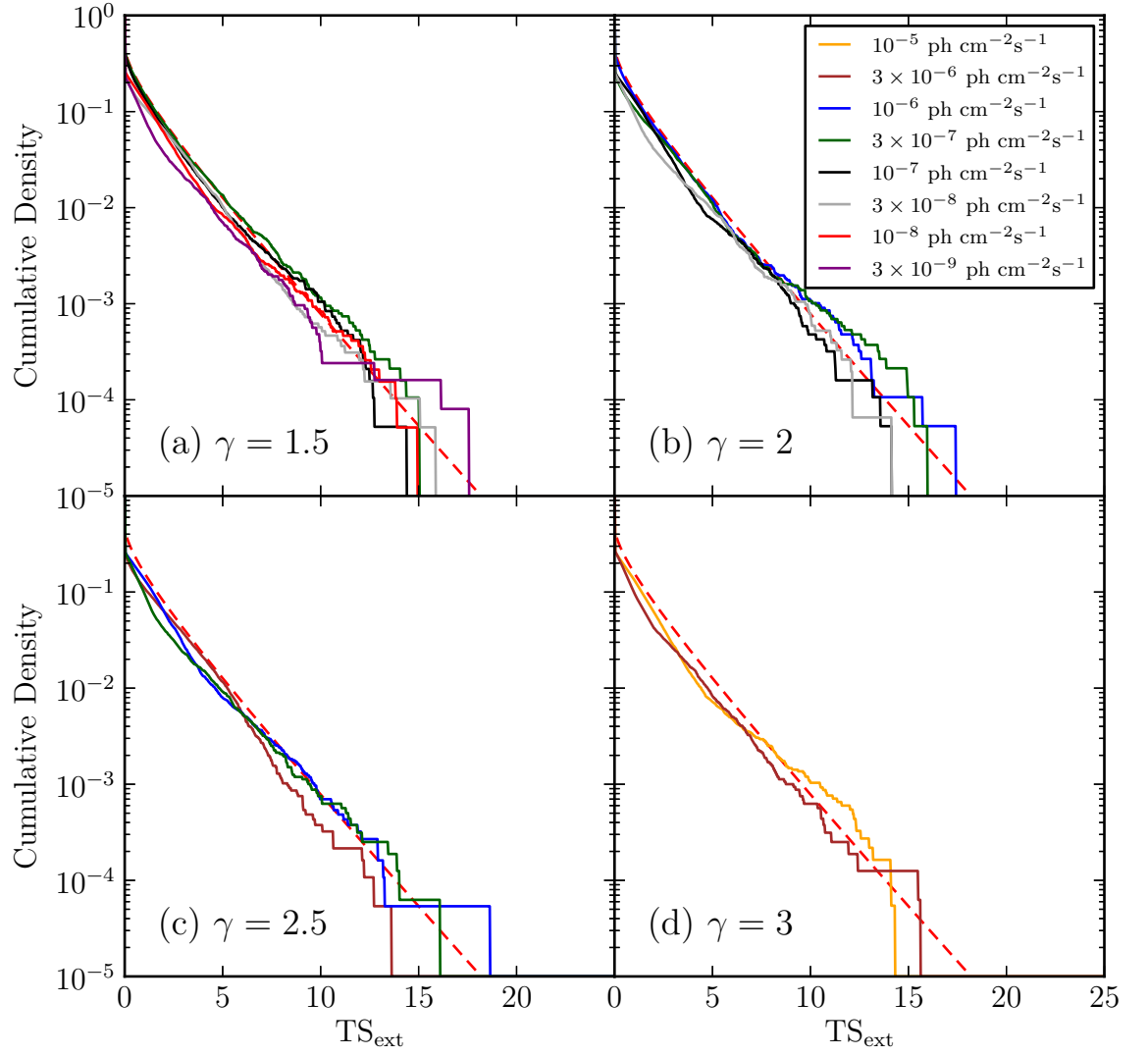


Figure 5.4 The same plot as Figure ?? but fitting in the 10 GeV to 100 GeV energy range.

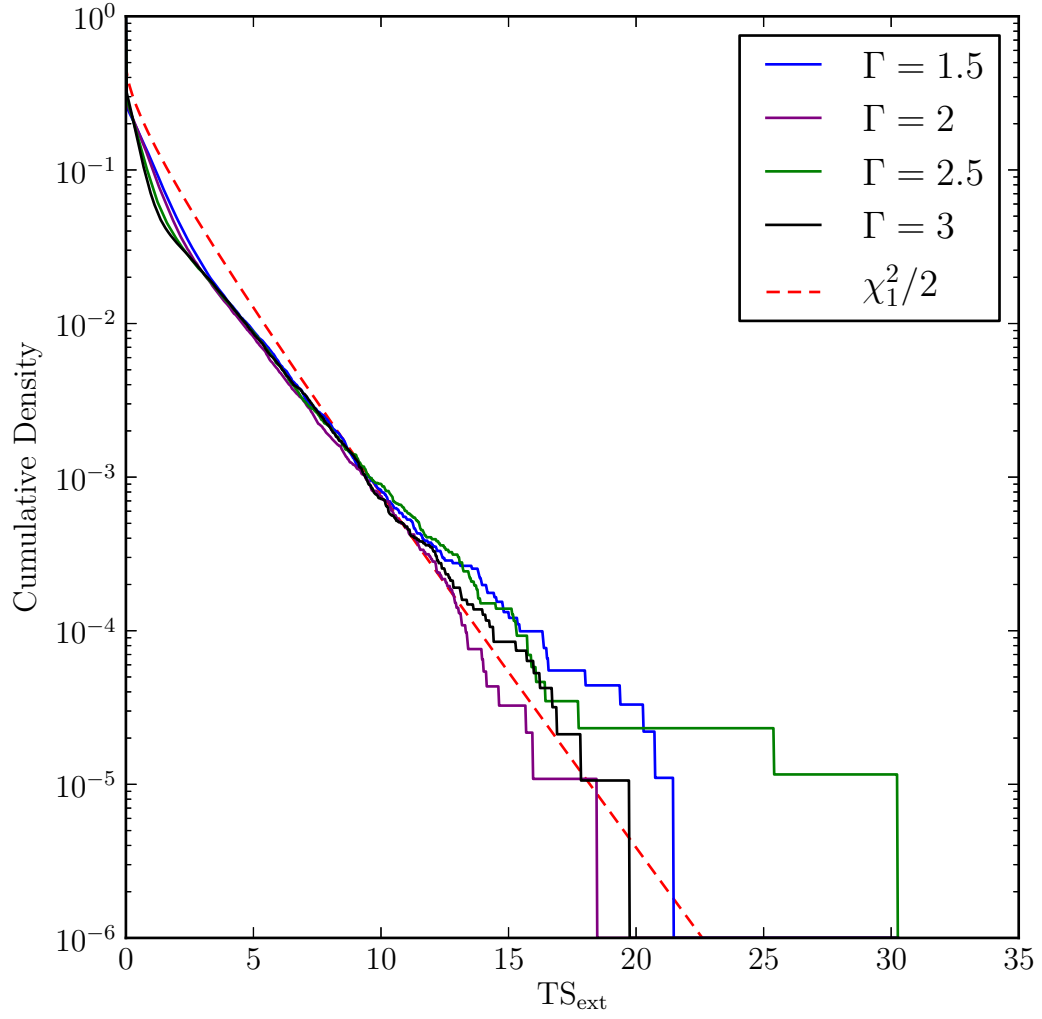


Figure 5.5 Cumulative distribution of TS_{ext} for sources simulated on top of the Galactic diffuse and isotropic background.

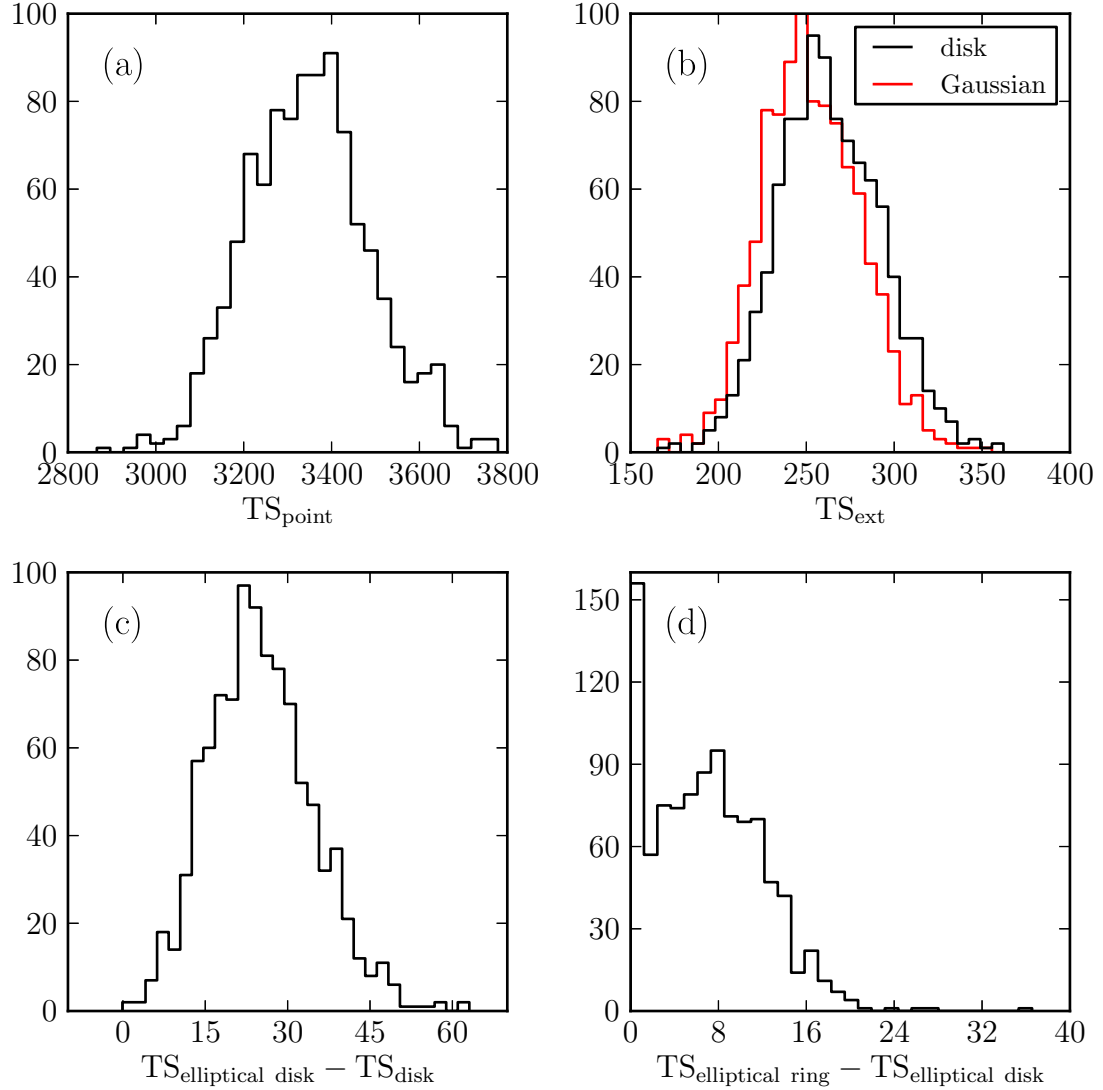


Figure 5.6 The distribution of TS values when fitting 985 statistically independent simulations of W44. (a) is the distribution of TS values when fitting W44 as a point-like source and (b) is the distribution of TS_{ext} when fitting the source with a uniform disk or a radially-symmetric Gaussian spatial model. (c) is the distribution of the change in TS when fitting the source with an elliptical disk spatial model compared to fitting it with a radially-symmetric disk spatial model and (d) when fitting the source with an elliptical ring spatial model compared to an elliptical disk spatial model.

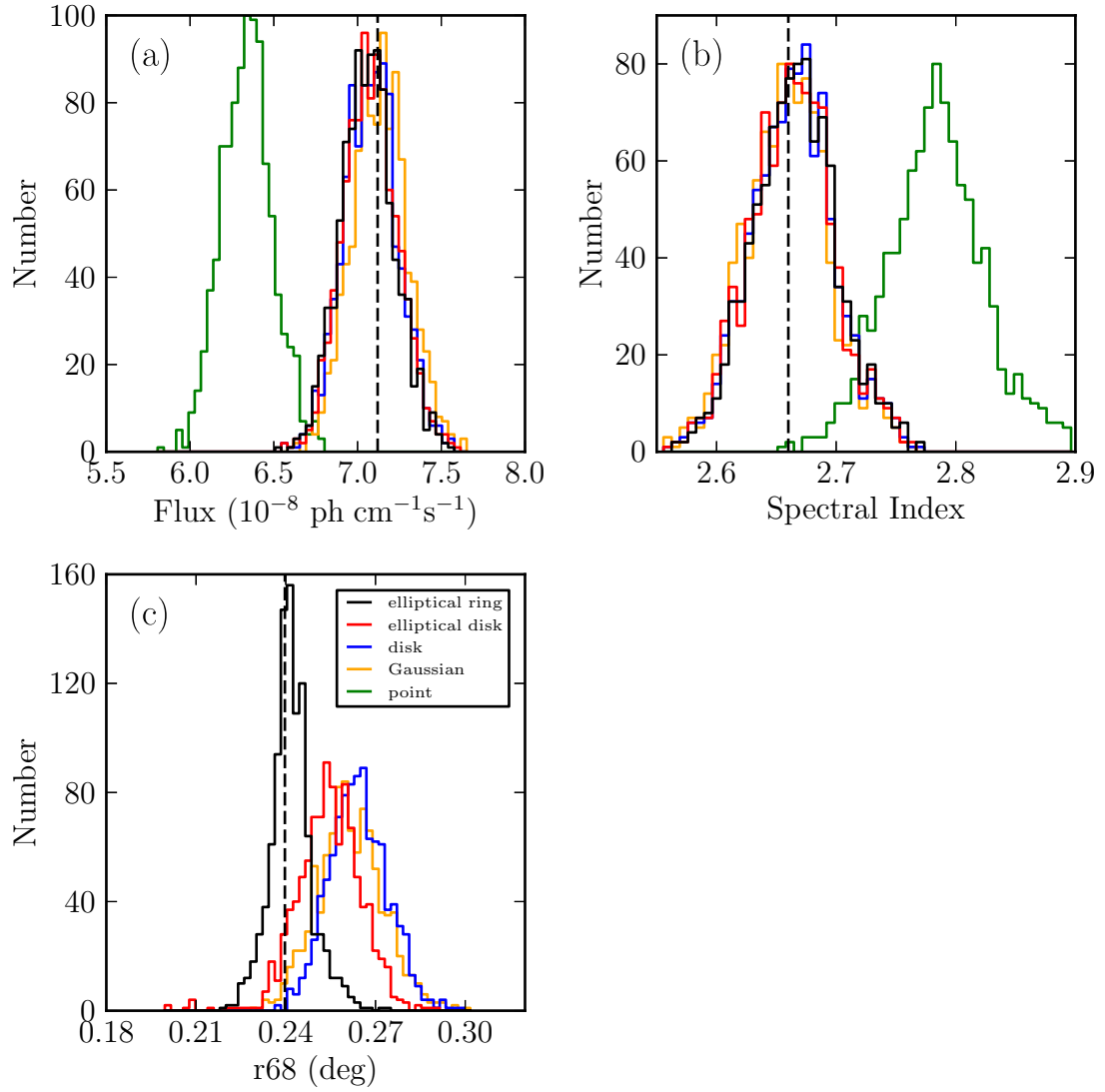


Figure 5.7 The distribution of fit parameters for the Monte Carlo simulations of W44. The plots show the distribution of best fit (a) flux (b) spectral index and (c) 68% containment radius. The dashed vertical lines represent the simulated values of the parameters.

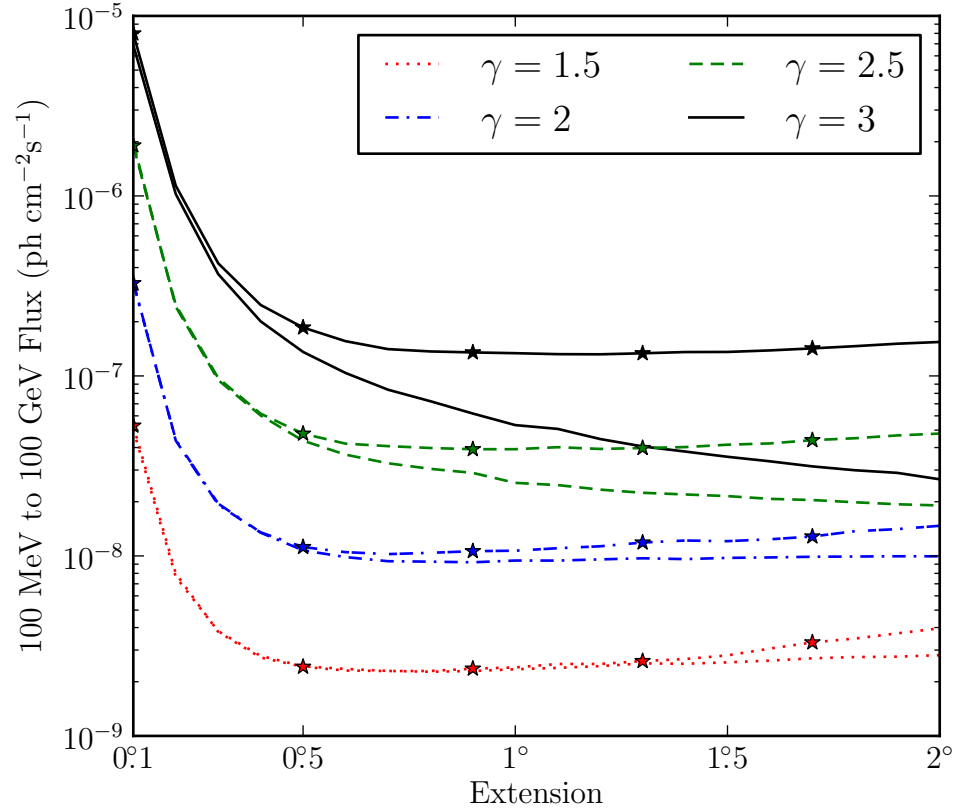


Figure 5.8 The detection threshold to resolve an extended source with a uniform disk model for a two-year exposure. All sources have an assumed power-law spectrum and the different line styles (colors in the electronic version) correspond to different simulated spectral indices. The lines with no markers correspond to the detection threshold using photons with energies between 100 MeV and 100 GeV, while the lines with star-shaped markers correspond to the threshold using photons with energies between 1 GeV and 100 GeV.

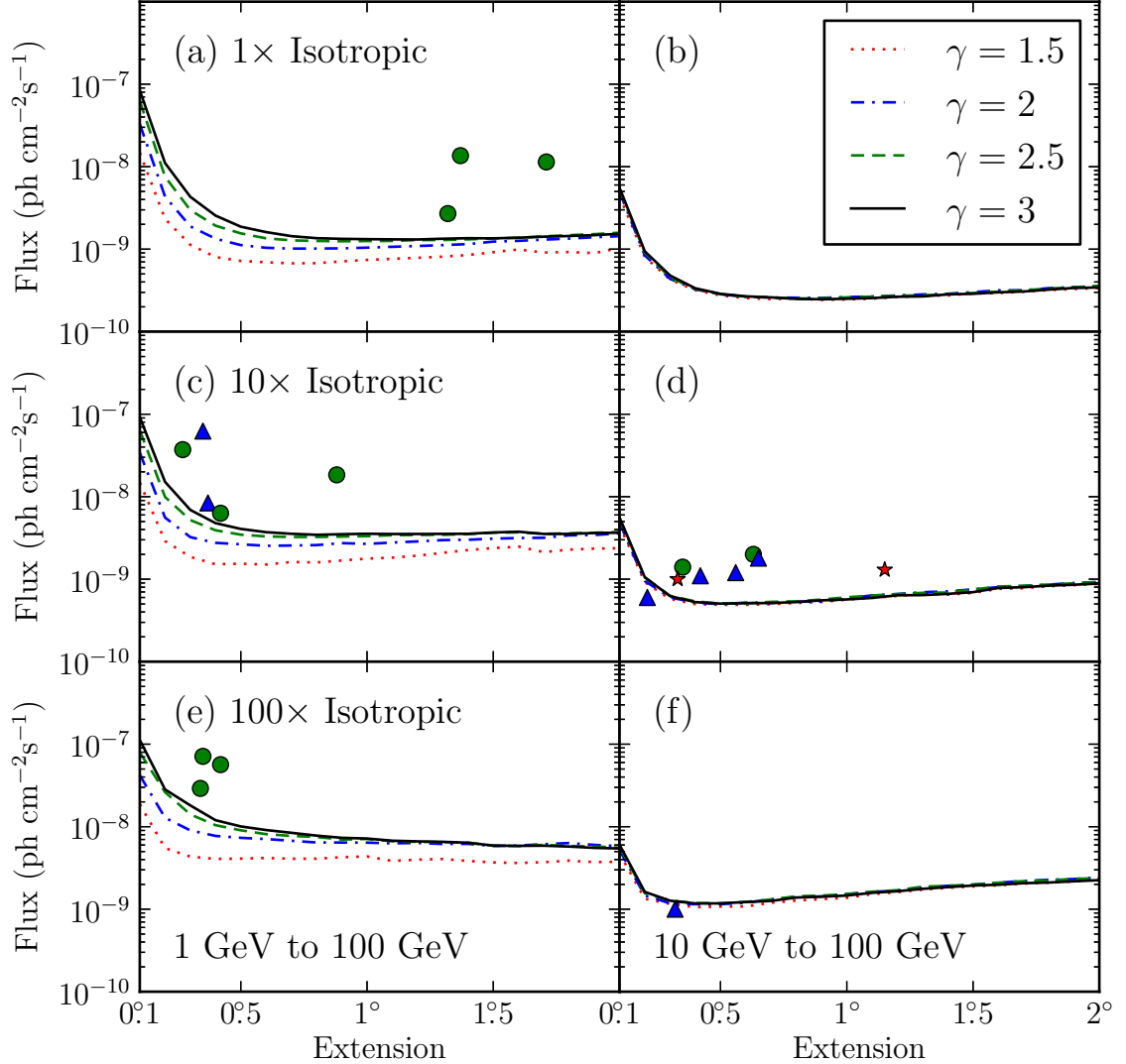


Figure 5.9 The LAT detection threshold for four spectral indices and three backgrounds ($1\times$, $10\times$, and $100\times$ the Sreekumar-like isotropic background) for a two-year exposure. The left-hand plots are the detection threshold when using photons with energies between 1 GeV and 100 GeV and the right-hand plots are the detection threshold when using photons with energies between 10 GeV and 100 GeV. The flux is integrated only in the selected energy range. Overlaid on this plot are the LAT-detected extended sources placed by the magnitude of the nearby Galactic diffuse emission and the energy range they were analyzed with. The star-shaped markers (colored red in the electronic version) are sources with a spectral index closer to 1.5, the triangular markers (colored blue) an index closer to 2, and the circular markers (colored green) an index closer to 2.5. The triangular marker in plot (d) below the sensitivity line is MSH 15–52.

Table 5.2. Extension Detection Threshold

γ	BG	0.1	0.2	0.3	0.4	0.5	0.6	0.7	0.8	0.9	1.0	1.1	1.2	1.3	1.4	1.5	1.6	1.7	1.8	1.9	2.0
E>1 GeV																					
1.5	1×	148.1	23.3	11.3	8.0	7.2	6.9	6.7	6.8	7.1	7.4	7.6	7.9	8.1	8.5	9.2	9.9	9.1	9.2	9.0	10.3
	10×	148.4	29.0	18.7	15.2	15.4	15.0	16.1	16.0	16.8	17.7	18.2	19.3	20.9	22.5	23.8	24.8	21.3	22.8	23.4	23.7
	100×	186.8	55.0	43.4	40.7	41.0	41.8	40.9	40.9	42.7	43.6	38.4	39.9	40.6	38.4	36.9	36.3	37.1	38.8	37.2	37.6
2	1×	328.4	43.4	18.9	13.4	11.2	10.4	10.2	10.2	10.2	10.4	10.7	10.9	11.2	11.5	12.4	12.6	13.0	13.4	14.0	14.4
	10×	341.0	55.9	32.3	27.6	26.5	25.4	25.6	25.9	27.4	26.8	27.8	28.7	29.8	30.1	31.0	31.5	31.7	34.0	34.3	35.9
	100×	420.5	128.3	90.2	77.3	73.3	70.8	67.5	64.3	64.2	64.1	62.8	63.6	61.7	61.9	58.4	59.0	61.4	63.3	60.1	58.1
2.5	1×	627.1	75.6	29.8	19.3	15.5	13.5	12.8	12.6	12.5	12.5	12.6	12.9	13.1	13.5	13.7	13.7	14.3	14.8	15.2	15.8
	10×	638.9	99.1	52.1	39.1	34.6	33.0	32.5	32.5	32.8	33.2	34.1	34.3	34.5	35.1	36.6	36.9	35.5	36.0	36.5	37.3
	100×	795.0	262.1	140.9	104.3	90.4	81.2	77.2	75.1	69.7	70.9	66.5	65.6	64.9	64.0	58.9	58.1	60.2	58.4	57.5	55.8
3	1×	841.5	110.6	43.2	25.5	18.7	16.1	14.4	13.6	13.3	13.2	13.1	13.1	13.4	13.6	13.5	13.8	14.2	14.4	14.8	15.4
	10×	921.6	151.3	69.1	47.8	40.7	37.1	35.5	34.5	35.1	35.5	35.3	35.3	35.4	35.5	36.8	37.6	35.3	35.4	36.3	36.6
	100×	1124.1	282.9	181.1	119.8	100.7	91.1	84.3	77.9	73.3	71.8	67.6	66.4	65.5	63.9	59.0	58.6	58.8	57.5	55.4	54.4
E>10 GeV																					
1.5	1×	44.6	8.0	4.3	3.2	2.7	2.6	2.5	2.5	2.4	2.5	2.5	2.6	2.7	2.8	2.9	2.9	3.1	3.2	3.3	3.4
	10×	45.2	9.2	5.8	5.0	4.9	4.9	5.0	5.2	5.3	5.7	5.9	6.3	6.6	6.5	6.8	7.6	7.8	8.2	8.5	8.7
	100×	47.3	13.4	11.6	10.6	10.8	10.8	12.0	12.7	13.2	13.7	15.3	16.1	17.2	18.2	18.9	19.5	20.4	21.0	21.7	22.9
2	1×	49.7	8.4	4.4	3.3	2.8	2.6	2.6	2.6	2.6	2.6	2.7	2.7	2.8	2.9	3.0	3.2	3.2	3.4	3.5	3.5
	10×	48.6	9.5	6.0	5.2	5.0	5.2	5.2	5.3	5.4	5.8	6.4	6.6	7.0	7.1	7.5	8.0	8.3	8.6	9.0	9.2
	100×	51.8	14.7	11.8	11.5	11.5	11.9	13.2	14.0	14.3	15.3	16.2	16.9	18.4	19.2	19.8	21.0	22.0	22.8	23.2	24.3
2.5	1×	53.1	9.1	4.5	3.3	2.8	2.7	2.6	2.5	2.5	2.6	2.7	2.7	2.8	2.8	2.9	3.1	3.2	3.3	3.5	3.6
	10×	53.7	10.5	6.3	5.4	5.1	5.1	5.3	5.4	5.7	6.0	6.3	6.6	6.8	6.9	7.5	8.1	8.3	8.6	8.9	9.2
	100×	57.0	15.6	12.7	11.9	11.8	12.2	13.1	14.3	14.6	15.2	16.3	17.0	18.8	19.2	19.9	21.0	21.9	22.3	23.3	23.7
3	1×	55.5	9.4	4.8	3.4	2.9	2.7	2.6	2.5	2.5	2.5	2.6	2.7	2.7	2.8	2.9	3.0	3.1	3.2	3.4	3.4
	10×	56.0	10.5	6.2	5.3	5.1	5.1	5.1	5.3	5.5	5.7	5.9	6.4	6.4	6.6	7.0	7.8	8.0	8.3	8.6	8.9
	100×	60.3	16.2	12.7	11.7	11.8	12.2	12.6	13.8	14.2	14.6	15.8	16.5	17.6	18.5	19.4	19.8	20.7	21.0	21.8	22.5

Table 5.2 (cont'd)

γ	BG	0.1	0.2	0.3	0.4	0.5	0.6	0.7	0.8	0.9	1.0	1.1	1.2	1.3	1.4	1.5	1.6	1.7	1.8	1.9	2.0
----------	----	-----	-----	-----	-----	-----	-----	-----	-----	-----	-----	-----	-----	-----	-----	-----	-----	-----	-----	-----	-----

Note. — The detection threshold to resolve spatially extended sources with a uniform disk spatial model for a two-year exposure The threshold is calculated for sources of varying energy ranges, spectral indices, and background levels. The sensitivity was calculated against a Sreekumar-like isotropic background and the second column is the factor that the simulated background was scaled by. The remaining columns are varying sizes of the source. The table quotes integral fluxes in the analyzed energy range (1 GeV to 100 GeV or 10 GeV to 100 GeV) in units of 10^{-10} ph cm $^{-2}$ s $^{-1}$.

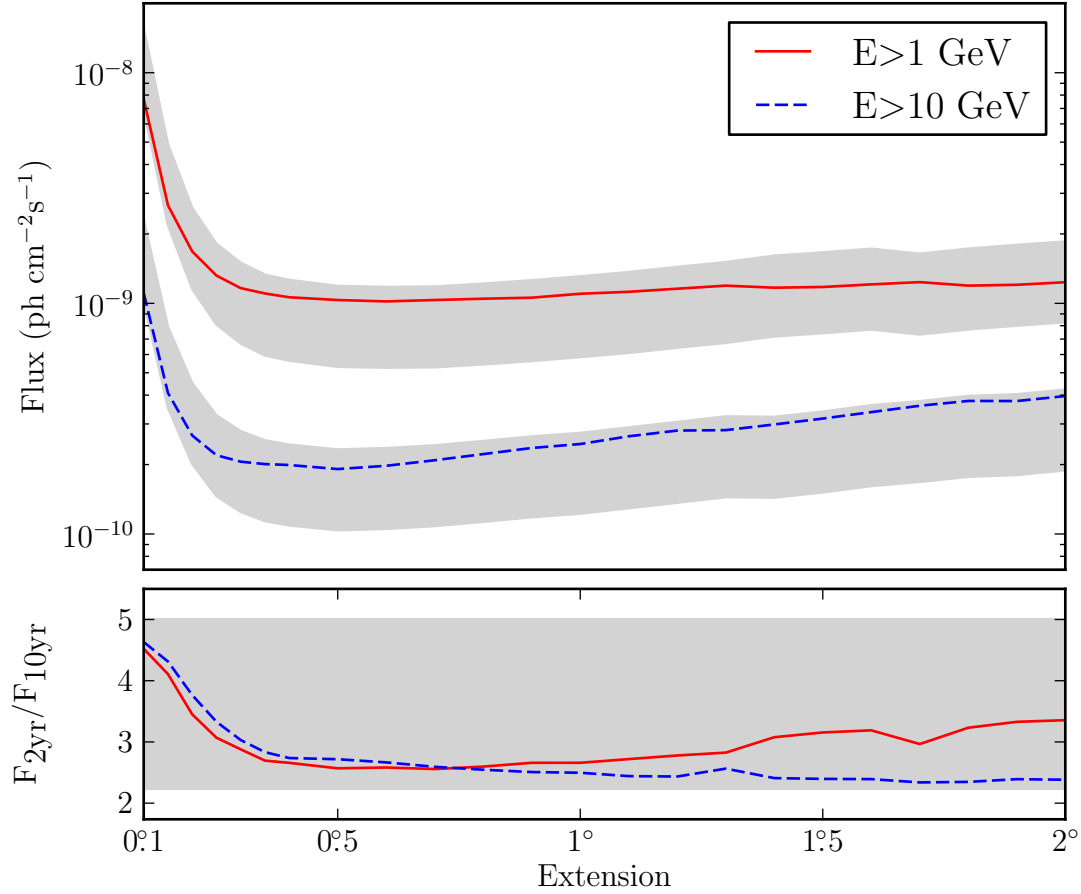


Figure 5.10 The projected detection threshold of the LAT to extension after 10 years for a power-law source of spectral index 2 against 10 times the isotropic background in the energy range from 1 GeV to 100 GeV (solid line colored red in the electronic version) and 10 GeV to 100 GeV (dashed line colored blue). The shaded gray regions represent the detection threshold assuming the sensitivity improves from 2 to 10 years by the square root of the exposure (top edge) and linearly with exposure (bottom edge). The lower plot shows the factor increase in sensitivity. For small extended sources, the detection threshold of the LAT to the extension of a source will improve by a factor larger than the square root of the exposure.

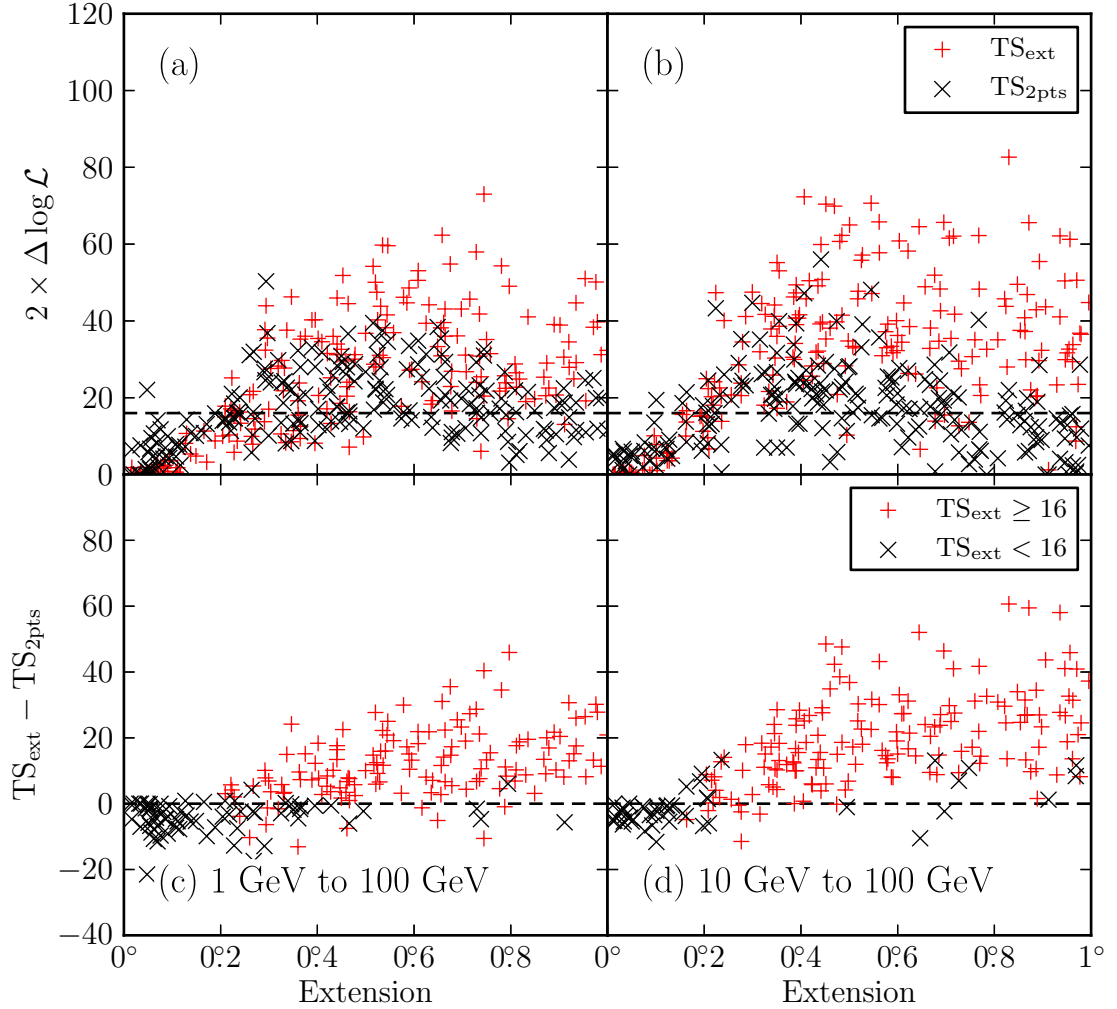


Figure 5.11 (a) and (b) are the distribution of TS_{ext} and of $TS_{2\text{pts}}$ when fitting simulated spatially extended sources of varying sizes as both an extended source and as two point-like sources. (c) and (d) are the distribution of $TS_{\text{ext}} - TS_{2\text{pts}}$ for the same simulated sources. (a) and (c) represent sources fit in the 1 GeV to 100 GeV energy range and (b) and (d) represent sources fit in the 10 GeV to 100 GeV energy range. In (c) and (d), the plus-shaped markers (colored red in the electronic version) are fits where $TS_{\text{ext}} \geq 16$.

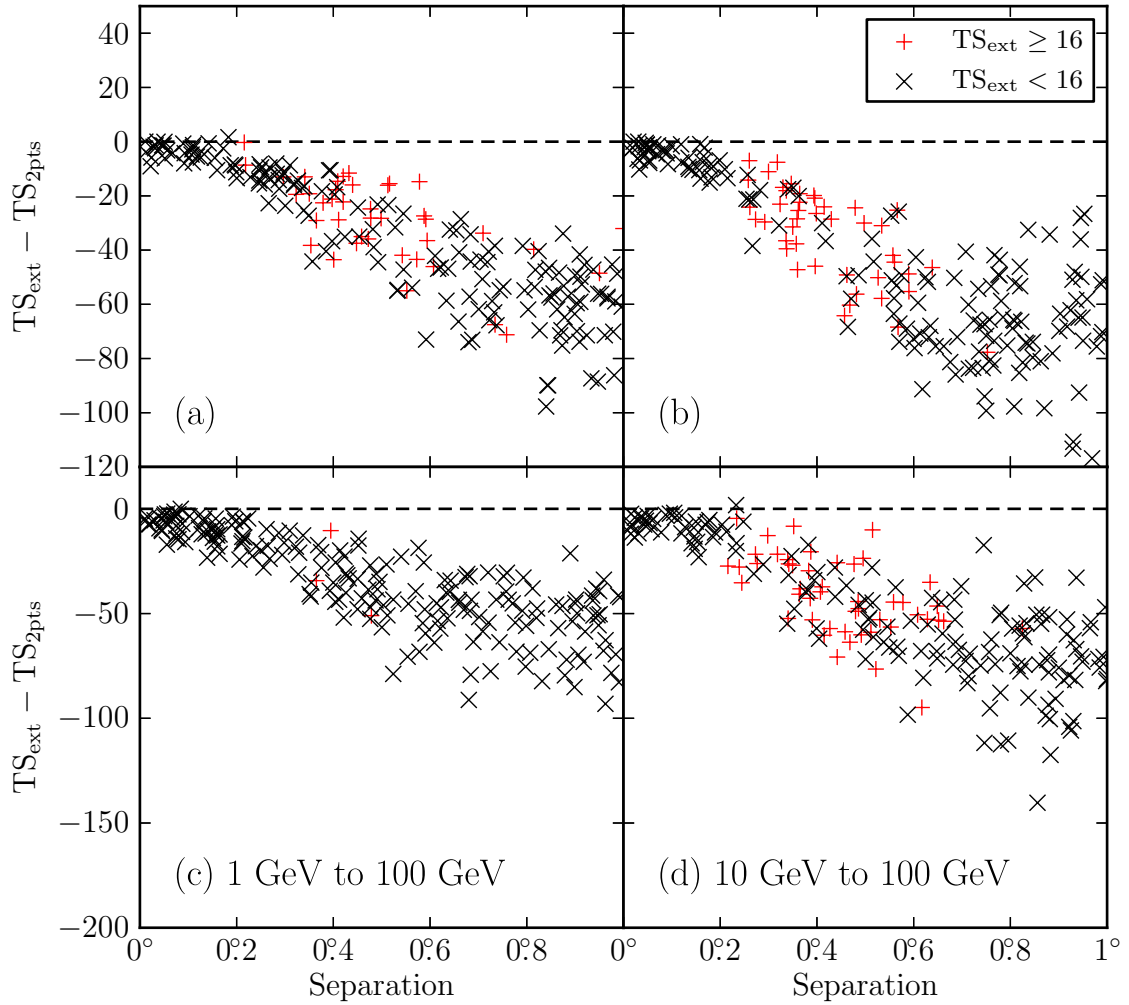


Figure 5.12 The distribution of $TS_{\text{ext}} - TS_{2\text{pts}}$ when fitting two simulated point-like sources of varying separations as both an extended source and as two point-like sources. (a), and (b) represent simulations of two point-like sources with the same spectral index and (c) and (d) represent simulations of two point-like sources with different spectral indices. (a) and (c) fit the simulated sources in the 1 GeV to 100 GeV energy range and (b) and (d) fit in the 10 GeV to 100 GeV energy range. The plus-shaped markers (colored red in the electronic version) are fits where $TS_{\text{ext}} \geq 16$.

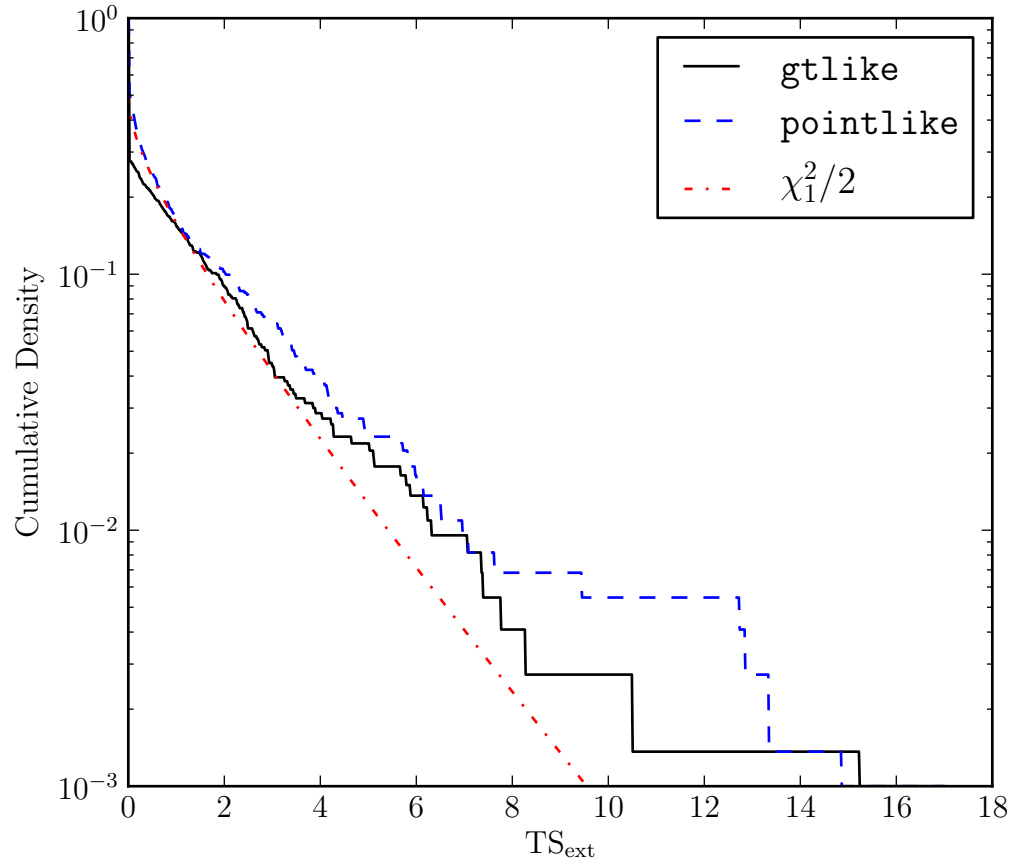


Figure 5.13 The cumulative density of TS_{ext} for the 733 clean AGN in 2LAC that were significant above 1 GeV calculated with `pointlike` (dashed line colored blue in the electronic version) and with `gtlike` (solid line colored black). AGN are too far and too small to be resolved by the LAT. Therefore, the cumulative density of TS_{ext} is expected to follow a $\chi^2_1/2$ distribution (Equation ??, the dash-dotted line colored red).

Table 5.3. Analysis of the twelve extended sources included in the 2FGL catalog

Name	GLON (deg.)	GLAT (deg.)	σ (deg.)	TS	TS _{ext}	Pos Err (deg.)	Flux ^(a)	Index
E>1 GeV								
SMC	302.59	-44.42	$1.32 \pm 0.15 \pm 0.31$	95.0	52.9	0.14	2.7 ± 0.3	2.48 ± 0.19
LMC	279.26	-32.31	$1.37 \pm 0.04 \pm 0.11$	1127.9	909.9	0.04	13.6 ± 0.6	2.43 ± 0.06
IC 443	189.05	3.04	$0.35 \pm 0.01 \pm 0.04$	10692.9	554.4	0.01	62.4 ± 1.1	2.22 ± 0.02
Vela X	263.34	-3.11	0.88					
Centaurus A	309.52	19.42	~ 10					
W28	6.50	-0.27	$0.42 \pm 0.02 \pm 0.05$	1330.8	163.8	0.01	56.5 ± 1.8	2.60 ± 0.03
W30	8.61	-0.20	$0.34 \pm 0.02 \pm 0.02$	464.8	76.0	0.02	29.1 ± 1.5	2.56 ± 0.05
W44	34.69	-0.39	$0.35 \pm 0.02 \pm 0.02$	1917.0	224.8	0.01	71.2 ± 0.5	2.66 ± 0.00
W51C	49.12	-0.45	$0.27 \pm 0.02 \pm 0.04$	1823.4	118.9	0.01	37.2 ± 1.3	2.34 ± 0.03
Cygnus Loop	74.21	-8.48	$1.71 \pm 0.05 \pm 0.06$	357.9	246.0	0.06	11.4 ± 0.7	2.50 ± 0.10
E>10 GeV								
MSH 15-52 ^(b)	320.39	-1.22	$0.21 \pm 0.04 \pm 0.04$	76.3	6.6	0.03	0.6 ± 0.1	2.20 ± 0.22
HESS J1825-137 ^(b)	17.56	-0.47	$0.65 \pm 0.04 \pm 0.02$	59.7	33.8	0.05	1.6 ± 0.2	1.63 ± 0.22

^(a) Integral Flux in units of 10^{-9} ph cm $^{-2}$ s $^{-1}$ and integrated in the fit energy range (either 1 GeV to 100 GeV or 10 GeV to 100 GeV).

^(b) The discrepancy in the best fit spectra of MSH 15-52 and HESS J1825-137 compared to Abdo et al. (2010a) and Grondin et al. (2011) is due to fitting over a different energy range.

Note. — All sources were fit using a radially-symmetric uniform disk spatial model. GLON and GLAT are Galactic longitude and latitude of the best fit extended source respectively. The first error on σ is statistical and the second is systematic (see Section ??). The errors on the integral fluxes and the spectral indices are statistical only. Pos Err is the error on the position of the source. Vela X and the Centaurus A Lobes were not fit in our analysis but are included for completeness.

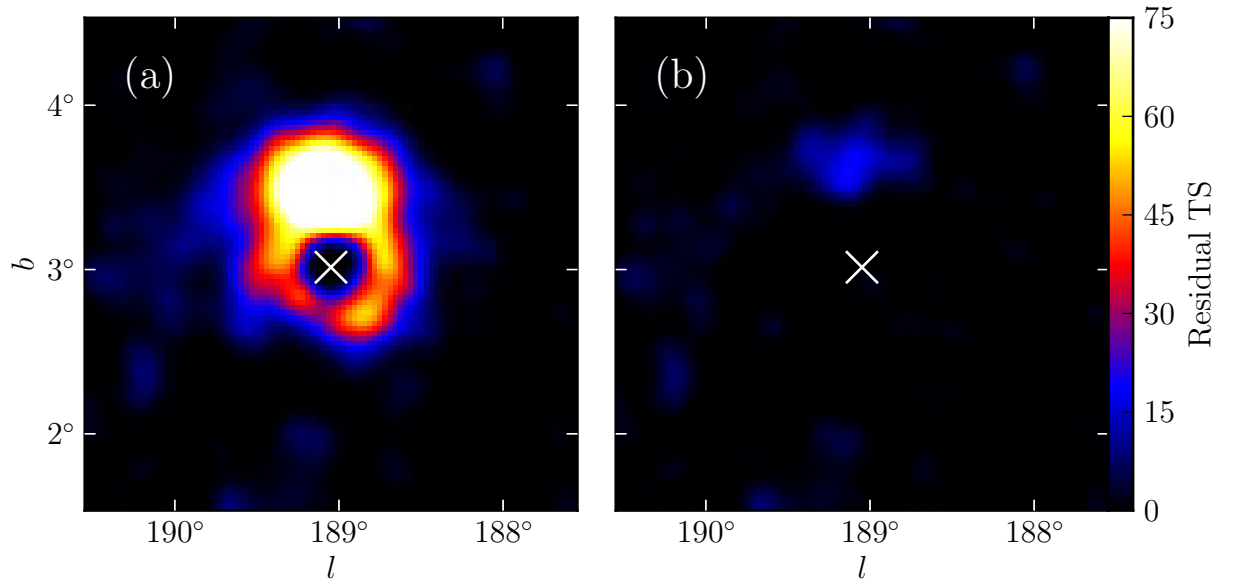


Figure 5.14 A TS map generated for the region around the SNR IC 443 using photons with energies between 1 GeV and 100 GeV. (a) TS map after subtracting IC 443 modeled as a point-like source. (b) same as (a), but IC 443 modeled as an extended source. The cross represents the best fit position of IC 443.

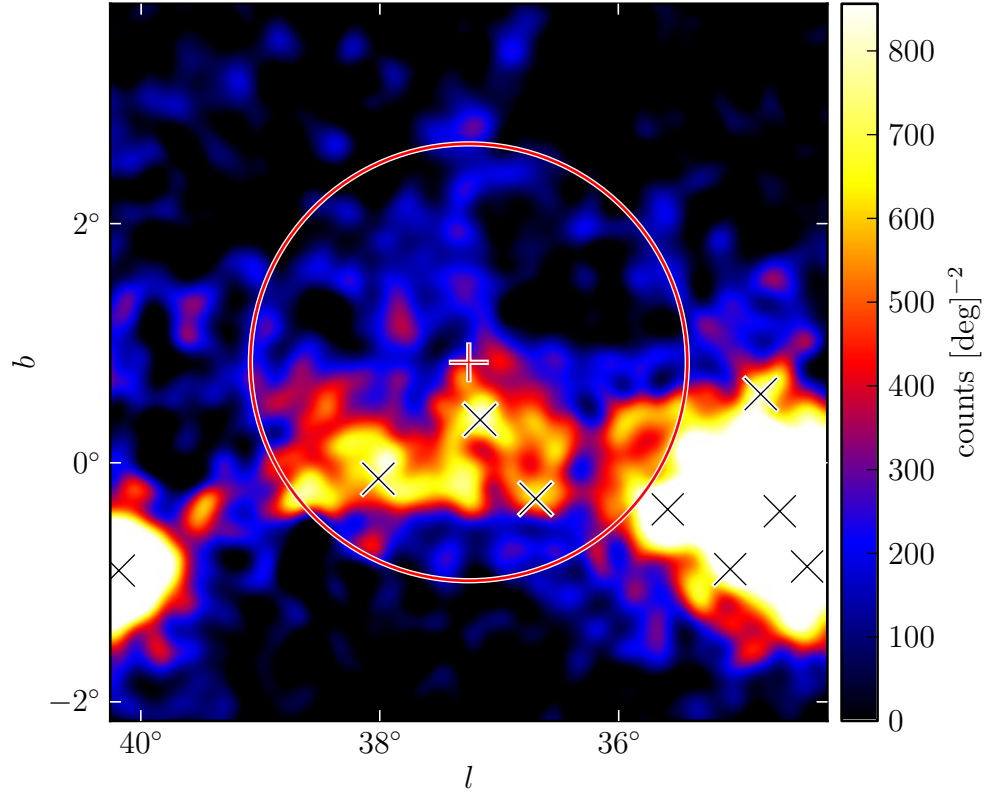


Figure 5.15 A diffuse-emission-subtracted 1 GeV to 100 GeV counts map of the region around 2FGL J1856.2+0450c smoothed by a 0.1° 2D Gaussian kernel. The plus-shaped marker and circle (colored red in the online version) represent the center and size of the source fit with a radially-symmetric uniform disk spatial model. The black crosses represent the positions of other 2FGL sources. The extension is statistically significant, but the extension encompasses many 2FGL sources and the emission does not look to be uniform. Although the fit is statistically significant, it likely corresponds to residual features of inaccurately modeled diffuse emission picked up by the fit.

Table 5.4. Extension fit for the nine additional extended sources

Name	GLON (deg.)	GLAT (deg.)	σ (deg.)	TS	TS _{ext}	Pos Err (deg.)	Flux ^(a)	Index	Counterpart
E>1 GeV									
2FGL J0823.0–4246	260.32	–3.28	$0.37 \pm 0.03 \pm 0.02$	322.2	48.0	0.02	8.4 ± 0.6	2.21 ± 0.09	Puppis A
2FGL J1627.0–2425c	353.07	16.80	$0.42 \pm 0.05 \pm 0.16$	139.9	32.4	0.04	6.3 ± 0.6	2.50 ± 0.14	Ophiuchus
E>10 GeV									
2FGL J0851.7–4635	266.31	–1.43	$1.15 \pm 0.08 \pm 0.02$	116.6	86.8	0.07	1.3 ± 0.2	1.74 ± 0.21	Vela Jr.
2FGL J1615.0–5051	332.37	–0.13	$0.32 \pm 0.04 \pm 0.01$	50.4	16.7	0.04	1.0 ± 0.2	2.19 ± 0.28	HESS J1616–508
2FGL J1615.2–5138	331.66	–0.66	$0.42 \pm 0.04 \pm 0.02$	76.1	46.5	0.04	1.1 ± 0.2	1.79 ± 0.26	HESS J1614–518
2FGL J1632.4–4753c	336.52	0.12	$0.35 \pm 0.04 \pm 0.02$	64.4	26.9	0.04	1.4 ± 0.2	2.66 ± 0.30	HESS J1632–478
2FGL J1712.4–3941 ^(b)	347.26	–0.53	$0.56 \pm 0.04 \pm 0.02$	59.4	38.5	0.05	1.2 ± 0.2	1.87 ± 0.22	RX J1713.7–3946
2FGL J1837.3–0700c	25.08	0.13	$0.33 \pm 0.07 \pm 0.05$	47.0	18.5	0.07	1.0 ± 0.2	1.65 ± 0.29	HESS J1837–069
2FGL J2021.5+4026	78.24	2.20	$0.63 \pm 0.05 \pm 0.04$	237.2	128.9	0.05	2.0 ± 0.2	2.42 ± 0.19	γ -Cygni

^(a) Integral Flux in units of 10^{-9} ph cm⁻²s⁻¹ and integrated in the fit energy range (either 1 GeV to 100 GeV or 10 GeV to 100 GeV).

^(b) The discrepancy in the best fit spectra of 2FGL J1712.4–3941 compared to Abdo et al. (2011) is due to fitting over a different energy range.

Note. — The columns in this table have the same meaning as those in Table ?? RX J1713.7–3946 and Vela Jr. were previously studied in dedicated publications (Abdo et al. 2011; Tanaka et al. 2011).

Table 5.5. Dual localization, alternative PSF, and alternative approach to modeling the diffuse emission

Name	TS _{pointlike}	TS _{gtlike}	TS _{alt,diff}	TS _{ext,pointlike}	TS _{ext,gtlike}	TS _{extalt,diff}	σ (deg.)	$\sigma_{\text{alt,diff}}$ (deg.)	$\sigma_{\text{alt,psf}}$ (deg.)	TS _{2pts}
E>1 GeV										
2FGL J0823.0–4246	331.9	322.2	356.0	60.0	48.0	56.0	0.37	0.39	0.39	23.0
2FGL J1627.0–2425c	154.8	139.9	105.7	39.4	32.4	24.8	0.42	0.40	0.58	24.5
E>10 GeV										
2FGL J0851.7–4635	115.2	116.6	123.1	83.9	86.8	89.8	1.15	1.16	1.17	15.5
2FGL J1615.0–5051 ^(a)	48.2	50.4	56.6	15.2	16.7	17.8	0.32	0.33	0.32	13.1
2FGL J1615.2–5138	75.0	76.1	83.8	42.9	46.5	54.1	0.42	0.43	0.43	35.1
2FGL J1632.4–4753c	64.5	64.4	66.8	23.0	26.9	25.5	0.35	0.36	0.37	10.9
2FGL J1712.4–3941	59.8	59.4	39.9	38.4	38.5	30.7	0.56	0.55	0.53	2.7
2FGL J1837.3–0700c	44.5	47.0	39.2	17.6	18.5	16.1	0.33	0.32	0.38	10.8
2FGL J2021.5+4026	239.1	237.2	255.8	139.1	128.9	138.0	0.63	0.65	0.59	37.3

^(a) Using **pointlike**, TS_{ext} for 2FGL J1615.0–5051 was slightly below 16 when the source was fit in the 10 GeV to 100 GeV energy range. To confirm the extension measure, the extension was refit in **pointlike** using a slightly lower energy. In the 5.6 GeV to 100 GeV energy range, we obtained a consistent extension and TS_{ext} = 28.0. In the rest of this paper, we quote the $E > 10\text{GeV}$ results for consistency with the other sources.

Note. — TS_{pointlike}, TS_{gtlike}, and TS_{alt,diff} are the test statistic values from **pointlike**, **gtlike**, and **gtlike** with the alternative approach to modeling the diffuse emission respectively. TS_{ext,pointlike}, TS_{ext,gtlike}, and TS_{extalt,diff} are the TS values from **pointlike**, **gtlike**, and **gtlike** with the alternative approach to modeling the diffuse emission respectively. σ , $\sigma_{\text{alt,diff}}$, and $\sigma_{\text{alt,psf}}$ are the fit sizes assuming a radially-symmetric uniform disk model with the standard analysis, the alternative approach to modeling the diffuse emission, and the alternative PSF respectively.

Table 5.6. Nearby Residual-induced Sources

Extended Source	Residual-induced Sources
2FGL J0823.0–4246	2FGL J0821.0–4254, 2FGL J0823.4–4305
2FGL J1627.0–2425c	...
2FGL J0851.7–4635	2FGL J0848.5–4535, 2FGL J0853.5–4711, 2FGL J0855.4–4625
2FGL J1615.0–5051	...
2FGL J1615.2–5138	2FGL J1614.9–5212
2FGL J1632.4–4753c	2FGL J1634.4–4743c
2FGL J1712.4–3941	...
2FGL J1837.3–0700c	2FGL J1835.5–0649
2FGL J2021.5+4026	2FGL J2019.1+4040

Note. — For each new extended source, we list nearby 2FGL sources that we have concluded here correspond to residuals induced by not modeling the extensions of nearby extended sources.

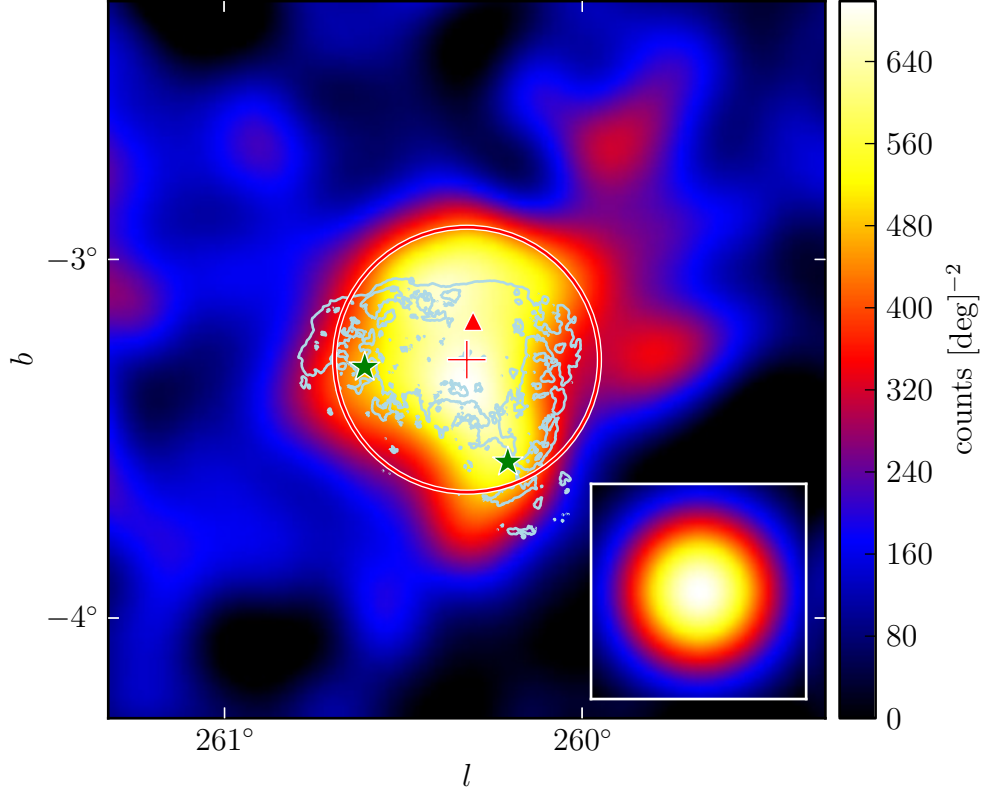


Figure 5.16 A diffuse-emission-subtracted 1 GeV to 100 GeV counts map of 2FGL J0823.0–4246 smoothed by a 0.1° 2D Gaussian kernel. The triangular marker (colored red in the online version) represents the 2FGL position of this source. The plus-shaped marker and the circle (colored red) represent the best fit position and extension of this source assuming a radially-symmetric uniform disk model. The two star-shaped markers (colored green) represent 2FGL sources that were removed from the background model. From left to right, these sources are 2FGL J0823.4–4305 and 2FGL J0821.0–4254. The lower right inset is the model predicted emission from a point-like source with the same spectrum as 2FGL J0823.4–4305 smoothed by the same kernel. This source is spatially coincident with the Puppis A SNR. The light blue contours correspond to the X-ray image of Puppis A observed by *ROSAT* (Petre et al. 1996).

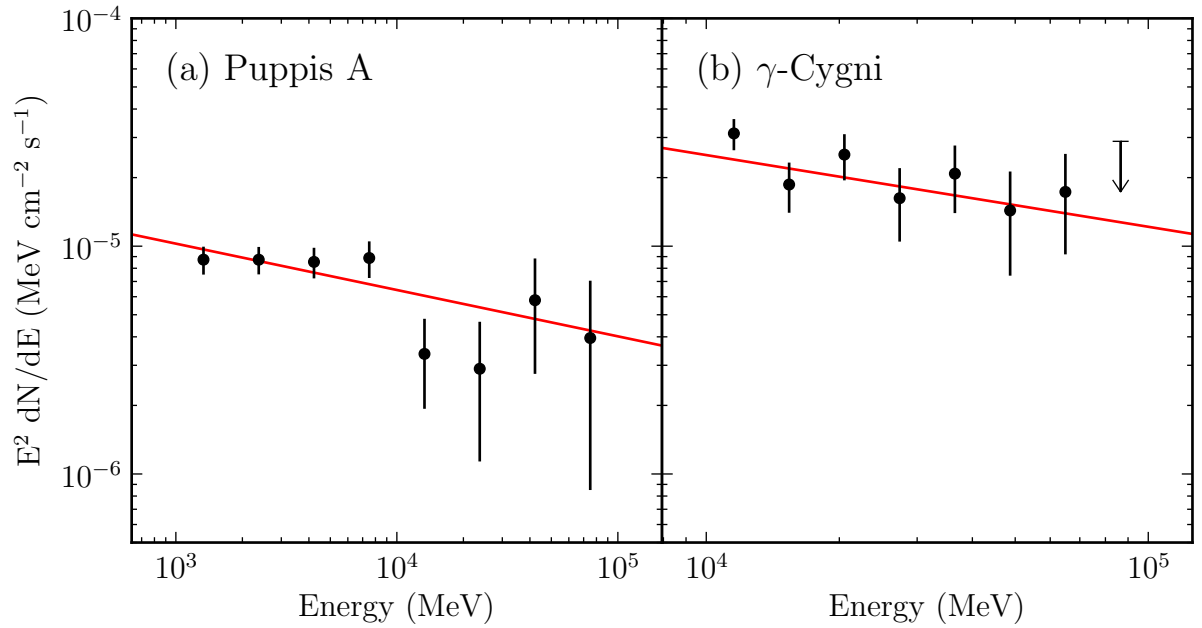


Figure 5.17 The spectral energy distribution of the extended sources Puppis A (2FGL J0823.0–4246) and γ -Cygni (2FGL J2021.5+4026). The lines (colored red in the online version) are the best fit power-law spectral models of these sources. Puppis A has a spectral index of 2.21 ± 0.09 and γ -Cygni has an index of 2.42 ± 0.19 . The spectral errors are statistical only. The upper limit is at the 95% confidence level.

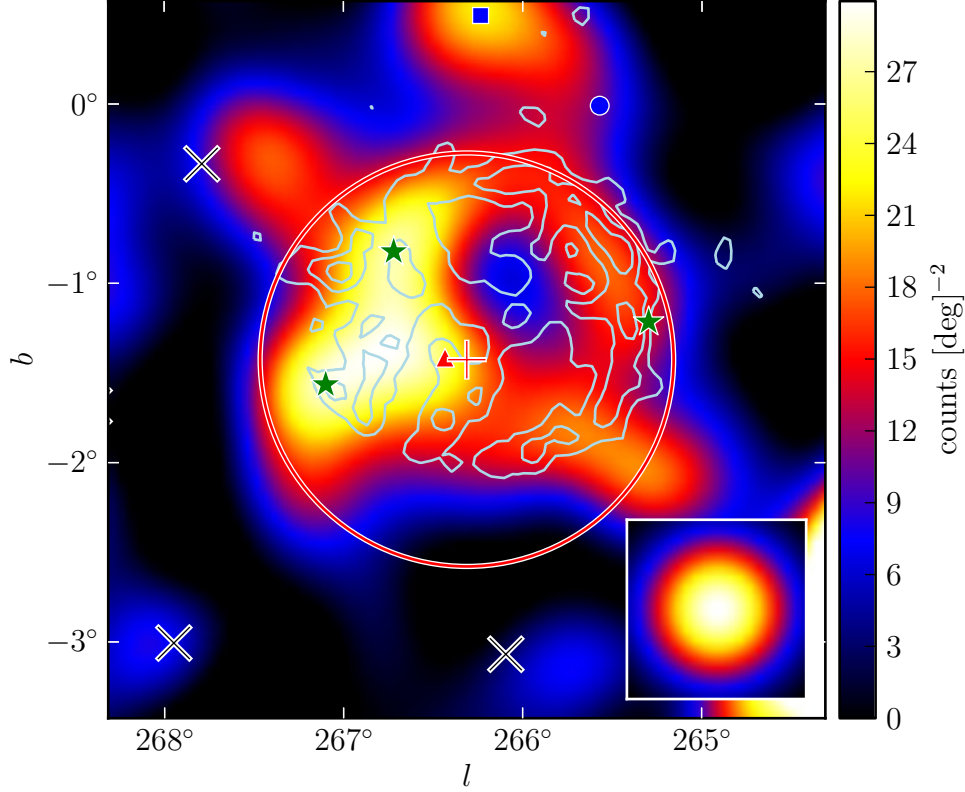


Figure 5.18 A diffuse-emission-subtracted 10 GeV to 100 GeV counts map of 2FGL J0851.7–4635 smoothed by a 0.25° 2D Gaussian kernel. The triangular marker (colored red in the electronic version) represents the 2FGL position of this source. The plus-shaped marker and the circle (colored red) are the best fit position and extension of this source assuming a radially-symmetric uniform disk model. The three black crosses represent background 2FGL sources. The three star-shaped markers (colored green) represent other 2FGL sources that were removed from the background model. They are (from left to right) 2FGL J0853.5–4711, 2FGL J0855.4–4625, and 2FGL J0848.5–4535. The circular and square-shaped marker (colored blue) represents the 2FGL and relocalized position of another 2FGL source. This extended source is spatially coincident with the Vela Jr. SNR. The contours (colored light blue) correspond to the TeV image of Vela Jr. (Aharonian et al. 2007a).

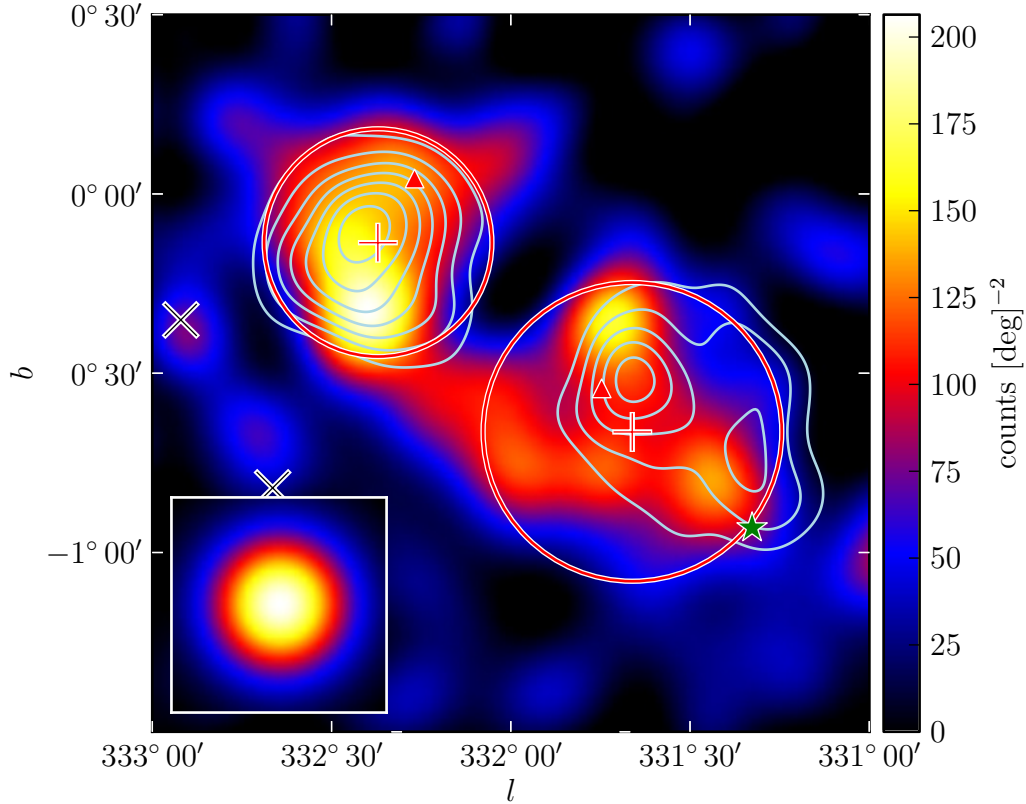


Figure 5.19 A diffuse-emission-subtracted 10 GeV to 100 GeV counts map of 2FGL J1615.0–5051 (upper left) and 2FGL J1615.2–5138 (lower right) smoothed by a 0.1° 2D Gaussian kernel. The triangular markers (colored red in the electronic version) represent the 2FGL positions of these sources. The cross-shaped markers and the circles (colored red) represent the best fit positions and extensions of these sources assuming a radially symmetric uniform disk model. The two black crosses represent background 2FGL sources and the star-shaped marker (colored green) represents 2FGL J1614.9-5212, another 2FGL source that was removed from the background model. The contours (colored light blue) correspond to the TeV image of HESS J1616–508 (left) and HESS J1614–518 (right) (Aharonian et al. 2006d).

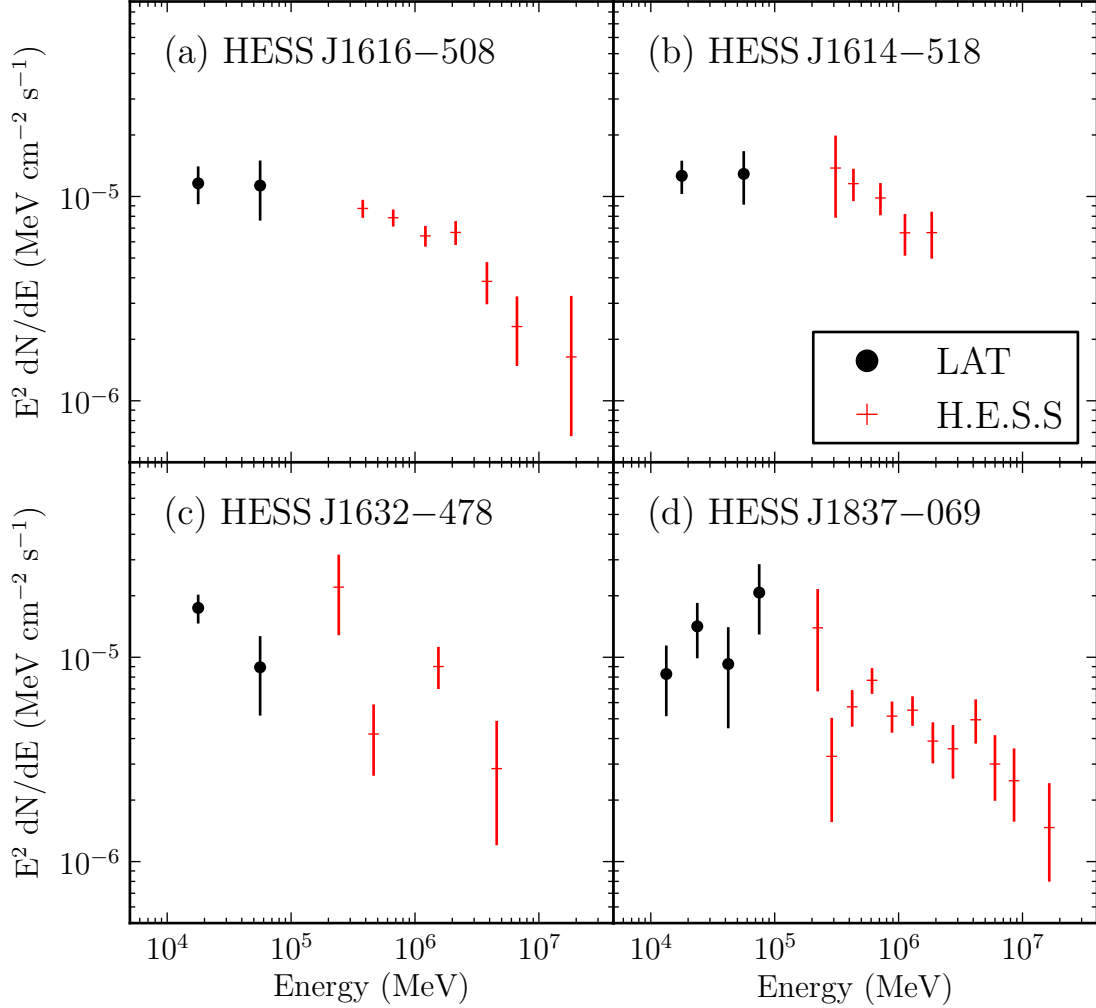


Figure 5.20 The spectral energy distribution of four extended sources associated with unidentified extended TeV sources. The black points with circular markers are obtained by the LAT. The points with plus-shaped markers (colored red in the electronic version) are for the associated H.E.S.S. sources. (a) the LAT SED of 2FGL J1615.0–5051 together with the H.E.S.S. SED of HESS J1616–508. (b) 2FGL J1615.2–5138 and HESS J1614–518. (c) 2FGL J1632.4–4753c and HESS J1632–478. (d) 2FGL J1837.3–0700c and HESS J1837–069. The H.E.S.S. data points are from (Aharonian et al. 2006d). Both LAT and H.E.S.S. spectral errors are statistical only.

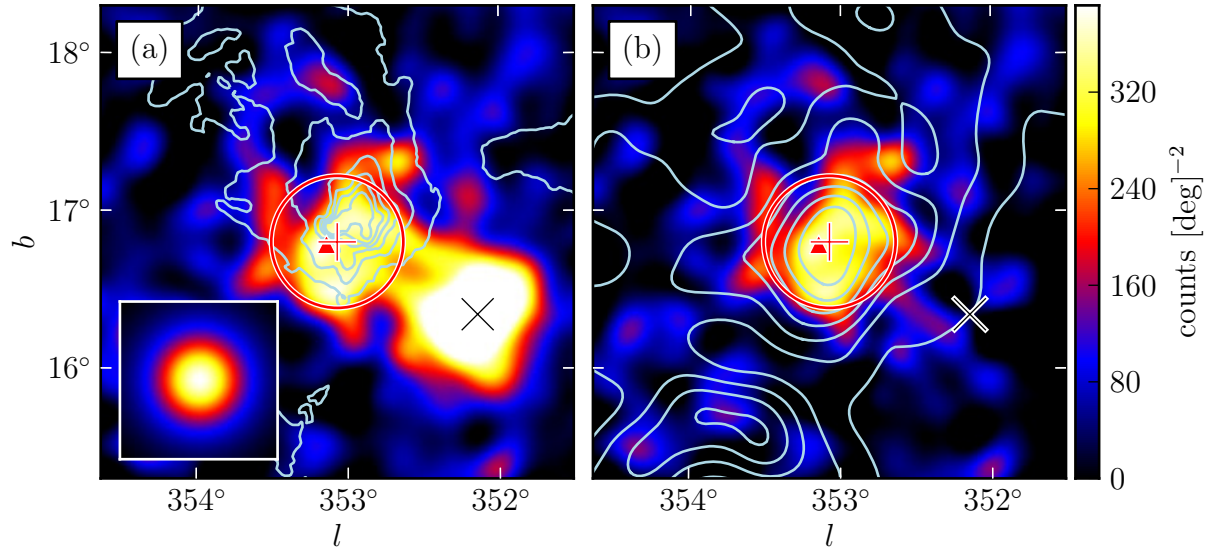


Figure 5.21 A diffuse-emission-subtracted 1 GeV to 100 GeV counts map of (a) the region around 2FGL J1627.0–2425 smoothed by a 0.1° 2D Gaussian kernel and (b) with the emission from 2FGL J1625.7–2526 subtracted. The triangular marker (colored red in the online version) represents the 2FGL position of this source. The plus-shaped marker and the circle (colored red) represent the best fit position and extension of this source assuming a radially-symmetric uniform disk model and the black cross represents a background 2FGL source. The contours in (a) correspond to the $100\ \mu\text{m}$ image observed by IRAS (Young et al. 1986). The contours in (b) correspond to CO ($J = 1 \rightarrow 0$) emission integrated from $-8\ \text{km s}^{-1}$ to $20\ \text{km s}^{-1}$. They are from de Geus et al. (1990), were cleaned using the moment-masking technique (Dame 2011), and have been smoothed by a 0.25° 2D Gaussian kernel.

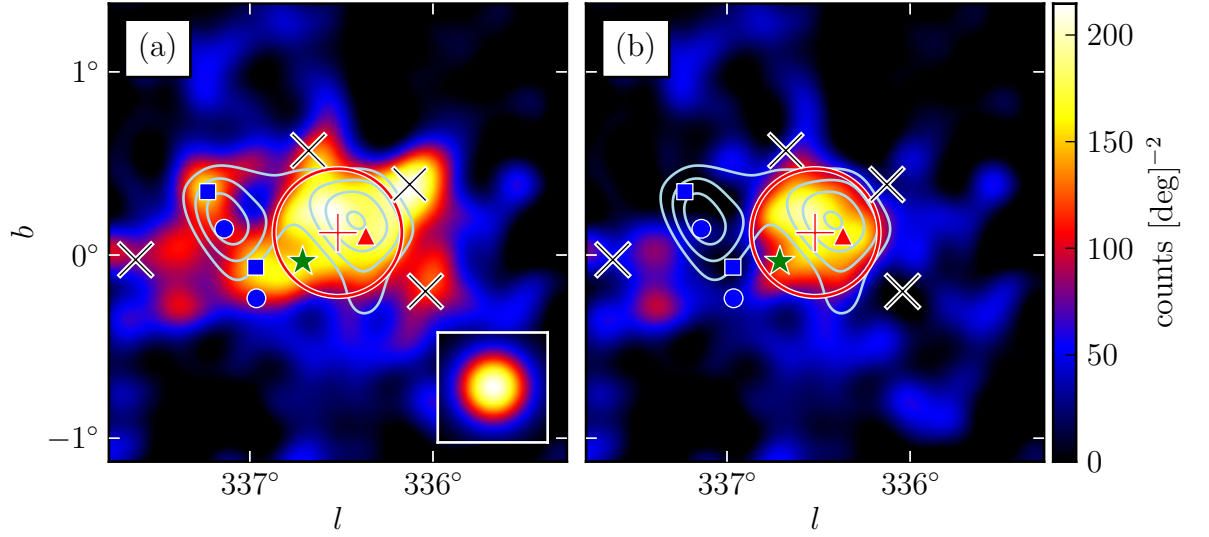


Figure 5.22 A diffuse-emission-subtracted 10 GeV to 100 GeV counts map of 2FGL J1632.4–4753c (a) smoothed by a 0.1 2D Gaussian kernel and (b) with the emission from the background sources subtracted. The triangular marker (colored red in the electronic version) represents the 2FGL position of this source. The plus-shaped marker and the circle (colored red) are the best fit position and extension of 2FGL J1632.4–4753c assuming a radially-symmetric uniform disk model. The four black crosses represent background 2FGL sources subtracted in (b). The circular and square-shaped markers (colored blue) represent the 2FGL and relocalized positions respectively of two additional background 2FGL sources subtracted in (b). The star-shaped marker (colored green) represents 2FGL J1634.4–4743c, another 2FGL source that was removed from the background model. The contours (colored light blue) correspond to the TeV image of HESS J1632–478 (Aharonian et al. 2006d).

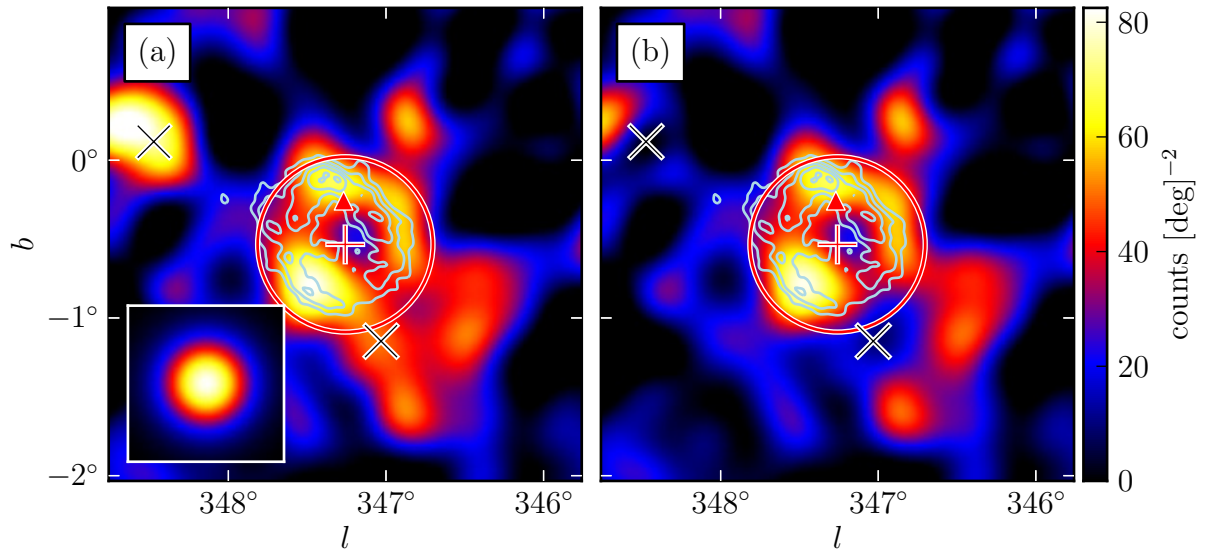


Figure 5.23 A diffuse-emission-subtracted 10 GeV to 100 GeV counts map of 2FGL J1712.4–3941 (a) smoothed by a 0.15° 2D Gaussian kernel and (b) with the emission from the background sources subtracted. This source is spatially coincident with RX J1713.7–3946 and was recently studied in Abdo et al. (2011). The triangular marker (colored red in the online version) represents the 2FGL position of this source. The plus-shaped marker and the circle (colored red) are the best fit position and extension of this source assuming a radially symmetric uniform disk model. The two black crosses represent background 2FGL sources subtracted in (b). The contours (colored light blue) correspond to the TeV image (Aharonian et al. 2007b).

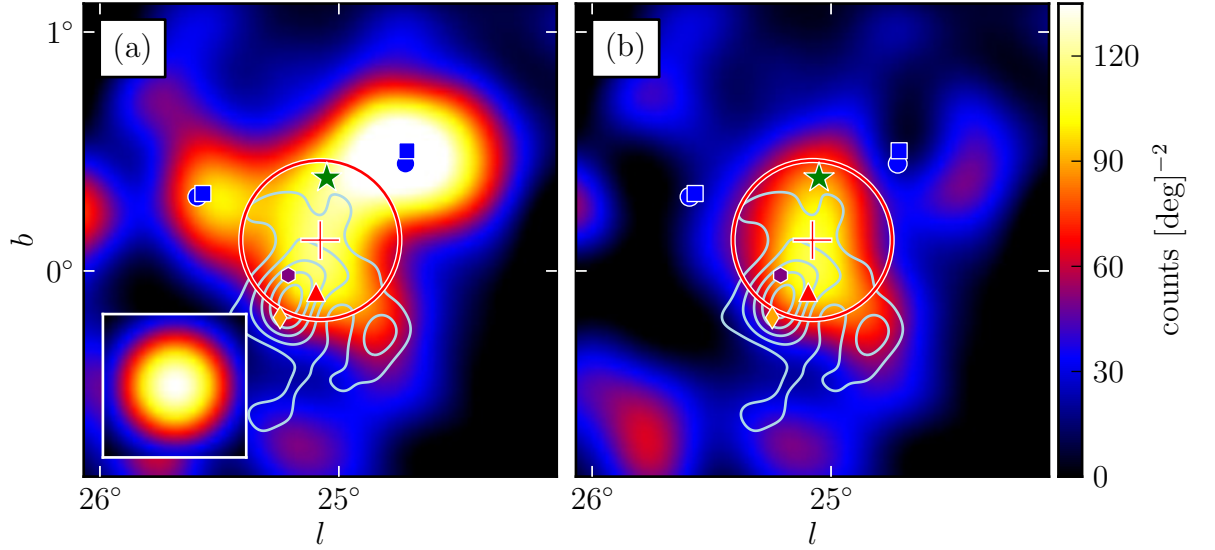


Figure 5.24 A diffuse-emission-subtracted 10 GeV to 100 GeV counts map of the region around 2FGL J1837.3–0700c (a) smoothed by a 0.15° 2D Gaussian kernel and (b) with the emission from the background sources subtracted. The triangular marker (colored red in the online version) represents the 2FGL position of this source. The plus-shaped marker and the circle (colored red) represent the best fit position and extension of 2FGL J1837.3–0700c assuming a radially-symmetric uniform disk model. The circular and square-shaped markers (colored blue) represent the 2FGL and the relocalized positions respectively of two background 2FGL sources subtracted in (b). The star-shaped marker (colored green) represents 2FGL J1835.5–0649, another 2FGL source that was removed from the background model. The contours (colored light blue) correspond to the TeV image of HESS J1837–069 (Aharonian et al. 2006d). The diamond-shaped marker (colored orange) represents the position of PSR J1838–0655 and the hexagonal-shaped marker (colored purple) represents the position AX J1837.3–0652 (Gotthelf & Halpern 2008).

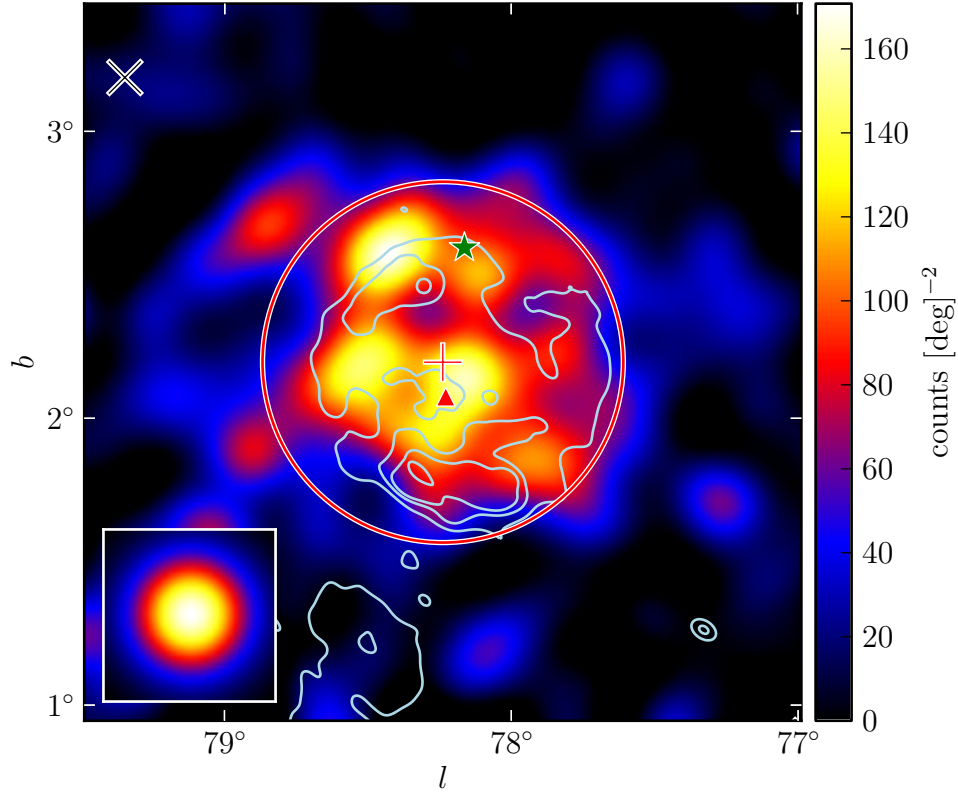


Figure 5.25 A diffuse-emission-subtracted 10 GeV to 100 GeV counts map of the region around 2FGL J2021.5+4026 smoothed by a 0.1° 2D Gaussian kernel. The triangular marker (colored red in the online version) represents the 2FGL position of this source. The plus-shaped marker and the circle (colored red) represent the best fit position and extension of 2FGL J2021.5+4026 assuming a radially-symmetric uniform disk model. The star-shaped marker (colored green) represents 2FGL J2019.1+4040, a 2FGL source that was removed from the background model. 2FGL J2021.5+4026 is spatially coincident with the γ -Cygni SNR. The contours (colored light blue) correspond to the 408MHz image of γ -Cygni observed by the Canadian Galactic Plane Survey (Taylor et al. 2003).

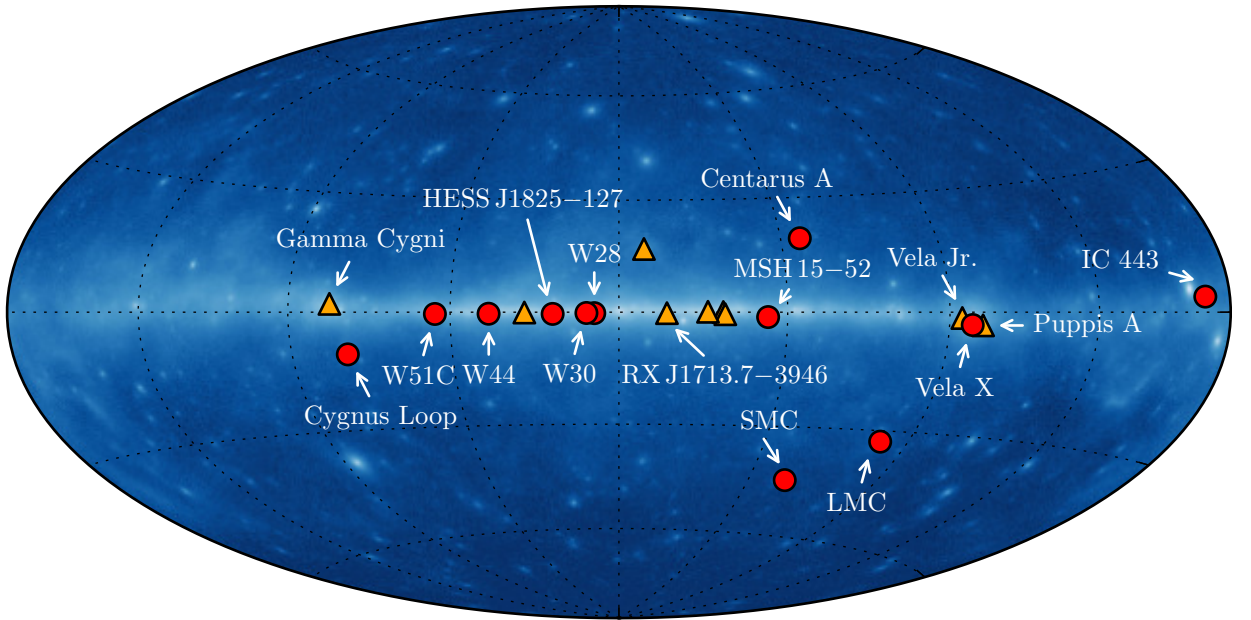


Figure 5.26 The 21 spatially extended sources detected by the LAT at GeV energies with 2 years of data. The twelve extended sources included in 2FGL are represented by the circular markers (colored red in the online version). The nine new extended sources are represented by the triangular markers (colored orange). The source positions are overlaid on a 100 MeV to 100 GeV Aitoff projection sky map of the LAT data in Galactic coordinates.

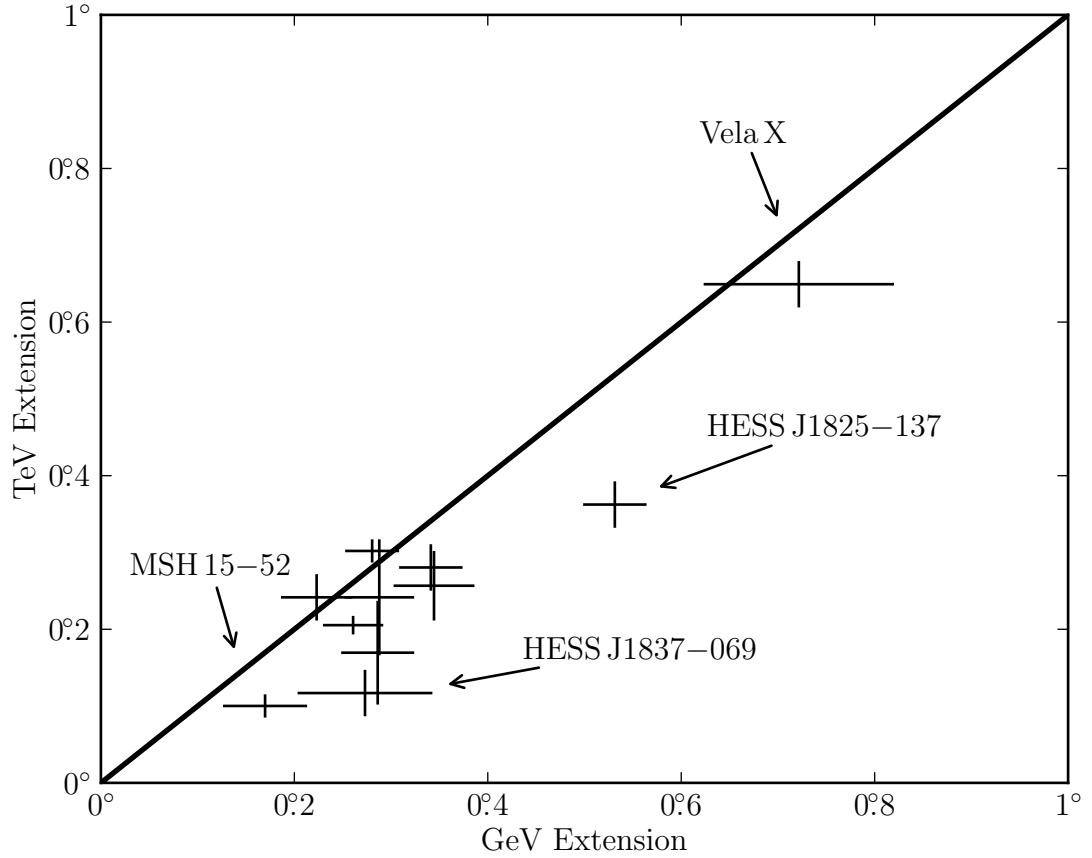


Figure 5.27 A comparison of the sizes of extended sources detected at both GeV and TeV energies. The TeV sizes of W30, 2FGL J1837.3–0700c, 2FGL J1632.4–4753c, 2FGL J1615.0–5051, and 2FGL J1615.2–5138 are from Aharonian et al. (2006d). The TeV sizes of MSH 15–52, HESS J1825–137, Vela X, Vela Jr., RX J1713.7–3946 and W28 are from Aharonian et al. (2005, 2006b,c, 2007a,b, 2008). The TeV size of IC 443 is from Acciari et al. (2009) and W51C is from Krause et al. (2011). The TeV sizes of MSH 15–52, HESS J1614–518, HESS J1632–478, and HESS J1837–069 have only been reported with an elliptical 2D Gaussian fit and so the plotted sizes are the geometric mean of the semi-major and semi-minor axis. The LAT extension of Vela X is from Abdo et al. (2010). The TeV sources were fit assuming a 2D Gaussian surface brightness profile so the plotted GeV and TeV extensions were first converted to r_{68} (see Section ??). Because of their large sizes, the shape of RX J1713.7–3946 and Vela Jr. were not directly fit at TeV energies and so are not included in this comparison. On the other hand, dedicated publications by the LAT collaboration on these sources showed that their morphologies are consistent (Abdo et al. 2011; Tanaka et al. 2011). The LAT extension errors are the statistical and systematic errors added in quadrature.

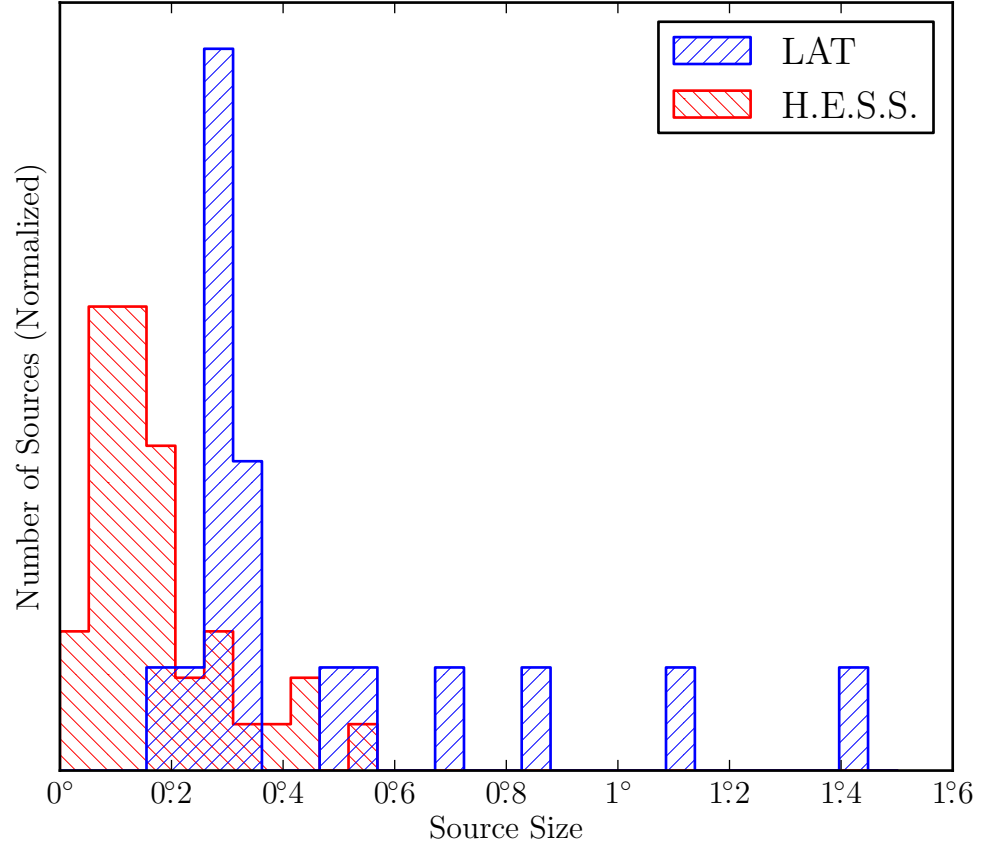


Figure 5.28 The distributions of the sizes of 18 extended LAT sources at GeV energies (colored blue in the electronic version) and the sizes of the 40 extended H.E.S.S. sources at TeV energies (colored red). The H.E.S.S. sources were fit with a 2D Gaussian surface brightness profile so the LAT and H.E.S.S. sizes were first converted to r_{68} . The GeV size of Vela X is taken from Abdo et al. (2010). Because of their large sizes, the shape of RX J1713.7–3946 and Vela Jr. were not directly fit at TeV energies and are not included in this comparison. Centaurus A is not included because of its large size.

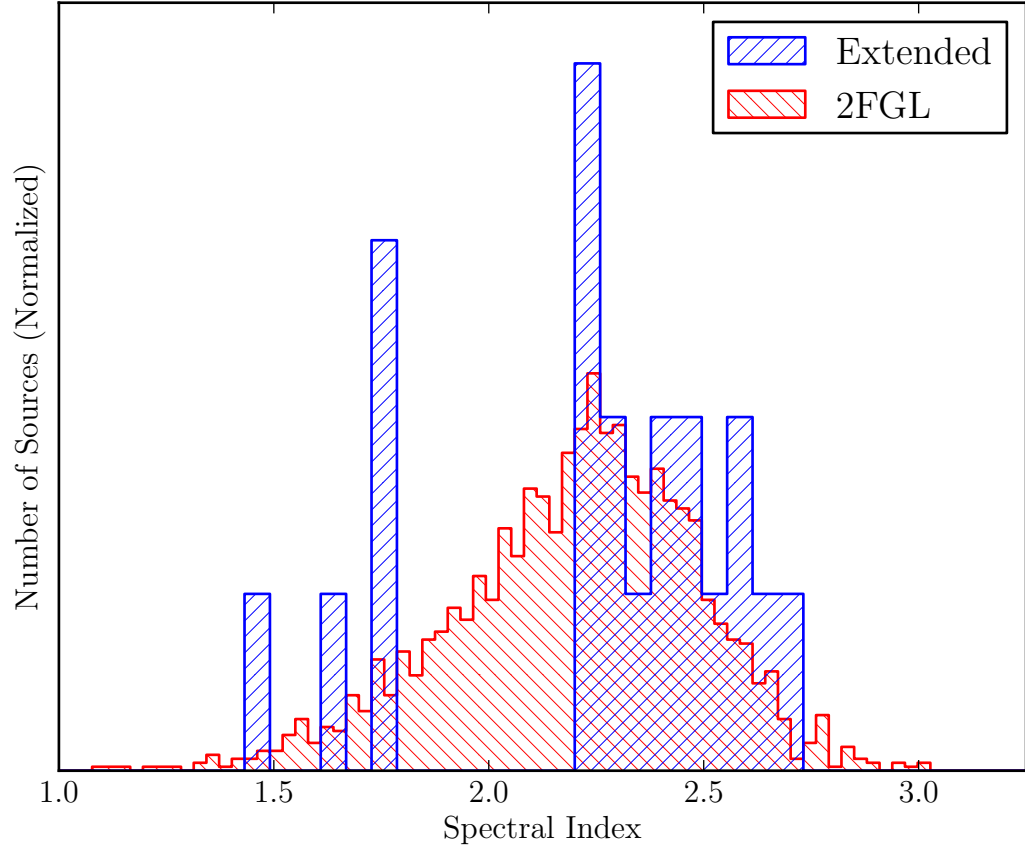


Figure 5.29 The distribution of spectral indices of the 1873 2FGL sources (colored red in the electronic version) and the 21 spatially extended sources (colored blue). The index of Centaurus A is taken from Nolan et al. (2012) and the index of Vela X is taken from Abdo et al. (2010).

Chapter 6

Search for Pulsar Wind Nebulae associated with Gamma-loud Pulsars

This chapter is based on work from 2PC. GET REFERENCE HERE.

6.1 Off-peak Phase Selection

6.2 Off-peak Analysis Method

6.3 Off-peak Results

6.4 Off-Peak Individual Source Discussion

Chapter 7

Search for Pulsar Wind Nebulae associated with TeV Pulsars

Notes

- Only include sources classified as PWN in TeVCat.
- Always model LAT Pulsar in the background (???)

7.1 List of Candidates

7.2 Analysis Method

7.3 Sources Detected

Chapter 8

Search for Pulsar Wind Nebulae associated with High \dot{E} Pulsars

Chapter 9

Population Study of The Large Area Telescope (LAT)-detected Pulsar wind nebula (PWN)

Chapter 10

Future Work (or Outlook)??

What would make good future work. Something about CTA population study, something about improved modeling liek HESS J1825, something about better PSF

Bibliography

- Abdo, A. A., Ackermann, M., Ajello, M., et al. 2009a, ApJ, 706, L1
- . 2009b, Astroparticle Physics, 32, 193
- . 2010a, ApJ, 714, 927
- Abdo, A. A., Ackermann, M., Ajello, M., et al. 2010b, A&A, 523, A46
- Abdo, A. A., Ackermann, M., Ajello, M., et al. 2010c, Science, 328, 725
- . 2010d, ApJS, 188, 405
- . 2010e, ApJ, 708, 1254
- . 2010f, ApJ, 718, 348
- Abdo, A. A., Ackermann, M., Ajello, M., et al. 2010, The Astrophysical Journal, 713, 146
- Abdo, A. A., Ackermann, M., Ajello, M., et al. 2010a, Science, 327, 1103
- . 2010b, ApJ, 712, 459
- Abdo, A. A., Ackermann, M., Ajello, M., et al. 2010c, A&A, 512, A7
- Abdo, A. A., Ackermann, M., Ajello, M., et al. 2010d, ApJS, 187, 460
- . 2011, ApJ, 734, 28
- Acciari, V. A., Aliu, E., Arlen, T., et al. 2009, ApJ, 698, L133

—. 2011, *ApJ*, 738, 3

Ackermann, M., Ajello, M., Allafort, A., et al. 2011, *ApJ*, 743, 171

Ackermann, M., Ajello, M., Albert, A., et al. 2012, *ApJS*, 203, 4

Aharonian, F., Akhperjanian, A. G., Aye, K.-M., et al. 2005, *A&A*, 435, L17

Aharonian, F., Akhperjanian, A. G., Bazer-Bachi, A. R., et al. 2006a, *A&A*, 460, 743

—. 2006b, *A&A*, 460, 365

—. 2006c, *A&A*, 448, L43

—. 2006d, *ApJ*, 636, 777

—. 2007a, *ApJ*, 661, 236

—. 2007b, *A&A*, 464, 235

—. 2008, *A&A*, 481, 401

Aharonian, F. A., & Bogovalov, S. V. 2003, *New A*, 8, 85

Aharonian, F. A., Coppi, P. S., & Voelk, H. J. 1994, *ApJ*, 423, L5

Aharonian, F. A., Akhperjanian, A. G., Bazer-Bachi, A. R., et al. 2007c, *A&A*, 469, L1

Ajello, M., Allafort, A., Baldini, L., et al. 2012, *ApJ*, 744, 80

Akaike, H. 1974, *IEEE Transactions on Automatic Control*, 19, 716

Albert, J., Aliu, E., Anderhub, H., et al. 2006, *Science*, 312, 1771

Arnold, J. R., Metzger, A. E., Anderson, E. C., & van Dilla, M. A. 1962, *J. Geophys. Res.*, 67, 4878

Arons, J. 1996, *Space Sci. Rev.*, 75, 235

- Ashworth, William B., J. 1981, Proceedings of the American Philosophical Society, 125, pp. 52
- Atwood, W. B., Abdo, A. A., Ackermann, M., et al. 2009, ApJ, 697, 1071
- Baltz, E. A., Berenji, B., Bertone, G., et al. 2008, J. Cosmology Astropart. Phys., 7, 13
- Baum, W. A., Johnson, F. S., Oberly, J. J., et al. 1946, Phys. Rev., 70, 781
- Bertsch, D. L., Brazier, K. T. S., Fichtel, C. E., et al. 1992, Nature, 357, 306
- Bignami, G. F., Boella, G., Burger, J. J., et al. 1975, Space Science Instrumentation, 1, 245
- Blandford, R. D., & Romani, R. W. 1988, MNRAS, 234, 57P
- Blumenthal, G. R., & Gould, R. J. 1970, Rev. Mod. Phys., 42, 237
- Bogovalov, S. V., & Aharonian, F. A. 2000, MNRAS, 313, 504
- Bradt, H., Rappaport, S., & Mayer, W. 1969, Nature, 222, 728
- Browning, R., Ramsden, D., & Wright, P. J. 1971, Nature Physical Science, 232, 99
- Burnham, K. P., & Anderson, D. R. 2002, Model selection and multimodel inference: a practical information-theoretic approach, 2nd edn. (Springer)
- Burnight, T. 1949, Phys. Rev, 76, 19
- Caballero, I., & Wilms, J. 2012, Mem. Soc. Astron. Italiana, 83, 230
- Carroll, B. W., & Ostlie, D. A. 2006, An Introduction to Modern Astrophysics, 2nd edn. (Benjamin Cummings)
- Cash, W. 1979, ApJ, 228, 939
- Chandrasekhar, S. 1931, ApJ, 74, 81

- Cocke, W. J., Disney, M. J., & Taylor, D. J. 1969, *Nature*, 221, 525
- Critchfield, C. L., Ney, E. P., & Oleksa, S. 1952, *Physical Review*, 85, 461
- Dame, T. M. 2011, ArXiv e-prints
- de Geus, E. J., Bronfman, L., & Thaddeus, P. 1990, *A&A*, 231, 137
- Demorest, P. B., Pennucci, T., Ransom, S. M., Roberts, M. S. E., & Hessels, J. W. T. 2010, *Nature*, 467, 1081
- Eadie, W. T., Drijard, D., & James, F. E. 1971, *Statistical methods in experimental physics* (North-Holland Pub. Co.)
- Espinoza, C. M., Lyne, A. G., Kramer, M., Manchester, R. N., & Kaspi, V. M. 2011, *ApJ*, 741, L13
- Esposito, J. A., Bertsch, D. L., Chen, A. W., et al. 1999, *ApJS*, 123, 203
- Falanga, M., Kuiper, L., Poutanen, J., et al. 2005, *A&A*, 444, 15
- Feenberg, E., & Primakoff, H. 1948, *Phys. Rev.*, 73, 449
- Fichtel, C. E., Hartman, R. C., Kniffen, D. A., et al. 1975, *ApJ*, 198, 163
- Fisher, R. A. 1925, *Statistical Methods for Research Workers* (Edinburgh: Oliver and Boyd)
- Fritz, G., Henry, R. C., Meekins, J. F., Chubb, T. A., & Friedman, H. 1969, *Science*, 164, 709
- Gaensler, B. M., & Slane, P. O. 2006, *ARA&A*, 44, 17
- Gelfand, J. D., Slane, P. O., & Zhang, W. 2009, *ApJ*, 703, 2051
- Giordano, F., & Fermi LAT Collaboration. 2011, in *High-Energy Emission from Pulsars and their Systems*, ed. D. F. Torres & N. Rea, 69
- Gold, T. 1968, *Nature*, 218, 731

- Goldreich, P., & Julian, W. H. 1969, *ApJ*, 157, 869
- Górski, K. M., Hivon, E., Banday, A. J., et al. 2005, *ApJ*, 622, 759
- Gotthelf, E. V., & Halpern, J. P. 2008, *ApJ*, 681, 515
- Grondin, M.-H., Funk, S., Lemoine-Goumard, M., et al. 2011, *ApJ*, 738, 42
- Gunn, J. E., & Ostriker, J. P. 1969, *Nature*, 221, 454
- Hartman, R. C., Bertsch, D. L., Bloom, S. D., et al. 1999, *ApJS*, 123, 79
- Haug, E. 1975, *Zeitschrift Naturforschung Teil A*, 30, 1099
- Hayakawa, S. 1952, *Progress of Theoretical Physics*, 8, 571
- Herschel, W. 1800, *Philosophical Transactions of the Royal Society of London*, 90, pp. 284
- Hewish, A., Bell, S. J., Pilkington, J. D. H., Scott, P. F., & Collins, R. A. 1968, *Nature*, 217, 709
- Hewitt, J., Grondin, M.-H., Lemoine-Goumard, M., et al. 2012
- Houck, J. C., & Allen, G. E. 2006, *ApJS*, 167, 26
- Hulsizer, R. I., & Rossi, B. 1948, *Phys. Rev.*, 73, 1402
- Hutchinson, G. 1952, *Philosophical Magazine Series 7*, 43, 847
- James, F., & Roos, M. 1975, *Computer Physics Communications*, 10, 343
- Jansky, K. 1933, *Proceedings of the Institute of Radio Engineers*, 21, 1387
- Kaspi, V. M., & Helfand, D. J. 2002, in *Astronomical Society of the Pacific Conference Series*, Vol. 271, *Neutron Stars in Supernova Remnants*, ed. P. O. Slane & B. M. Gaensler, 3
- Katagiri, H., Tibaldo, L., Ballet, J., et al. 2011, *ApJ*, 741, 44

- Katsuta, J., Uchiyama, Y., Tanaka, T., et al. 2012
- Kennel, C. F., & Coroniti, F. V. 1984, *ApJ*, 283, 710
- Kerr, M. 2010, PhD thesis, University of Washington
- King, I. 1962, *AJ*, 67, 471
- Klein, O., & Nishina, T. 1929, *Zeitschrift fur Physik*, 52, 853
- Kniffen, D. A., & Fichtel, C. E. 1970, *ApJ*, 161, L157
- Krause, J., Carmona, E., Reichardt, I., & for the MAGIC Collaboration. 2011, *ArXiv e-prints*
- Kraushaar, W., Clark, G. W., Garmire, G., et al. 1965, *ApJ*, 141, 845
- Kraushaar, W. L., Clark, G. W., Garmire, G. P., et al. 1972, *ApJ*, 177, 341
- Large, M. I., Vaughan, A. E., & Mills, B. Y. 1968, *Nature*, 220, 340
- Li, T.-P., & Ma, Y.-Q. 1983, *ApJ*, 272, 317
- Longair, M. S. 2011, *High Energy Astrophysics*, 3rd edn. (The Edinburgh Building, Cambridge CB2 8RU, UK: Cambridge University Press)
- Mattox, J. R., Bertsch, D. L., Fichtel, C. E., et al. 1992, *ApJ*, 401, L23
- Mattox, J. R., Bertsch, D. L., Chiang, J., et al. 1996, *ApJ*, 461, 396
- Mayer-Hasselwander, H. A., Kanbach, G., Bennett, K., et al. 1982, *A&A*, 105, 164
- McK Mahille, J., Schild, R., Wendorf, F., & Brenner, R. 2007, *African Skies*, 11, 2
- Morrison, P. 1958, *Il Nuovo Cimento*, 7, 858
- Neronov, A., Semikoz, D. V., Tinyakov, P. G., & Tkachev, I. I. 2011, *A&A*, 526, A90
- Nolan, P. L., Arzoumanian, Z., Bertsch, D. L., et al. 1993, *ApJ*, 409, 697

- Nolan, P. L., Fierro, J. M., Lin, Y. C., et al. 1996, *A&AS*, 120, C61
- Nolan, P. L., Abdo, A. A., Ackermann, M., et al. 2012, *ApJS*, 199, 31
- Pacini, F. 1967, *Nature*, 216, 567
- . 1968, *Nature*, 219, 145
- Pacini, F., & Salvati, M. 1973, *ApJ*, 186, 249
- Petre, R., Becker, C. M., & Winkler, P. F. 1996, *The Astrophysical Journal Letters*, 465, L43
- Protasov, R., van Dyk, D. A., Connors, A., Kashyap, V. L., & Siemiginowska, A. 2002, *ApJ*, 571, 545
- Rea, N., & Esposito, P. 2011, in *High-Energy Emission from Pulsars and their Systems*, ed. D. F. Torres & N. Rea, 247
- Rees, M. J., & Gunn, J. E. 1974, *MNRAS*, 167, 1
- Richards, D. W., & Comella, J. M. 1969, *Nature*, 222, 551
- Rousseau, R., Grondin, M.-H., Van Etten, A., et al. 2012, *A&A*, 544, A3
- Rybicki, G. B., & Lightman, A. P. 1979, *Radiative processes in astrophysics* (New York: John Wiley & Sons Ltd)
- Schwarz, G. 1978, *The Annals of Statistics*, 6, pp. 461
- Slane, P., Castro, D., Funk, S., et al. 2010, *The Astrophysical Journal*, 720, 266
- Sreekumar, P., Bertsch, D. L., Hartman, R. C., Nolan, P. L., & Thompson, D. J. 1999, *Astroparticle Physics*, 11, 221
- Sreekumar, P., Bertsch, D. L., Dingus, B. L., et al. 1992, *ApJ*, 400, L67
- Sreekumar, P., Bertsch, D. L., Dingus, B. L., et al. 1998, *The Astrophysical Journal*, 494, 523

- Staelin, D. H., & Reifenshtein, III, E. C. 1968, *Science*, 162, 1481
- Swanenburg, B. N., Hermsen, W., Bennett, K., et al. 1978, *Nature*, 275, 298
- Swanenburg, B. N., Bennett, K., Bignami, G. F., et al. 1981, *ApJ*, 243, L69
- Tanaka, T., Allafort, A., Ballet, J., et al. 2011, *ApJ*, 740, L51
- Taylor, A. R., Gibson, S. J., Peracaula, M., et al. 2003, *AJ*, 125, 3145
- Thompson, D. J. 2008, *Reports on Progress in Physics*, 71, 116901
- Thompson, D. J., Fichtel, C. E., Hartman, R. C., Kniffen, D. A., & Lamb, R. C. 1977a, *ApJ*, 213, 252
- Thompson, D. J., Fichtel, C. E., Kniffen, D. A., & Ogelman, H. B. 1977b, *ApJ*, 214, L17
- Thompson, D. J., Bertsch, D. L., Fichtel, C. E., et al. 1993, *ApJS*, 86, 629
- van der Swaluw, E., & Wu, Y. 2001, *ApJ*, 555, L49
- Weekes, T. C., Cawley, M. F., Fegan, D. J., et al. 1989, *ApJ*, 342, 379
- Young, E. T., Lada, C. J., & Wilking, B. A. 1986, *ApJ*, 304, L45